

PROPER ORTHOGONAL DECOMPOSITION AND TOMOGRAPHIC ANALYSIS
OF COMBUSTION SYSTEMS FOR CONTROL APPLICATIONS

A Dissertation

Presented to the Faculty of the Graduate School
of Cornell University

In Partial Fulfillment of the Requirements for the Degree of
Doctor of Philosophy

by

Jennifer Leslie Edwards

May 2007

© 2007 Jennifer Leslie Edwards

PROPER ORTHOGONAL DECOMPOSITION AND TOMOGRAPHIC ANALYSIS
OF COMBUSTION SYSTEMS FOR CONTROL APPLICATIONS

Jennifer Leslie Edwards, Ph.D.

Cornell University 2007

Control of combustion systems is of considerable importance to the improvement of system performance and is currently an active field of research. An understanding of combustion system dynamics is crucial to the development of effective control systems. Combustion dynamics and control combine the different aspects of combustion research such as theoretical analysis of the governing equations and phenomena, computational simulation, modeling, and measurement using advanced sensors.

Investigation of the use of proper orthogonal decomposition to analyze combustion product fields and their associated dynamics is presented. Proper orthogonal decomposition is applied to CO₂ number density and vorticity magnitude data from reacting rectangular jet simulations. The resulting eigenfunctions are used to develop physical insight of the vortex formations and dynamics of these jets and their related mixing and spreading characteristics. It is seen that different vortex structures are captured in the eigenfunctions and that CO₂ and vorticity eigenfunctions are very similar indicating that vortex-driven mixing dominates in these jets. Using subsets of eigenfunctions with high information content, CO₂ and vorticity magnitude distributions can be represented with relatively few eigenfunctions.

Results of research to develop and apply multiple line-of-sight absorption and emission tomography for the study of combustion and as a sensor for monitoring and control of combustion systems are reported. Absorption tomography can provide data on the state of macro-mixing in combustion systems that can influence system

performance, e.g. efficiency, radiation signature, and pollutant emissions. The development of an IR laser absorption facility for rapid scanning tomography and the performance of the tomographic reconstruction technique, Adaptive Finite Domain Direct Inversion, are discussed. The development of a sensor system for use in a practical combustion device is also addressed. Computational simulation of a combustor sector rig provided operating state conditions such as excited state population and temperature distributions. Emission tomography measurements were simulated using numerical line-of-sight integration of simulated excited state number densities of water for two emission transitions. Tomographic reconstruction was performed using Tomographic Reconstruction via a Karhunen-Loeve Basis to evaluate nine line-of sight measurement configurations and an optimal measurement configuration was selected. Operating state identification for control applications was investigated using the TRKB reconstructions.

BIOGRAPHICAL SKETCH

Jennifer L. Edwards was born in Newport News, VA in 1977. After moving briefly to various army bases, her family returned to her home state and settled in Fairfax County where they lived for over 20 years. Jennifer graduated from Chantilly High School. While many friends and acquaintances at CHS believed she might go to art school, her aptitude for math and science impelled her to attend the University of Virginia for her undergraduate education in engineering. Following in her father's footsteps, she received her Bachelor of Science with Highest Honors in Aerospace Engineering in 1999, focusing in aerodynamics. Through her undergraduate work in laser induced fluorescence for flow visualization, she developed an interest in laser diagnostic techniques. She began her graduate studies in the Sibley School of Mechanical and Aerospace Engineering at Cornell University in the fall of 1999. Her interest in laser diagnostics and optics was furthered through her work on tomography systems and applications at Cornell. She is currently working on electro-optics at the Johns Hopkins University Applied Physics Laboratory in Laurel, MD. When she finds the time, she still enjoys photography and other artistic endeavors.

To my family and Bryon

ACKNOWLEDGEMENTS

I would like to acknowledge the love and support of my parents throughout all of my endeavors. You've always made me feel like there was nothing I couldn't do. I thank my sister Katie for always being there when I needed to vent, and for sharing our odd sense of humor that only we truly understand. And I must thank Kellycat for being a welcome distraction during graduate school and in the years beyond.

Special thanks go to my committee chair, Professor Frederick C. Gouldin, for his guidance and support. I would like to thank Professor Elizabeth Fisher and Professor Clifford Pollock for serving on my committee and for their helpful advice. I would also like to acknowledge Professor George Wolga for his guidance and assistance in the development of the laser absorption facility. Additional thanks go to Dr. Mark MacDonald, Dr. Ann Chojnacki, and Dr. Michael Feng for their extensive work on the Cornell tomography experiments.

Graduate school would not have been the same without my dear friends. First and foremost, I acknowledge Sandra Sattler: my housemate, coworker, and general "partner in crime" throughout graduate school. Thanks to Louise and Greg Chini, Mark MacDonald, Tina Jayaweera, and Jonathan Pearlman for injecting my life with humor and optimism. Thanks to Juan Abelló for the many tangos together and a few late night phone calls. Thank you to Mike Moorhead, Veronica and Ryan Santos, and Terry Mcloughlin for your friendship and support near the end of my studies.

I would like to thank Nishant and Katie Mehta and Laurie O'Connor for their friendship in this next phase of my life. Finally, I would like to thank C. Bryon Hargis for being a source of never-ending love and support, and for pushing me to get this done! Thanks for being there for me.

The Office of Naval Research with Dr. Gabriel Roy as scientific officer is gratefully acknowledged for supporting the work presented in Chapter 2 and Chapter 3 of this dissertation under ONR grant # N00014-99-1-0447.

The work reported in Chapter 4 was supported by Pratt and Whitney. I would like to thank Dr. Jeffrey Cohen and Dr. Arash Ateshkadi for their valuable input and feedback.

TABLE OF CONTENTS

1	Introduction	1
2	Reduced Order Structure of Reacting Rectangular Jets	5
2.1	Introduction	6
2.2	Reacting Rectangular Jets.....	11
2.3	Proper Orthogonal Decomposition.....	14
2.4	Results	18
2.4.1	CO ₂ Concentration.....	18
2.4.2	Vorticity Magnitude	21
2.4.3	Axis Switching	25
2.4.4	Eigenvalue Spectra and the Potential for Reduced Modeling	27
2.5	Summary and Conclusions	32
	Appendix A Grid Resolution Issues.....	37
	Appendix B Proper Orthogonal Decomposition Matrix Formulation.....	43
	Acknowledgements	44
	References	45
3	High Speed Absorption Tomography with Advanced Reconstruction Algorithms.	51
3.1	Introduction	52
3.2	Absorption Tomography	53
3.3	IR Absorption Facility.....	55
3.4	Flow Apparatus	59
3.5	Performance of Absorption Apparatus.....	60
3.6	Tomographic Reconstruction	61
3.7	Forced Square Jet Reconstructions from Laboratory Data.....	68
3.8	Performance of Adaptive FDDI	73
3.9	Summary and Conclusions	86
	Acknowledgements	89
	References	90
4	Emission Tomography for Gas Turbine Combustor Control	92
4.1	Introduction	93
4.2	Tomographic Reconstruction via a Karhunen-Loeve Basis.....	99
4.2.1	Tomographic Reconstruction Problem.....	99
4.2.2	TRKB Basis Set Development	103
4.2.3	Error Measures	104
4.2.4	Evaluation of Tomography for Control using TRKB.....	106
4.3	Combustor Simulations and Modeling of Emission Measurements	108
4.3.1	Combustor simulation	108
4.3.2	Modeling of Emission Measurements	110
4.3.3	Practical Emission Estimates.....	117

4.4	Results	125
4.4.1	Evaluation of Tomographic Measurement Configurations	131
4.4.2	Control Applications	140
4.5	Summary and Conclusions	144
	Appendix POD Analysis and Results.....	148
	Acknowledgements	150
	References	151
5	Summary.....	155

LIST OF FIGURES

2.1	Schematic diagram of computational domain representing the output grid provided for this study.....	14
2.2	First eigenfunctions of CO ₂ at y=0.4De (top), 2.6De (middle), 5.7De (bottom) for a) AR=1; b) AR=2; and c) AR=3 jets.....	19
2.3	Eigenvalue spectra for CO ₂ and vorticity eigenfunctions at y=0.4De (top), y=2.6De (middle), and y=5.7De (bottom).....	20
2.4	First eigenfunctions of vorticity at y=0.4De (top), 2.6De (middle), and 5.7De (bottom) for a) AR=1; b) AR=2; and c) AR=3 jets.....	22
2.5	Second eigenfunctions of vorticity at y=0.4De (top), 2.6De (middle), and 5.7De (bottom) for a) AR=1; b) AR=2; and c) AR=3 jets.....	23
2.6	Vorticity eigenfunctions displaying axis-switching in the three jets. a) Switching first occurs at y=2.6De for AR=1; b) Switching first	26
2.7	Representation results using 6 eigenfunctions of a representative CO ₂ distribution in the square jet at y=2.6De	33
2.8	Representation results using 10 eigenfunctions of a representative vorticity magnitude distribution in the square jet at y=2.6De.....	33
2.9	Vorticity distributions on streamwise planes passing through the jet axis for run rc40 (top) and run rc36 (bottom).....	39
2.10	Normalized eigenvalue spectra at y ₁ =2.2De (top) and y ₂ =3.3De (bottom).....	40
2.11	a) First eigenfunctions of vorticity for rc36 jet (left) and rc40 jet (right) at y ₁ =2.2De (top) and y ₂ =3.3De (bottom).....	41
3.1	Schematic of coordinate system and LOSs in a single view. LOSs are defined by the offset s , and viewing angle, θ	54
3.2	Schematic diagram of the IR absorption facility. The absorption facility consists of an IR laser beam divided amongst 6 scanning modules	56
3.3	Schematic diagram of a single module and reference detector. Each module consists of a focusing lens, a mirror	57
3.4	Schematic diagram of square jet flow apparatus. A CO ₂ /air mixture is fed through a speaker chamber that forces the flow	59
3.5	Absorption measurements from a 6 m/s forced jet with 50% CO ₂ made at the jet exit. (a) Raw laser scanning data recorded from the reference	62
3.6	Two-dimensional basis functions of varying aspect ratios used in the FDDI and AFDDI reconstructions. Basis functions are both spatially	65
3.7	Adaptive grid for a square phantom distribution. Left: uniform grid of 97 basis functions used in FDDI. Characteristic view angles	67
3.8	Filtered forced jet AFDDI reconstructions of a 6 m/s jet with 50% CO ₂	70
3.9	Reconstructions at 0, 90, 180 and 270 degrees in the forcing phase. Maximum CO ₂ values are labeled on the plots in arbitrary units	71
3.10	Sample phantom top-hat distribution used in evaluation of AFDDI performance (see Figure 3.7 for corresponding AFDDI grid).....	74

3.11	Sample multiple-jet (left) and merged-peak phantom distributions derived from previous measured data [1,17].....	75
3.12	Reconstruction and representation errors for various jet and peak distributions	78
3.13	Reconstruction and representation errors for gaussian peak distributions	80
3.14	Triangular top hat distribution rotated at 0 degrees and reconstruction errors of the triangular distribution under rotation.....	84
4.1	Tomographic measurement geometry	99
4.2	CFD single nozzle schematic	110
4.3	Sample temperature, pressure, and fuel-air ratio distributions provided by CFD simulations.....	111
4.4	H ₂ O spectral information provided by HITRAN	118
4.5	Line-of-sight collection geometry	120
4.6	Sample n_A excited state population distributions from the ensemble. The outer zone, middle zone, and inner zone, locations are marked	127
4.7	First three n_A population eigenfunctions.	128
4.8	Eigenvalue spectra for the n_A and n_B population eigenfunctions.....	129
4.9	LOS measurement configurations considered. Inner, middle, and outer regions correspond to minimum, median, and maximum Z locations	130
4.10	Mean error measures presented for the nine measurement configurations	134
4.11	Average reconstruction errors for four sample n_A distribution reconstructions in the presence of noise in the projection measurements	136
4.12	Sample population distributions and errors in reconstruction. Note, the distributions for n_A and n_B presented	139
4.13	Temperature distributions and errors in reconstructions corresponding to the two operating states presented in Figure 4.12	141
4.14	Error measures corresponding to temperature distributions calculated from reconstructed populations (\circ) and filtered.....	142

LIST OF TABLES

2.1. Percentage of information content of each CO ₂ and vorticity magnitude eigenfunction presented.....	24
2.2. Comparison of information content of subsets of CO ₂ eigenfunctions (average values for the three aspect ratio jets).....	30
2.3. Comparison of information content of subsets of vorticity eigenfunctions (average values for the three aspect ratio jets.).....	30
2.4. Errors in representations of chosen CO ₂ and vorticity magnitude distributions using subsets of eigenfunctions are presented. Bold values indicate the representations presented in Figures 2.7 and 2.8.....	32
3.1. Comparison of forcing effects on two forced CO ₂ /air jets.....	72
3.2. Sample reconstruction error results for a phantom distribution with noisy projection measurements.....	82
3.3. Sample reconstruction error results for a case with high AFDDI reconstruction error.....	82
3.4. Effect of the addition of basis functions on AFDDI representation and reconstructions errors.....	83
4.1. Projection matrix condition numbers for a 12 eigenfunction basis set.....	137
4.2. Number of states identified using basis sets consisting of 12 eigenfunctions.....	143
4.3. Sample State Identification Results.....	144

Chapter 1

Introduction

The widespread use of combustion systems in applications related to propulsion, power generation, heating, and waste incineration make combustion control an area of continuing interest. Control of combustion systems is of considerable importance to the improvement of system performance and is currently an active field of research. As a complex system, an understanding of combustion system dynamics is crucial to the development of effective control systems. Combustion dynamics and control combine the different aspects of combustion research such as theoretical analysis of the governing equations and phenomena, computational simulation, modeling, and measurement using advanced sensors. Control of combustion instabilities has been a primary concern in combustion systems. Combustion processes are extremely susceptible to instabilities; high energy density (heat release) drives oscillations, resonant properties of combustor geometries allow for acoustic oscillations, and perturbations in the flow feed unstable processes, which grow according to the Rayleigh criterion when the heat-release is in phase with pressure fluctuations. Efficiency and optimization of a combustion process are also of primary concern. Combustor efficiency, temperature distribution (pattern factor), radiant signature, exhaust gas composition, and pollutants can be optimized through control of the operating state of a combustion system.

Combustion control techniques can be divided into *passive* and *active* control methods. Passive control methods aim to reduce the dominant unstable oscillations in a combustion system through modifications of combustor geometry or introduction of resonators to alter resonant conditions and damp oscillations. Passive control methods are often inadequate for control in situations where combustor operating conditions change. Active closed-loop or feedback control is promising for control of combustion systems as it enables control of combustion systems under constantly changing conditions. Required for the development of an active control system are sensors for monitoring the combustion process and actuators used for modulation of the process. Methods of active control include the use of actuators such as acoustic drivers to induce pressure oscillations, fuel injectors used to alter fuel flow configurations and timing, secondary jets used to alter velocity or vorticity fields, and heating elements. A thorough understanding of the combustion dynamics is necessary for the development of models relating the important parameters and governing equations for use in control algorithms. The goal of the present work is the investigation of several of these important aspects of active combustion control, including the potential for model development and advancement in sensing technology.

Active feedback control requires modeling of a combustion system and testing of control concepts under representative conditions. The complex dynamics of a combustion system are governed by a set of partial differential equations, making thorough analytical investigation of combustion behavior difficult. However, an understanding of combustion dynamics and the underlying elementary processes is necessary for successful control. Finite-dimensional or *reduced order* models become necessary for the study of combustion parameters and their response to control action. Flame/vortex interactions, vortex enhanced mixing, and acoustic flame coupling are

examples of processes important to combustion dynamics. Understanding of these individual processes may be used to develop components of a more comprehensive model of the combustion system dynamics. In **Chapter 2**, the potential for development of reduced order models based on the CO₂ and vorticity fields is evaluated for forced reacting rectangular jets. These jets are of interest for use as actuators in combustion control applications as they have been shown to enhance mixing and entrainment through the development of large-scale vortical structures.

The use of fast, accurate, and robust sensors is required to make active combustion control possible. Information from sensors monitoring the combustion zone or exhaust gases is used in a feedback loop to reduce combustion instability or optimize combustor performance through operating point control. Practical considerations for the use of sensors, including optical sensors, in combustion systems include speed of data acquisition for real-time control applications, measurement accuracy, integration of sensors in practical combustor geometries, and limitations on optical access. Common sensors used in combustion applications include pressure transducers, photodiodes, and radiometers. The evaluation of a new tomographic measurement facility coupled with tomographic reconstruction using the Adaptive Finite Domain Direct Inversion (AFDDI) algorithm is presented in **Chapter 3**. This chapter addresses the issues of data acquisition speed and measurement accuracy. The high-speed infrared absorption facility was developed to make a complete set of measurements in less than 2 ms for tomographic reconstruction of combustion product concentrations. The practical implementation of tomographic measurement as a sensor for combustion control is considered in **Chapter 4**. Emission measurements are simulated at the exit plane of a practical combustor demonstrating that a limited number of measurements is required for accurate reconstruction using the

Tomographic Reconstruction via a Karhunen-Loeve Basis (TRKB) algorithm. The issues of sensor integration and limited optical access are addressed in this chapter.

Chapter 2

Reduced Order Structure of Reacting

Rectangular Jets

Jennifer L. Edwards¹, Frederick C. Gouldin²,

Cornell University, Ithaca, NY 14853

Fernando F. Grinstein³, and Kazhikathra Kailasanath³

US Naval Research Laboratory, Washington, DC 20375

ABSTRACT

The results of proper orthogonal decomposition analyses on CO₂ number density and vorticity magnitude data from reacting rectangular jet simulations are presented. The resulting proper orthogonal decomposition eigenfunctions are used to develop physical insight of the vortex formations and dynamics of these jets and their related mixing and spreading characteristics. It is seen that different vortex structures are captured in

¹ Graduate Student, Sibley School of Mechanical and Aerospace Engineering.

² Professor, Sibley School of Mechanical and Aerospace Engineering.

³ US Naval Research Laboratory, Washington, DC.

the eigenfunctions and that CO₂ and vorticity eigenfunctions are very similar indicating that vortex-driven mixing dominates in these jets. The eigenvalue spectra associated with these eigenfunctions are used to evaluate the information content of the eigenfunctions, and the potential for reduced order models. Using subsets of eigenfunctions with high information content, CO₂ and vorticity magnitude distributions can be represented with relatively few eigenfunctions. However, as the flows develop downstream, more eigenfunctions are needed to represent them to the same level of accuracy. The potential for reduced order modeling of each field is approximately the same for the jets of aspect ratios 1, 2, and 3, however, there is stronger potential for reduced order modeling of the CO₂ field than of the vorticity field.

2.1 Introduction

Combustion control technologies are under development for application to advanced combustion and propulsion systems [1-13]. Detection and control of the large-scale flow and scalar features in these systems are of primary importance as internal mixing control can improve combustor performance [1,2,6,10,14]. An overview of combustion dynamics and control can be found in the review article by Candel [8]. The behavior of a combustion system is governed by a set of partial differential equations (PDEs) that describe the fluid dynamics, combustion dynamics, heat transfer, and acoustics of the system [15]. These PDEs and their associated boundary conditions define a system state located in an infinite-dimensional state space [16,17,18] that can change as a function of both time and condition. Detailed solution of the PDEs is impractical for control applications and finite-dimensional or *reduced order* models become necessary to describe the behavior of the system. Reduced order models representing the dynamics of a combustion system are crucial

to the development of effective combustion control, by providing a model of the system and how it responds to control actuation [3,4,8,9,11]. For control applications, these models have been developed in two ways: 1) through projection of the governing equations onto a subspace defined by a chosen basis set [18-21]; and 2) through a system identification approach where a mathematical model describing the relationships among the important system variables is obtained from empirical input and output data, often including expansions of individual input or output parameters in a basis set [11,22]. It has been shown that the performance of a control system depends highly on the quality of the basis set used¹⁹ and proper orthogonal decomposition eigenfunctions are often utilized [9,11,19,21,23-25] because of their ability to represent important parameters efficiently, requiring only a small number of eigenfunctions in an expansion.

The Karhunen-Loeve (KL) procedure, or Proper Orthogonal Decomposition (POD), is one method that could be used to develop reduced order models and investigate large-scale structures of a combustion system. POD decomposes a set of distributions or functions, the ensemble, into an optimal orthonormal set of eigenfunctions able to represent the distributions of the ensemble [18,26-28]. These distributions are represented as a weighted expansion of the eigenfunctions. Subsets of these eigenfunctions can offer highly efficient representations of important variables in combustion systems. They are optimal in the sense that they contain the most information relative to any other basis set and allow one to capture the dominant features of a system using the fewest number of basis functions in an expansion. Examination of a few POD eigenfunctions quickly identifies the most important large-scale structures of the flow enabling the researcher to visualize the flow behavior and determine where more detailed investigation is desired. Furthermore, the potential for a reduced order model utilizing these basis functions can be evaluated from their

information content as determined from the associated eigenvalue spectrum derived from POD. The eigenvalue spectrum quantifies the average contribution of each eigenfunction in representing the distributions in the ensemble, and thus its relative importance, to the representation of the system properties. For a reduced order model utilizing an expansion in a set of basis functions, a measure of the potential for modeling is the number of basis functions necessary to capture the flow physics. Because the POD eigenfunctions provide an optimal basis set, the number of POD derived basis functions required will be the lowest of any basis set and POD analysis can be used as a best case to evaluate the potential for modeling.

Proposed by Lumley in 1967 as a method to recover coherent structures in turbulent flows [29], POD has become widely used for investigation of organized structures in jet flows. POD has been used to study velocity data generated by numerical simulation [30,31] as well as particle image velocimetry (PIV) [32,33] and hot-wire measurements [34-36] in various jet configurations. POD has also been applied to scalar fields such as concentration and temperature produced by numerical simulation [30,31,37] and experimental measurement [32,38,39]. POD has been used by a number of researchers to study various spatial structures in physical flows and systems [18,26,27]; for example, it has been applied to the study of turbulent mixing in jets [40] and facial pattern recognition [27]. POD results are frequently used to study the dynamics and understand the nature of jet flows. For instance, results have been used to examine the stagnation point location and radial velocity fluctuations in an annular jet [33]. The relation between jet stability and jet flapping and penetration were examined for a round jet in a counterflow [32], and vortex rings and jet flapping were investigated in round jet-like flows [39]. POD results are also commonly applied to the identification and evolution of large-scale structures in jet flows and used in low-dimensional representations of the fields studied [31,34-38]. Tornianen *et al.*

developed a tomographic reconstruction technique using POD eigenfunctions as basis functions, taking advantage of the optimality of the eigenfunction set and the ability to represent a scalar field using relatively few basis functions [37].

Low-dimensional models based on Galerkin projection of the governing equations onto POD eigenfunctions have been developed [9,11,30,41,42]. Studies have utilized POD eigenfunctions to develop reduced order models of flow over compliant wall surfaces and coherent structures in turbulent boundary layers [41] as well as turbulent plane Couette flow [42]. Models based on POD eigenfunctions have been developed to describe burning characteristics and instability in combustion systems for use in control applications [9,11]. POD eigenfunctions have also been used with partial measurements of data fields in a H₂/air opposed-jet diffusion flame to estimate “unmeasured” quantities, showing that POD eigenfunctions have good interpolative properties [31]. The forced 1-D turbulent jet studies of Faghani *et al.* showed that eigenfunctions depend on the domain of measurements but are possibly invariant in a given flow for certain relevant parameters, e.g. Reynolds number [35]. It has been suggested that the use of POD eigenfunctions may be extended to situations similar to that from which they were derived if the ensemble of distributions from which the eigenfunctions were generated is sufficiently large and contains sufficient information on the dynamics of the system [20,35]. However, for the majority of applications, models utilizing POD eigenfunctions are developed for a specific system. Due to the need for an ensemble of distributions, the eigenfunctions must be derived from computational [9,19,21,23,24] or experimental data [11,23,25] representative of the system of interest and are sometimes referred to as *empirical eigenfunctions*. The necessary ensemble may contain distributions resulting from various operating states of a system or a set of measured or simulated time realizations of important variables in an unsteady process.

The majority of the studies mentioned above were applied to axisymmetric or plane jets. The studies were performed on non-forced and forced [35-37] flows and, with the exception of Refs. 31 and 37, the jet studies were performed on non-reacting flows. Forced jets are of particular interest due to their use as actuators in combustion control applications [3-7]. Rectangular jets have been shown to passively improve mixing of the jet (e.g. fuel) with its surroundings (oxidizer) through enhanced entrainment due to axis-switching and to enhance mixing near corner regions and far downstream [1,43-45]. Entrainment and mixing control are highly dependent upon the development of large-scale coherent vortical structures in the flow and their breakdown into turbulence.

We are investigating CO₂ and vorticity magnitude data in forced rectangular reacting jets of varying aspect ratios as non-premixed flames where fuel-oxidizer mixing is required for chemical reaction [43,44]. Near the jet exit, CO₂ production is governed primarily by fuel-air mixing through the vortex formations there while farther downstream, its presence is governed not only by production in mixed zones, but also by convective and diffusive transport. CO₂ concentration data are useful as an indicator of overall mixing, as well as being an important measure of combustion progress. Vorticity magnitude data is investigated because of the importance that vorticity plays in the mixing and entrainment of these jets and the connection between combustion instabilities and vortex dynamics [10,14,46].

Data for the jet flows studied are obtained from large-eddy simulation (LES) of the jets, reported separately [43,44]. While both experimental and numerical simulation data can be used for the POD analysis, the need for a large number of distributions in the ensemble makes simulation data the most attractive choice. LES reduces the need for the extensive computational resources required by direct

numerical simulation (DNS) and eliminates the need for experimental resources needed to gather large amounts of data on multiple jets for this study.

In this paper the results of POD applied to CO₂ concentration and vorticity magnitude fields in forced rectangular reacting jets of aspect ratios $AR=1-3$ are reported and discussed. By consideration of eigenvalue spectra and eigenfunction information content we evaluate the potential for reduced order modeling of vorticity and scalar fields in forced rectangular jets using a limited number of basis functions. In addition, we investigate the structures of these jets through the study of the vorticity magnitude and CO₂ concentration fields. Through comparison of these two fields, we can investigate the effect of vorticity on jet mixing and combustion and extract physical insight about the jet structures.

2.2 Reacting Rectangular Jets

Large Eddy Simulation (LES) of turbulent reacting rectangular jets was performed on forced jets of varying aspect ratios ($AR=1-3$) [43,44]. Monotonically Integrated LES (MILES) [43-45,47-52] was used for the LES computations in this paper. The MILES approach involves solving the unfiltered Euler or Navier-Stokes equations with high-resolution, locally monotonic algorithms such as the Flux-Corrected Transport (FCT) method or the Piecewise Parabolic Method (PPM). Non-linear high-frequency filters built into the algorithms provide implicit SGS models eliminating the use of explicit SGS models introduced for closure in conventional LES. Formal properties of the effectual SGS modeling using MILES are presented in Refs. 44 and 48.

By design, the simulated rectangular jets differed in AR but had otherwise essentially identical initial conditions, including nearly identical De . Propane-nitrogen jets were issued into a quiescent oxygen-nitrogen background, with reactant molar

concentrations chosen to be the same and equal to 0.4, a Mach number of 0.3, and Reynolds number greater than 85,000 – based on the jet exit velocity, U_o , and the circular-equivalent jet diameter, De , (the diameter of a round jet having the same cross-sectional area). Typical Re for the jets discussed in this paper is $Re=U_oDe/\nu>85000$ based on estimated upper bounds for the effective numerical viscosity of the FCT algorithm [44,49]. The jets were initialized with laminar conditions, thin rectangular vortex sheets, slightly rounded-off corner regions, and uniform initial momentum thickness, θ , such that $De/\theta=50$. The jet exit velocity was forced axially by superimposing a single-frequency sinusoidal perturbation on the jet-exit velocity, $U_o=200\text{m/s}$, having an rms level of 2.5% and Strouhal frequency $St=fDe/U_o=0.48$.

A global (single-step irreversible) model for propane chemistry was used [44,53], $\text{C}_3\text{H}_8+5\text{O}_2\rightarrow 3\text{CO}_2+4\text{H}_2\text{O}$, with the fuel consumption rate given by $\omega=A_r\exp(-E_{act}/RT)[\text{C}_3\text{H}_8]^\alpha[\text{O}_2]^\beta$, $\alpha=0.1$, $\beta=1.65$, $A_r=8.6\times 10^{11}\text{ cm}^{2.25}\text{ mol}^{-0.75}\text{ s}$, and $E_{act}=30\text{ kcal mol}^{-1}$. As the fuel consumption rate is sensitive to fuel and oxidizer concentrations as well as temperature, it can handle extinction and reignition in a limited manner when there are large fluctuations in concentrations or temperature. Given the simplified chemistry model used and the assumption of near unity Lewis numbers (typical Le range from 0.8 to 0.94), coupling relations between species and temperature can be developed [54,55]. With these assumptions, it is expected that temperature or species data for the POD analysis will provide the same information with regard to the potential for modeling of these fields. Convective mixing (stirring) and fast chemistry dominate in the flow regime of these jets (fast flow, high Damkohler number), such that this combustion model is useful to provide a reasonable, simple framework to assess the utility of POD. This chemistry model is reasonable for calculating heat release rate for use in combustion instability and control studies [47,50]. The

background gases were at 1400 K to ensure autoignition of the jet. Multi-species temperature-dependent diffusion and thermal conduction processes were calculated explicitly using central difference approximations and coupled to the chemical kinetics and convection using timestep-splitting techniques. The numerical model was second order in space and time [47]. Subgrid fluctuations were neglected and instantaneous evaluation of relevant combustion quantities such as diffusivities, thermal conductivities, and fuel burning rates was performed directly in terms of unfiltered variables. Further details on the simulated transport properties and their validation are discussed in Refs. 43, 44, 47 and references therein.

The close relationship between unsteady fluid dynamics and non-premixed combustion in high-speed propane jets emerging into an air background was used to illustrate the potential practical impact of the vortex dynamics on the jet entrainment. For the jet regimes considered, large-scale vortex-driven convective mixing dominated, and instantaneous entrainment and fuel-burning rates were highly correlated [47]. These are precisely the kinds of regimes (large-scale driven entrainment, mixing, and combustion) where LES can be expected to be useful. Moreover, because the regimes involve near-unity jet-to-background density ratio and virtually negligible preferential diffusion effects such that differences in Lewis and Schmidt numbers between the jet and surroundings are small, the results for propane reactive jets discussed are not very dependent on the combustion specifics [44,47]. The main focus of the simulations is to relate unsteady jet combustion and fluid dynamics while examining the basic topological features of the jets.

Jet simulations were performed on a $140 \times 200 \times 140$ computational grid and the results were presented on a $120 \times 200 \times 120$ inner subdomain, at up to 63 equally spaced times with time interval = $0.1/f$. The cell spacing, dx , of the output grid was equal to 0.015 cm, and the reference equivalent jet diameter was $De=0.338$ cm; see Figure 2.1.

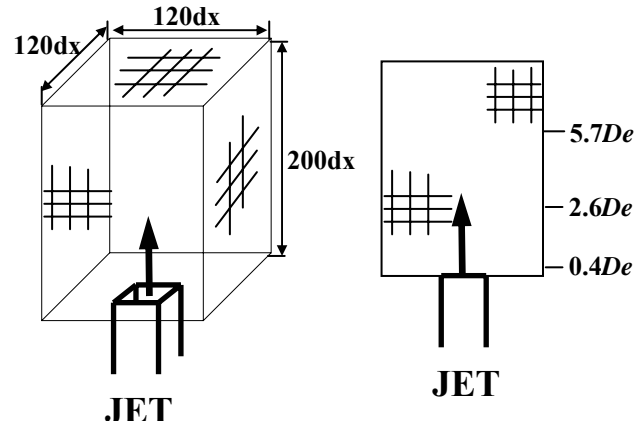


Figure 2.1. Schematic diagram of computational domain representing the output grid provided for this study [37].

Jet dimensions are 0.3cm×0.3cm, 0.21cm×0.42cm, and 0.18cm×0.54cm for the AR=1,2, and 3 jets respectively. Convergence studies indicate that the MILES approach is capable of capturing the dominant inertial subrange in these flows. Previous spectral analysis⁴⁵ of the jets presented on the coarse and fine grids in Appendix A showed similar trends for amplitudes and self-similar behaviors on the smallest resolved scale. Grid resolution issues in the context of POD are addressed in Appendix A.

2.3 Proper Orthogonal Decomposition

Proper orthogonal decomposition (POD) is a mathematical procedure that we have applied to the study of reacting forced jets. It is useful because it produces an optimal orthonormal set of eigenfunctions from an ensemble of distributions. The eigenfunctions are optimal in the sense that they are calculated to have the smallest mean squared error in representing the ensemble of distributions for any fixed number of terms in the expansion compared to any other basis set [26-28]. Due to the optimality of the POD basis set, it can be used as a best case to evaluate the potential for development of a reduced order model utilizing an expansion in any set of basis

functions, making POD analysis useful to the development of reduced order models of the system under investigation. POD is used here to investigate the potential for reduced order modeling of forced reacting rectangular jet systems through evaluation of the eigenvalue spectra and eigenfunction information content, as well as to capture and study large-scale features of these jet flows, specifically large-scale spatial structures in CO₂ concentration distributions and vorticity magnitude distributions. The most important POD eigenfunctions contain those structures that are the most significant, primarily large-scale structures. Because the large scales are well resolved with LES and we are interested in retaining the most important eigenfunctions for modeling and analysis, POD analysis is well suited for this study. Information regarding the spatiotemporal behavior of the large-scale structures can be gained from the results of POD applied to the CO₂ and vorticity fields.

An ensemble of time realizations such as those in this study can be expanded as a superposition of KL eigenfunctions, each with a set of associated time coefficients that correspond to all of the time realizations of the ensemble. Each eigenfunction also has an associated eigenvalue, which classifies the importance of the eigenfunction to the representation of the ensemble of time realizations. The eigenvalues are the mean square of the associated time coefficients. The KL eigenfunctions and time coefficients are determined from a matrix eigenvalue problem via the method of snapshots [27,28]. Using this method, eigenfunctions are given by a superposition of instantaneous distributions from the set of time realizations, producing an intrinsically defined basis set. Details of formulation of the matrix problem that follows are included in Appendix B.

Two-dimensional POD decomposes the ensemble of scalar distributions, $\{n_j\}$, calculated at a set of discrete time realizations, (t_k) , and chosen at specified axial locations in the jet, into a set of eigenfunctions, $\{\phi_j\}$, with time coefficients, $\{a_j\}$:

$$n(x_i, z_j, t_k) = \sum_{l=1}^{N_m} a_l(t_k) \phi_l(x_i, z_j) \quad (2.1)$$

$$i=1, \dots, N_x, j=1, \dots, N_z, k=1, \dots, N_t.$$

N_x and N_z are the number of grid points in the x and z directions respectively, equal to 120 in both directions, N_t is the number of time realizations analyzed (approximately 60), and N_m is the number of eigenfunctions used in the expansion [27,28,37]. Generally, the number of eigenfunctions, N_m , necessary for a sufficient representation of a distribution $n(x, z, t_k)$ is much less than the total number of eigenfunctions provided by the POD analysis, N_t .

As noted, the eigenfunctions are given by a superposition of instantaneous distributions producing an intrinsically defined basis set. The time coefficients and eigenfunctions are calculated by solving the following matrix eigenvalue problem through Cholesky factorization:

$$DA = A\Lambda \quad (2.2)$$

where $D \in \mathbf{R}^{N_t \times N_t}$, $A \in \mathbf{R}^{N_t \times N_t}$, and $\Lambda \in \mathbf{R}^{N_t \times N_t}$. A is a matrix containing the time coefficients and Λ is a diagonal matrix containing the associated eigenvalues [27,28,37]. The two-time correlation matrix, D , is defined by

$$D = (1/N_t)CGC^T \quad (2.3)$$

where C is a $N_t \times N_p$ ($N_p = N_x \times N_z$) matrix containing the ensemble of distributions and G is a $N_p \times N_p$ integration matrix. The integration matrix, G , is used to obtain the discrete estimate of the two-time correlation matrix, D [28]. The eigenfunctions are then calculated as [28,37]

$$\Phi = (1/N_t)\Lambda^{-1}A^TC \quad (2.4)$$

where the $N_t \times N_p$ matrix Φ contains N_t eigenfunctions that are normalized according to

$$\Phi G \Phi^T = I \quad (2.5)$$

The eigenvalue, λ_i , associated with the eigenfunction, ϕ_i , classifies the importance of that eigenfunction in the representation of the ensemble of distributions investigated. The eigenfunctions are arranged in order of importance, the first eigenfunction having the largest eigenvalue and the last eigenfunction having the smallest eigenvalue. The total amount of information present in a subset of eigenfunctions, termed the *information content*, can be evaluated as the sum of the subset of normalized eigenvalues. It is therefore possible to estimate the contribution of any particular eigenfunction or subset of eigenfunctions to a representation by determining the information content therein, see Equation (2.7). It is important to note however that the “importance” of an eigenfunction to the representation is an average quantity of the entire ensemble and may be described as an ensemble average importance. However, for any given distribution in the ensemble, the amount of information a particular eigenfunction can capture in the distribution can differ from the amount of information it captures in the ensemble on average.

For this study, the eigenvalues were normalized as

$$\bar{\lambda}_i = \frac{\lambda_i}{\sum_{j=1}^{N_m} \lambda_j} \quad (2.6)$$

following the analysis in Ref. 37 and were used to classify the information content of a

subset of the first M eigenfunctions, E_M (sometimes referred to as the “energy” of an eigenfunction [26,27])

$$E_M = \sum_{i=1}^M \bar{\lambda}_i . \quad (2.7)$$

2.4 Results

POD is used here to investigate the potential for reduced order modeling of forced reacting rectangular jet systems through analysis of eigenfunction information content, as well as to capture large-scale spatial structures in concentration and vorticity magnitude distributions. Information regarding the spatiotemporal behavior of the large-scale structures is investigated using the results of POD applied to these fields. Results were obtained by performing POD on sets of planar CO₂ concentration and vorticity magnitude distributions containing approximately 60 time realizations. Distributions at seven axial locations were examined: $y=0.4De$, $2.2De$, $2.6De$, $3.3De$, $4.8De$, $5.7De$, and $6.6De$. Results representative of the CO₂ and vorticity fields are presented here for $y=0.4De$, $2.6De$, and $5.7De$.

2.4.1 CO₂ Concentration

The first KL eigenfunctions of CO₂ concentration are presented in Figure 2.2 for the axial locations described above in reacting rectangular jets of aspect ratios 1, 2, and 3. The normalized eigenvalue spectra corresponding to the eigenfunctions produced by POD at these locations are shown in Figure 2.3. The first eigenfunction, having the largest eigenvalue, is considered to be the eigenfunction most closely correlated to the distributions contained in the ensemble and the single eigenfunction that best represents the jet distributions [37]. This eigenfunction contains over 95% of

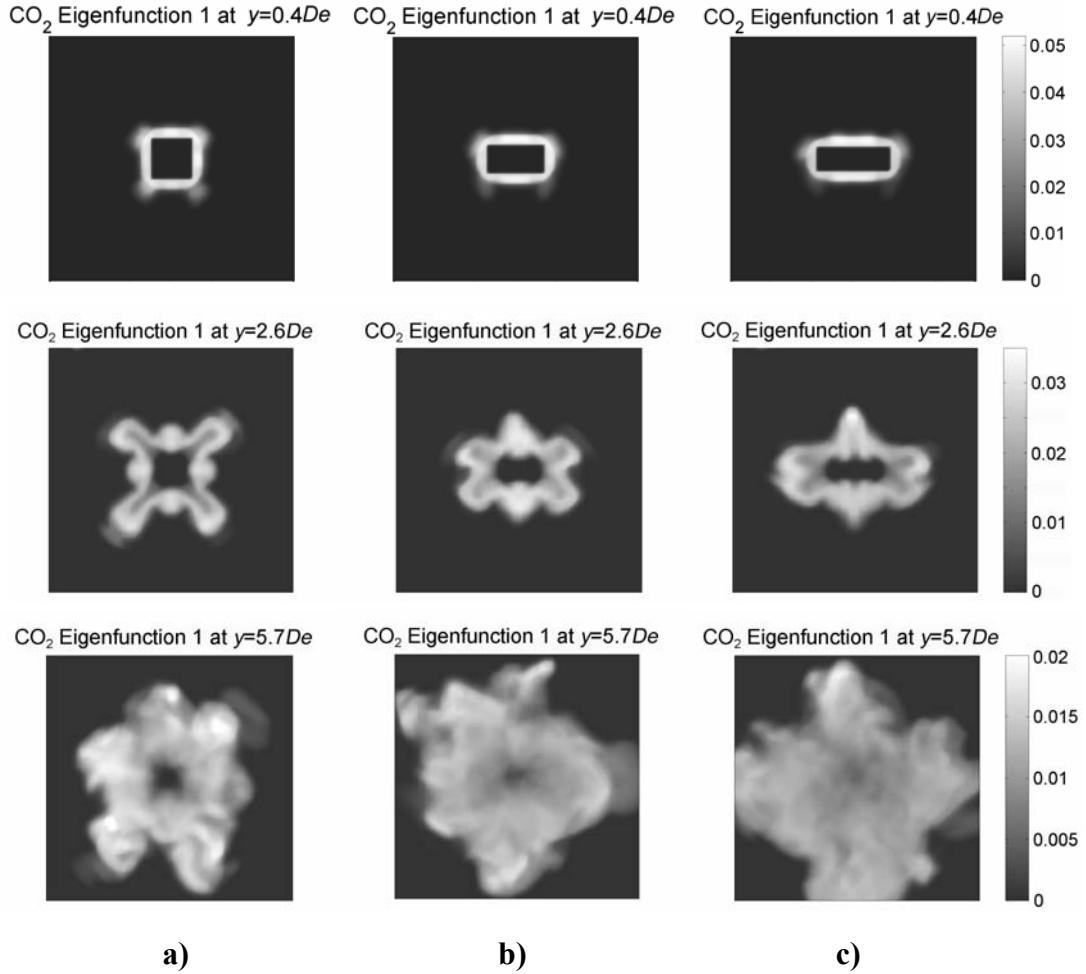


Figure 2.2. First eigenfunctions of CO₂ at $y=0.4De$ (top), $2.6De$ (middle), $5.7De$ (bottom) for a) AR=1; b) AR=2; and c) AR=3 jets. Notice the lobes that develop in the corner regions and the ridges that develop along the major sides of the jets.

the total information in the set of eigenfunctions at $0.4De$ and over 75% of the information at $5.7De$ for the aspect ratios considered. Close to the jet exit (at $0.4De$), the first eigenfunction for each jet shows some lobes beginning to develop near the corner regions of the jets. In the center of each eigenfunction is a rectangular region where no CO₂ is present, indicating the fuel region of the jet. At locations close to the jet exit, the first eigenfunctions are of similar shape for each aspect ratio jet. However, farther downstream (at $2.6De$), the eigenfunctions begin to differ due to

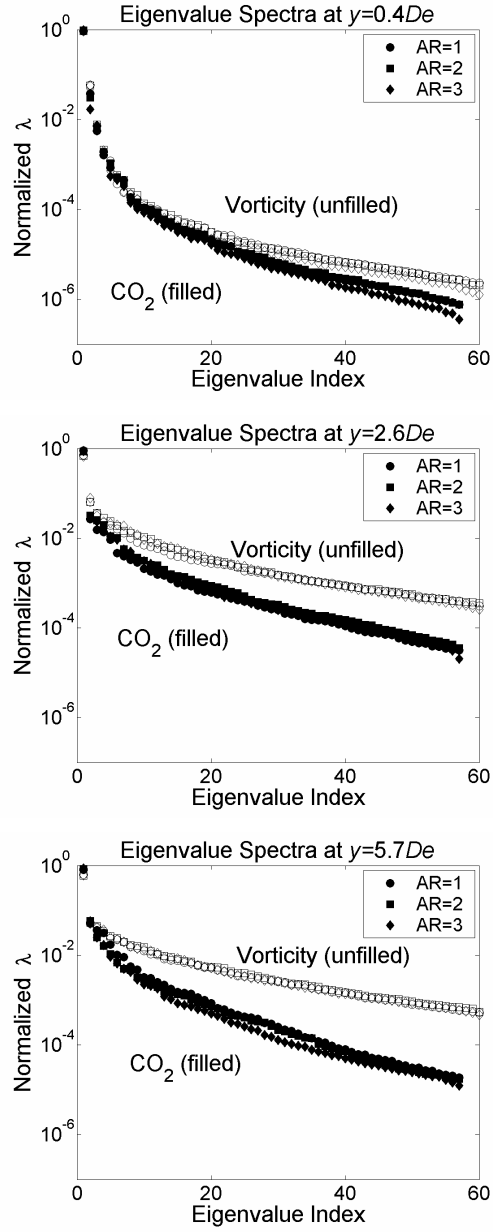


Figure 2.3. Eigenvalue spectra for CO₂ and vorticity eigenfunctions at $y=0.4De$ (top), $y=2.6De$ (middle), and $y=5.7De$ (bottom).

different vortex dynamics between the jets [43,44]. Lobes develop at the corners of each jet, however these lobes are far more pronounced for $AR=1$ than for $AR=2$ or 3. The lobes increase the spreading of the square jet in the corner regions over that of the rectangular jets at this axial location. For aspect ratios of 2 and 3, ridges develop

along the major sides of the rectangular jets that are less prominent in the case of the square jet. The peak levels of CO_2 are approximately the same in the eigenfunctions for the different aspect ratios, consistent with the results from numerical simulations of these jets.

Far downstream (at $5.7De$), the first CO_2 eigenfunctions are much more diffuse and complex. The lobes and ridges that are well defined at $y=2.6De$ have lost their definition and become more random. The eigenfunctions suggest better mixing and entrainment in the $AR=2$ and especially $AR=3$ jets compared to the square jet. This is evident in the more uniform concentration of the first eigenfunctions in the rectangular jets when compared to the square case and is due to more intense streamwise vorticity in these jets [43,44]. More extensive spreading of the CO_2 field in the $AR=3$ and, to some extent, the $AR=2$ jets is also noted at this axial location, in contrast to axial locations closer to the jet exit where there is enhanced spreading of the square jet. Note that the fuel core region remains visible even at these downstream locations.

2.4.2 Vorticity Magnitude

The first eigenfunctions of vorticity magnitude are displayed in Figure 2.4 for axial locations $y=0.4De$, $2.6De$, and $5.7De$ with the corresponding normalized eigenvalue spectra for these locations displayed in Figure 2.3. The second eigenfunctions of vorticity are displayed in Figure 2.5.

The eigenfunctions display well-defined vortex structures at $y=0.4De$ and $2.6De$. Vorticity magnitude data after vortex structure breakdown and transition to turbulence in the far jet is displayed at $5.7De$. The vorticity eigenfunctions also capture different vortex structures in the flow dependent upon the aspect ratio of the jet. The structures apparent in the corresponding eigenfunctions of $AR=2$ and 3 jets are similar to each other, however, different vortex structures are apparent in the

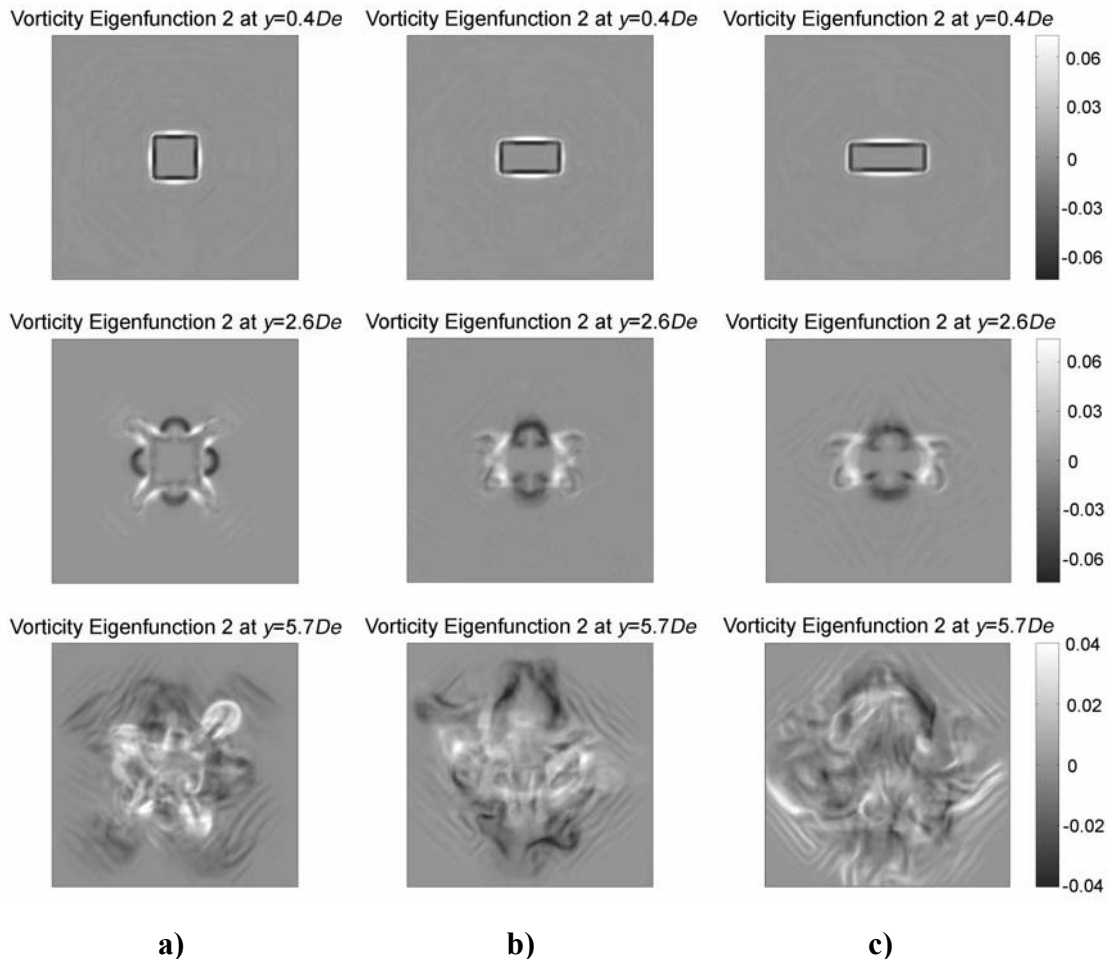


Figure 2.5. Second eigenfunctions of vorticity at $y=0.4De$ (top), $2.6De$ (middle), and $5.7De$ (bottom) for a) $AR=1$; b) $AR=2$; and c) $AR=3$ jets.

results indicate that different vorticity eigenfunctions can be associated with specific vortex orientations. For instance, the first eigenfunction at $y=2.6De$ (see Figure 2.4) appears to capture streamwise vorticity in the form of rib pairs for the square jet and single ribs aligned with corner regions in the rectangular jets. The rib pairs present in the square jet produce larger streamwise vorticity and larger jet spreading in the corner regions of the square jet than for the rectangular jets at $y=2.6De$, consistent with the spreading seen in the CO_2 eigenfunctions. The second eigenfunction appears to capture portions of the azimuthal vortex ring more strongly than other eigenfunctions,

as well as capturing additional streamwise vortex formations, including vortex ring distortion and rib pair coupling in the square jet. The third eigenfunction (not displayed) also captures primarily streamwise vorticity.

Comparisons of the first eigenfunctions of CO₂ and vorticity reveal similar shapes and nonzero spatial extent at each axial location. This is expected since it is vortex driven convective mixing that dominates in these reactive jets. Highly correlated entrainment and fuel burning rates are expected as the *AR* dependent coherent structures have an important role in jet spreading, mixing, and combustion [44].

Table 2.1. Percentage of information content of each CO₂ and vorticity magnitude eigenfunction presented.

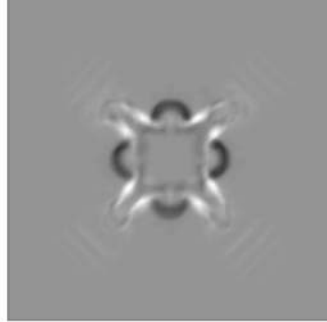
<i>Eigenfunction</i>	<i>AR</i>	<i>y=0.4De, %</i>	<i>y=2.6De, %</i>	<i>y=5.7De, %</i>
CO ₂ – 1 st	1	95.22	90.08	80.74
CO ₂ – 1 st	2	95.78	86.11	84.74
CO ₂ – 1 st	3	97.18	87.32	85.71
Vorticity – 1 st	1	92.97	71.94	61.86
Vorticity – 1 st	2	92.89	67.73	59.16
Vorticity – 1 st	3	93.26	67.29	60.95
Vorticity – 2 nd	1	5.78	6.43	5.05
Vorticity – 2 nd	2	5.76	6.38	5.36
Vorticity – 2 nd	3	5.69	7.83	5.09

2.4.3 Axis Switching

Studies have shown that as a rectangular jet spreads, the shape of its cross-section can evolve with downstream distance in such a way that the axes of the jet will rotate in ways determined by the jet geometry. As the jet spreads, it will contract in the direction of the major axis and expand in the direction of the minor axis. The cross section will evolve through an intermediate rhomboidal shape where the jet widths are equal in both directions, termed the crossover location. The axes of a square jet rotate 45 degrees while those of a rectangular jet rotate 90 degrees, interchanging the major and minor axes of the jet. This is denoted as axis-switching [43,44,56]. Rectangular jets passively improve mixing through enhanced entrainment due to axis-switching. Axial forcing of these jets is one way to make axis-switching more pronounced, by increasing the vortex ring strength and coherence [43,44].

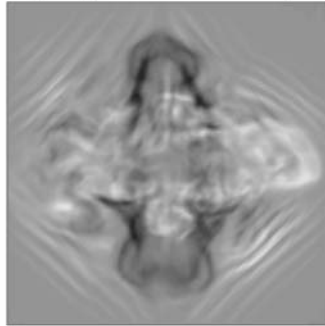
The streamwise location of axis-switching increases with aspect ratio. In the present results, axis-switching can be seen in several of the eigenfunctions in Figure 2.6. The eigenfunctions make axis-switching phenomena more apparent than individual distributions from the ensembles. For the $AR=1$ jet, the first axis switching occurs at approximately $y=2.5De$. The 45 degree rotated vortex ring and its influence can be seen in the first eigenfunctions of both vorticity and CO_2 . For the $AR=2$ jet, the first 90 degree axis-switching occurs at approximately $5De$ and can be seen in the second eigenfunction of vorticity at $y=4.8De$ in Figure 2.6. The first switching for the $AR=3$ jet occurs past $6.6De$. At the axial locations studied here, it is only possible to see the intermediate rhomboidal jet cross-section at the crossover location in the first eigenfunction of vorticity at $y=6.6De$ for the $AR=3$ jet. POD analyses were performed at the downstream locations chosen based on expected axis-switching distances in the three jets, determined in previous studies [43,44,57]. The switching distance for the $AR=1$ jet is expected to be approximately one-half and one-third of the distances for

Vorticity Eigenfunction 2 at $y=2.6De$



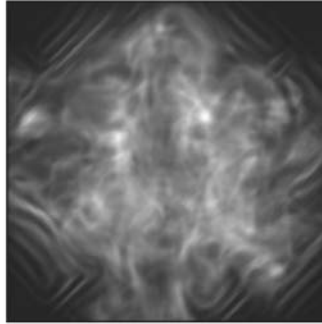
a)

Vorticity Eigenfunction 2 at $y=4.8De$



b)

Vorticity Eigenfunction 1 at $y=6.6De$



c)

Figure 2.6. Vorticity eigenfunctions displaying axis-switching in the three jets. a) Switching first occurs at $y=2.6De$ for $AR=1$; b) Switching first occurs at $y=4.8De$ for $AR=2$; c) Switching occurs past $y=6.6De$ for $AR=3$, intermediate rhomboidal shape at crossover is displayed here.

the $AR=2$ and $AR=3$ jets, respectively. This expectation is consistent with the results seen in the POD eigenfunctions.

2.4.4 Eigenvalue Spectra and the Potential for Reduced Modeling

Eigenvalue spectra for CO₂ and vorticity magnitude are shown in Figure 2.3 for the locations $y=0.4, 2.6,$ and $5.7De$. Near the jet exit, the spectra for both fields drop off rapidly indicating that the majority of information in each set of eigenfunctions is contained in the first few eigenfunctions. This indicates a strong potential for reduced order modeling using a small number of eigenfunctions to represent distributions contained in the ensembles of CO₂ and vorticity distributions. As axial distance from the jet increases (moving downstream) the information content of a subset of a fixed number of eigenfunctions decreases in each case, evident in the slower decrease in the eigenvalue spectra. At downstream locations more eigenfunctions are needed to capture the same amount of information that is present in a smaller number of eigenfunctions closer to the jet exit. This is a result of the evolution of the flow through transition to turbulence and breakup of large-scale structures, leading to an increase in complexity as measure by the required number of eigenfunctions necessary to represent the flow. The decrease of information in a given subset of eigenfunctions continues until approximately $y=4De$, beyond which point the information content of a subset of eigenfunctions remains approximately the same. The eigenfunctions, on the other hand, continue to change. This indicates that the CO₂ and vorticity fields have reached a constant level of complexity as measured by the information content of a fixed number of eigenfunctions.

At all axial locations, the eigenvalue spectra for the three different aspect ratio jets are approximately the same, indicating that about the same number of eigenfunctions are needed in each jet to capture a given amount of information. Comparing the CO₂ spectra and the vorticity magnitude spectra, it is seen that the information content of a subset of eigenfunctions of CO₂ is greater than the information content of the same number of vorticity eigenfunctions, more significantly

as distance from the jet exit is increased. Near the jet exit, CO₂ production is primarily governed by production in regions mixed through large-scale vortex formations, resulting in similar eigenfunctions and eigenvalue spectra for the two fields. Farther downstream, the CO₂ field is more diffuse and uniform as its presence is determined not only by production in mixed regions but also by convective and diffusive transport. Differences are seen in the eigenfunctions as vorticity eigenfunctions contain more small-scale structure than CO₂ eigenfunctions at these downstream locations (compare Figures 2.2 and 2.4), requiring use of additional vorticity eigenfunctions to capture the information in the flow. Hence, reduced order modeling based on a small number of eigenfunctions may be more feasible for the CO₂ field than for vorticity.

The development of a reduced order model is dependent on the ability of a limited number of basis functions to capture the flow physics and represent the important flow parameters. The POD eigenfunctions presented here are the most efficient basis set possible for this particular problem. A reduced order model could be developed through Galerkin projection of the governing equations of the flow onto the basis functions [18], resulting in a set of ordinary differential equations that describe the flow through the evolution of the associated time coefficients of each basis function. A reduced order model based on a subset of the most important eigenfunctions would require modeling of the small scale processes not captured by these eigenfunctions, however this would be true for any reduced order model. For control applications, input and output parameters may be represented by an expansion of basis functions and relations between these parameters used to develop a reduced order model using system identification methods or Galerkin projection of the governing equations. Development of a reduced order model for control is often system specific and can be highly dependent on the basis set utilized.

Relevant to this study, two-dimensional POD analysis of the flow provides a basis set for use with two-dimensional measurements of combustion parameters for tomographic or other applicable techniques. Measurements in the cross-stream direction allow for the study of axis-switching phenomena present in these jets. In a measurement context, three-dimensional measurements of quantities such as pressures, species concentrations, temperature, emission, etc. are often difficult and costly. One-dimensional or two-dimensional measurements are often made on a combustion system at fixed locations. Measurements of these quantities can then be used for feedback control of the system utilizing a reduced-order model based on the measured parameters at these fixed locations [11,13,25,58,59]. CO₂ eigenfunctions could be used to develop a model for CO₂ formation rate, which is proportional to the heat release rate and hence could be used in combustion instability studies. CO₂ eigenfunctions also can be used for tomographic analysis [28,37] and monitoring of a combustion system. Studies have shown that vortex dynamics are linked to sustaining combustion instabilities [10,14,46] indicating that development of a reduced order model based on vortex dynamics could be important for use in active combustion control. The results of the POD analysis presented here are representative of the jets under investigation and reflect the flow dynamics evident in the ensemble of distributions from which they were derived. Therefore, the eigenfunctions are specific to each jet and downstream location in this study, nonetheless, they are useful for developing models of these jets for use in combustion control applications where forced jets are of interest as actuators [3-7].

The information content of subsets of eigenfunctions, E_M , is quantified in Tables 2.2 and 2.3 for different axial locations. Because the eigenvalue spectra for the three jets are approximately the same at each axial location, average values of the information content of the three jets have been used.

Table 2.2. Comparison of information content of subsets of CO₂ eigenfunctions (average values for the three aspect ratio jets).

E_M	$y=0.4De, \%$	$y=2.6De, \%$	$y=5.7De, \%$
E_1	96.06	87.84	83.73
E_5	99.81	95.6	95.58
E_{10}	99.94	97.95	98.13

Table 2.3. Comparison of information content of subsets of vorticity eigenfunctions (average values for the three aspect ratio jets.)

E_M	$y=0.4De, \%$	$y=2.6De, \%$	$y=5.7De, \%$
E_1	93.04	68.99	60.66
E_5	99.78	83.98	76.04
E_{10}	99.91	90.54	84.79

A way to examine the representational capabilities of subsets of eigenfunctions is to calculate the best representation of a given distribution in the training set. The best representation of a distribution $n(x, z, t_k)$ using a subset of M eigenfunctions is given by

$$n(x, z, t_k) \approx \hat{n}(x, z, t_k) = \sum_{i=1}^M \beta_i(t_k) \phi_i(x, z) \quad (2.8)$$

where $\hat{n}(x, z, t_k)$ is the best representation using the first M eigenfunctions and $\beta_i(t_k)$ is the associated weighting factor for each eigenfunction ϕ_i at time t_k . The weighting factors are chosen to minimize the difference between the actual distribution and the

best representation of that distribution, i.e., to minimize the norm $\|n - \hat{n}\|$ given M eigenfunctions. The weighting factors are calculated by taking the inner product of the actual distribution with each eigenfunction. It is thus possible to reduce the representation problem to order M , where M is the number of eigenfunctions determined to give a sufficiently accurate representation of a distribution. Sirovich suggests defining the representational dimension as the number of eigenfunctions with eigenvalues greater than 1% of the first eigenvalue [27]. An expansion based on these eigenfunctions will capture at least 90% of the total information. For example, based on this concept, 10 vorticity eigenfunctions and 6 CO₂ eigenfunctions (capturing 91.5% and 97.0%, respectively) are necessary for the $AR=1$ jet at $y=2.6De$. The number of eigenfunctions needed for a particular model or representation will most likely be chosen based on the accuracy needed for a given application. Sample representations are presented in Figure 2.7 and Figure 2.8. The associated errors are quantified in Table 2.4 using the following error measures discussed in Reference 60.

1) Normalized rms error

$$e_{rms} = \frac{\|n(x_i, z_j) - \hat{n}(x_i, z_j)\|_F}{\|n(x_i, z_j) - \bar{n}\|_F} \quad (2.9)$$

where

$$\bar{n} = \sum_{i=1}^{N_x} \sum_{j=1}^{N_z} \frac{n(x_i, z_j)}{N_x N_z} \quad (2.10)$$

2) Normalized absolute error

$$e_{abs} = \frac{\sum_{i=1}^{N_x} \sum_{j=1}^{N_z} |n(x_i, z_j) - \hat{n}(x_i, z_j)|}{\sum_{i=1}^{N_x} \sum_{j=1}^{N_z} |n(x_i, z_j)|} \quad (2.11)$$

3) Normalized maximum error

$$e_{\max} = \frac{\max\left(|n(x_i, z_j) - \hat{n}(x_i, z_j)|\right)}{n(x_{\max}, z_{\max})} \quad (2.12)$$

Table 2.4. Errors in representations of chosen CO₂ and vorticity magnitude distributions using subsets of eigenfunctions are presented. Bold values indicate the representations presented in Figures 2.7 and 2.8.

<i>Distribution</i>	<i>M</i>	<i>e_{rms}</i>	<i>e_{abs}</i>	<i>e_{max}</i>
<i>CO₂, 2.6De</i>	2	0.2894	0.2203	2.9508
	4	0.2030	0.1526	0.6853
	6	0.1640	0.1255	0.7915
	8	0.1450	0.1126	0.7070
	10	0.1256	0.0981	0.6143
	12	0.1196	0.0911	0.5912
<i>Vorticity, 2.6De</i>	2	0.4516	0.4403	0.8169
	4	0.4469	0.4515	0.8135
	6	0.3009	0.2688	0.3825
	8	0.2717	0.2512	0.9630
	10	0.2576	0.2242	0.4230
	12	0.2517	0.2116	0.4154

2.5 Summary and Conclusions

Proper orthogonal decomposition has been used to analyze ensembles of two-dimensional distributions of concentration and vorticity magnitude in forced reacting rectangular jets of aspect ratios 1-3. The ensembles were constructed at various downstream locations using CO₂ concentration and vorticity magnitude data obtained

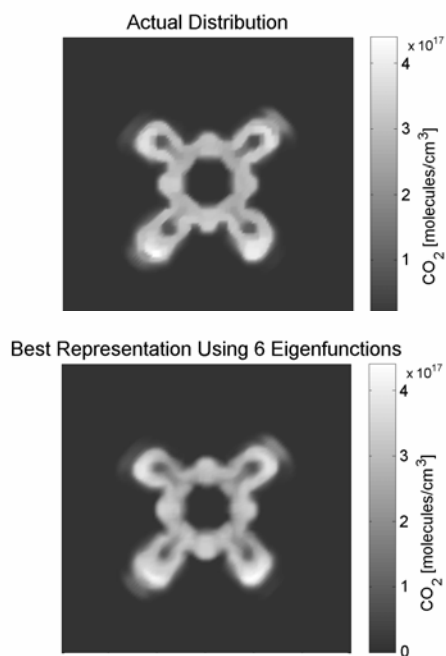


Figure 2.7. Representation results using 6 eigenfunctions of a representative CO₂ distribution in the square jet at $y=2.6De$.

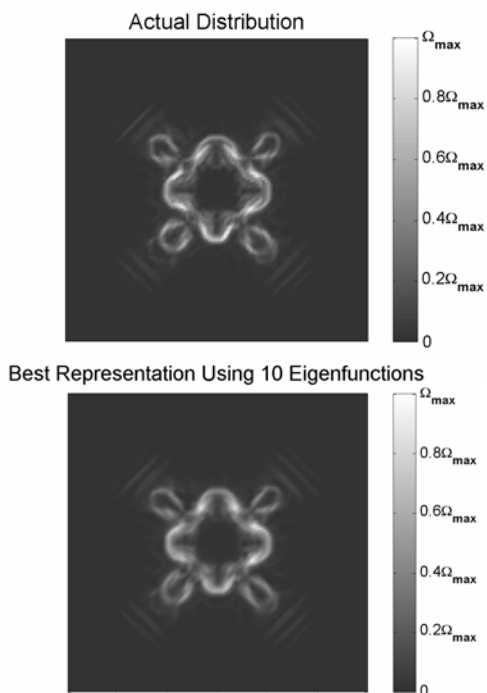


Figure 2.8. Representation results using 10 eigenfunctions of a representative vorticity magnitude distribution in the square jet at $y=2.6De$.

by computation; they contained 60 and 63 members, respectively. Proper orthogonal decomposition produced sets of eigenfunctions useful for investigating the large-scale features of the flow, and eigenvalues used to evaluate the information content of the eigenfunctions and the potential for reduced-order modeling of these combustion variables using a limited number of basis functions. While not part of this investigation, spectral analysis of the POD derived time coefficients could be used to investigate the temporal contributions of individual eigenfunctions and to gain insight into the dynamics of the flow.

Results of proper orthogonal decomposition applied to CO₂ concentration and vorticity magnitude distributions show CO₂ eigenfunctions and vorticity eigenfunctions of similar shapes and nonzero spatial extent, consistent with the understanding that vortex driven mixing dominates in these jets. The results show similar eigenfunctions for the different aspect ratio jets at locations near the jet exit. However, the similarity decreases as downstream distance from the jet exit increases. The differences are evident in the different vortex structures that are captured in the rectangular jets and square jet eigenfunctions, e.g. single ribs located in corner regions of the rectangular jets as opposed to rib pairs present in the square jet, and result from the inherent differences in the vortex dynamics of these jets. Differences in the extent of the spreading of the CO₂ eigenfunctions between the rectangular and square jets are also displayed, resulting from the different vortex structures mentioned above. The vorticity eigenfunctions can be associated to some extent with different vortex orientations, e.g. the first eigenfunction appears more correlated with streamwise vorticity while the second eigenfunction is more correlated with the azimuthal vortex ring. Axis-switching is evident in the eigenfunctions at axial locations that are consistent with expectations, e.g., axis-switching distances increase with aspect ratio. While new structures or flow physics have not been revealed

through the POD analysis, it is useful in the interpretation of the LES results as it eliminates the need for detailed analysis of many timesteps. Large-scale structures are easily identified in the POD results and phenomena such as axis-switching are readily apparent.

Eigenvalue spectra and eigenfunction information content are examined at various downstream locations. Near the jet exit, the spectra for both CO₂ and vorticity magnitude show that the majority of the information contained in the eigenfunctions is present in the first few eigenfunctions of CO₂ and vorticity, which indicates a good potential for reduced-order modeling at this axial location. However, the complexity of the CO₂ and vorticity eigenfunctions increases as distance from the jet exit increases up to approximately $y=4De$. This indicates that additional eigenfunctions would be necessary for reduced-order modeling at locations farther downstream and the potential for reduced-order modeling based on a small set of eigenfunctions at these locations is less than that near the jet exit. After approximately $4De$, evaluation of the eigenfunction information content and the eigenvalue spectra suggests that a constant level of complexity in the flow has been reached. This is evident in the near constant amount of information content contained in a fixed number of eigenfunctions as distance from the jet exit is increased past this location. It is also noted that at each axial location the eigenvalue spectra are approximately the same for the different aspect ratio jets, indicating that a similar amount of information is contained in a fixed number of eigenfunctions for each of the jets. However, the information content of a fixed number of CO₂ eigenfunctions is greater than the information content of the same number of vorticity eigenfunctions, indicating a greater potential for reduced-order modeling of the CO₂ concentration field. As a result, more vorticity eigenfunctions are needed to accurately represent a vorticity distribution from the

ensemble than the number required for a representation of a CO₂ distribution of the same accuracy.

In this paper, we have investigated the results of proper orthogonal decomposition analysis on unsteady, reacting rectangular jets. Through evaluation of the eigenvalue spectra and eigenfunction information content, we have determined that there is a stronger potential for reduced-order modeling of the CO₂ field than for the vorticity field, while these potentials are approximately the same for the three rectangular jets studied. We have gained physical insight through examination of the resulting eigenfunctions, specifically relating to vortex structures and the development of the CO₂ concentration field through mixing and spreading at locations downstream from the jet exit. Axis-switching phenomena and the influence of vortex dynamics on mixing are also evident in the POD eigenfunctions.

Appendix A

Grid Resolution Issues

The computational domains used in the original simulations in Reference 44 had streamwise lengths between $7De-10De$ and extended up to $5De-10De$ away from the jet axis in the transverse directions. Various grids were used in the original simulations; for $AR=1$, for example, the number of grid points ranged between $87 \times 112 \times 87$ (spacing 2Δ) to $174 \times 225 \times 174$ (spacing Δ), with most of the simulations typically carried out on computationally convenient grids at the intermediate resolution 1.5Δ ; the smallest cell size considered was $\Delta=De/42$ [43,44]. In all cases, the timestep used in the temporal integration was determined as a function of the smallest grid spacing based on a fixed Courant number of 0.4. The computational grids used evenly spaced cells in the shear flow region of interest. Geometrical grid stretching in the cross-stream direction outside of the latter region was used to implement the open boundary conditions there [43]. The data used for the POD analysis on the rectangular jets in this investigation were generated at the intermediate resolution with characteristic spacing 1.5Δ . Datasets were obtained from similar simulations of a non-reacting square jet carried out on the finest and coarsest such grids. Because the vortex dynamics and topology of the reacting rectangular and non-reacting square jets are similar and the Reynolds number regime is the same, the non-reacting square jet simulations are applicable to address grid resolution issues in what follows.

Because we are dealing here with LES (as opposed to DNS), the meaningful issue to be addressed is convergence of the largest scales of the simulated flow. Figure 2.9 compares vorticity distributions on streamwise planes passing through the jet axis;

run “rc40” was carried out on the $174 \times 225 \times 174$ grid with one-half the mesh spacing of the $87 \times 112 \times 87$ “rc36” grid; the finest-resolved vorticity data were interpolated onto a grid with the same spacing as the coarsest to generate the frames in Figure 2.9. Comparison of snapshots at representative selected times in Figure 2.9, indicates that the large-scale features are virtually identical in the first few diameters of streamwise extent, say, up to a transitional location of $y_o \approx 2.75De$; downstream of which differences are more apparent, reflecting significantly more smaller-scale features captured on the finest grid after transition to turbulence – which also affect the large scales of the simulated flow.

Figures 2.10 and 2.11 examine the grid resolution issues from the perspective of POD analysis. Analysis is based on the available vorticity simulation data from runs rc40 and rc36 at 10 equally-spaced timesteps, over a time interval spanning two forcing periods – significantly less than that used in the POD analysis presented above (60 samplings over six forcing periods). A large number of distributions is desirable for POD analysis and additional grids would allow for more comprehensive convergence studies, however the production of numerous distributions on different LES grids is computationally intensive and thus we have chosen to use pre-existing simulation data for the present grid resolution studies [43-45].

POD analysis is useful for investigating grid resolution issues in an unsteady process, as differences in the flow resulting from changes in the simulation grid will alter both the resulting eigenfunctions and eigenvalue spectra. The specific nature of the eigenfunctions makes them useful as a mechanism for determining the adequacy of LES resolution through evaluation of the small-scale information captured in the eigenfunctions and the associated eigenvalue spectra. Changes in the eigenvalue spectra caused by differing amounts of small-scale information captured on the different grids are useful in evaluating grid resolution. The relevant quantity to be

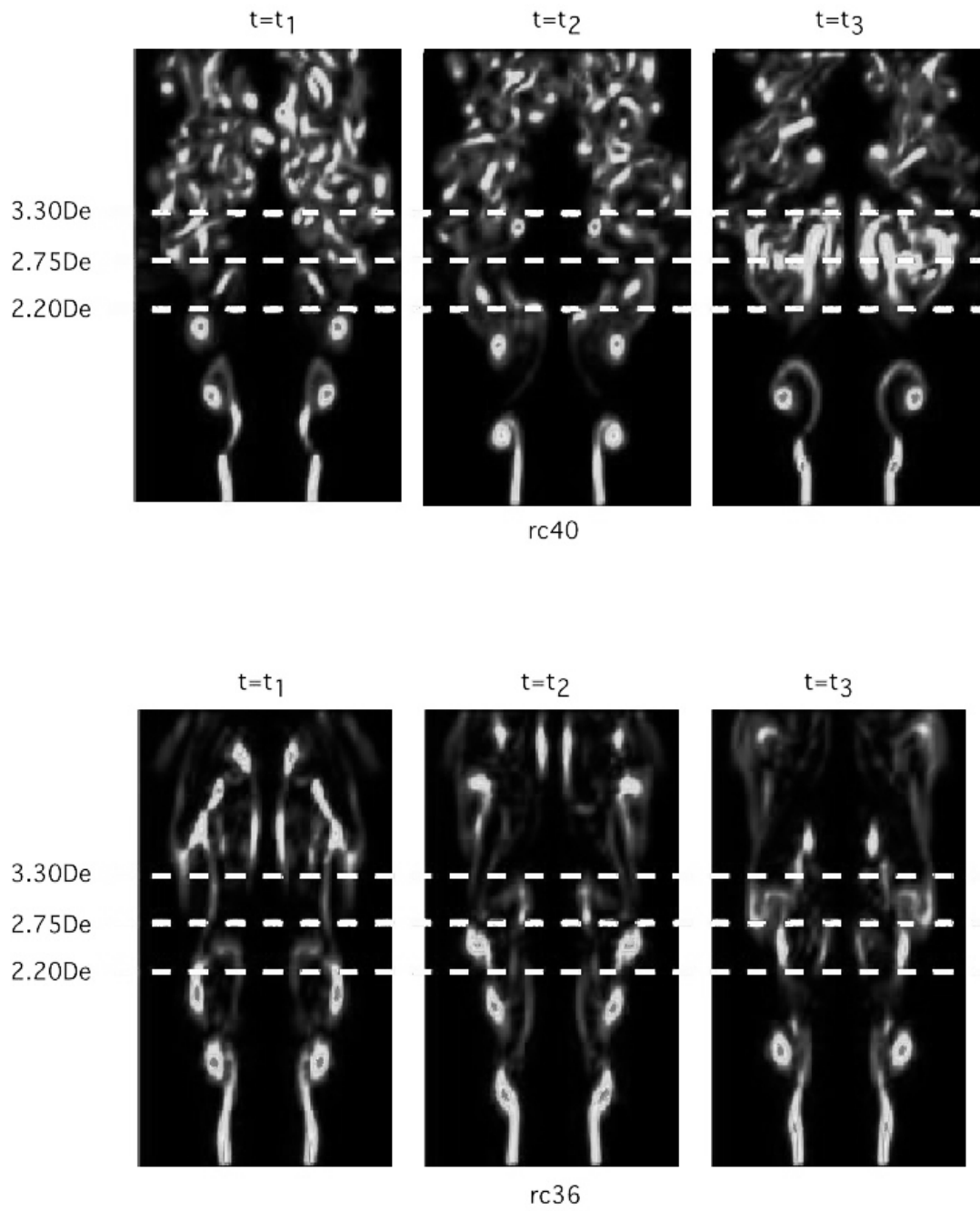


Figure 2.9. Vorticity distributions on streamwise planes passing through the jet axis for run rc40 (top) and run rc36 (bottom).

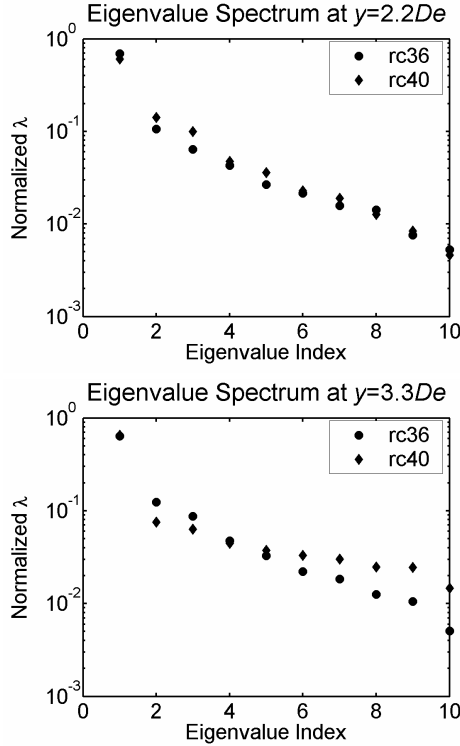
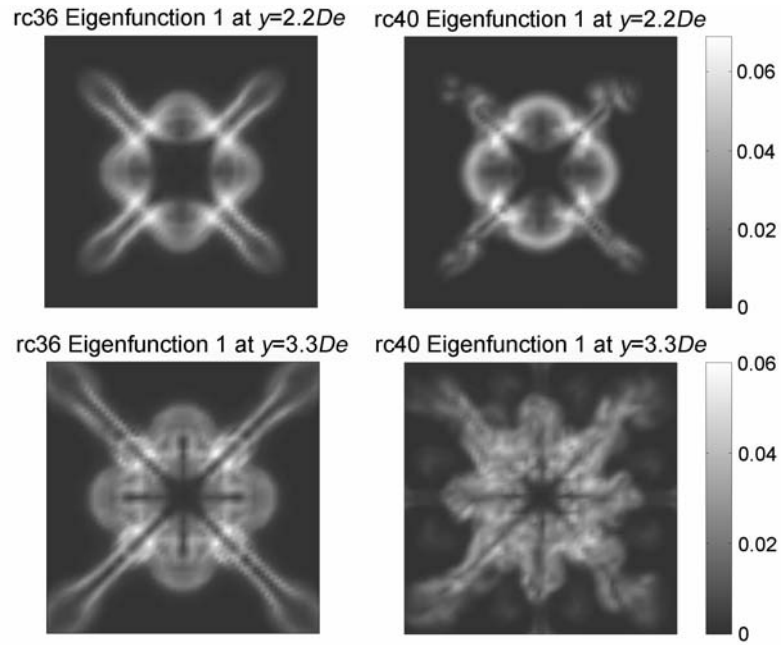


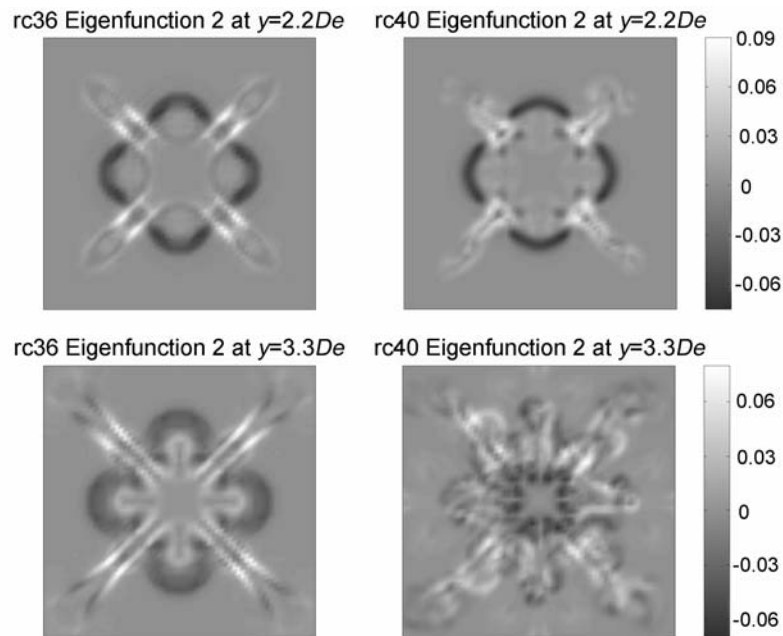
Figure 2.10. Normalized eigenvalue spectra at $y_1=2.2De$ (top) and $y_2=3.3De$ (bottom).

computed is the amount of information contained in a subset of eigenfunctions as deduced from the eigenvalue spectra. By comparison of a subset of eigenfunctions resulting from POD analysis of different grid resolutions, if the eigenvalue spectra are suitably similar for the different grids, one can determine a measure of grid resolution suitability based on the amount of information contained in the subset of eigenfunctions.

Figure 2.10 compares the normalized eigenvalue spectra at two relevant streamwise locations, $y_1=2.2De < y_o$ and $y_2=3.3De > y_o$. By design, y_1 and y_2 were chosen to straddle the transitional location $y=y_o$. The two eigenvalue spectra compare favorably at $y=y_1$, but somewhat less favorably at $y=y_2$, especially at higher index number. In Figure 2.11, large-scale coherent structures are seen in the eigenfunctions resulting from the coarsely gridded rc36 simulation. The lack of small-scale



a)



b)

Figure 2.11. a) First eigenfunctions of vorticity for rc36 jet (left) and rc40 jet (right) at $y_1=2.2De$ (top) and $y_2=3.3De$ (bottom); b) Second eigenfunctions of vorticity for rc36 and rc40 jets at $y_1=2.2De$ (top) and $y_2=3.3De$ (bottom).

information in the rc36 eigenfunctions results in a fast decline in the eigenvalue spectra at both downstream locations. This simulation is capable of capturing the large-scale vorticity formations but is unable to capture the smallest scale coherent structures, the high intensity “worm” vortices as described in Reference 44. The finely gridded rc40 simulation is able to resolve the worm vortices and thus captures more small-scale information in the flow. These small-scale structures can be seen in the resulting eigenfunctions in Figure 2.11 and cause the flattening of the rc40 eigenvalue spectrum as information is shifted from the lower to the higher eigenfunctions, seen in Figure 2.10 at $y_2=3.3De$. At the downstream location y_1 , the eigenvalue spectra for the two simulations are similar and a subset of the first four eigenfunctions captures approximately 90% of the information in the flow for each simulation. Farther downstream at y_2 , the same subset of eigenfunctions captures approximately 90% of the information in the rc36 simulation but only 83.5% of the information in the rc40 simulation. Comparison of the information content on additional grids would allow for further evaluation of grid resolution; the convergence features are likely to depend on ensemble specifics (e.g. number of samplings involved, downstream location, etc.).

Appendix B

Proper Orthogonal Decomposition Matrix Formulation

The matrix formulation of the POD is presented following the formulation in Ref. 27. As stated in the main text, consider an ensemble of distributions $\{n\}$. An individual distribution is a scalar function of position and time, $n(x,z,t_k)$, and can be written as $n^k(\mathbf{x})$. Consider \mathbf{C} as a matrix containing the ensemble distributions $\{n^k(\mathbf{x})\}$ such that each member of the ensemble is contained in a row of \mathbf{C} of length $N_p=N_x \times N_z$ resulting in a $N_t \times N_p$ matrix.

$$\mathbf{C} = \begin{bmatrix} n^1(\mathbf{x}) \\ \vdots \\ n^{N_t}(\mathbf{x}) \end{bmatrix} \quad (2.13)$$

We seek a system of orthonormal functions $\{\phi^k(\mathbf{x})\}$ such that

$$(\phi^k(\mathbf{x}), \phi^l(\mathbf{x})) = \int_{\Omega} \phi^k(\mathbf{x}) \phi^l(\mathbf{x}) d\mathbf{x} = \delta_{kl}. \quad (2.14)$$

Consider a $N_t \times N_p$ matrix Φ such that each row is a vector denoting a member of the set $\{\phi^k(\mathbf{x})\}$.

$$\Phi = \begin{bmatrix} \phi^1(\mathbf{x}) \\ \vdots \\ \phi^{N_t}(\mathbf{x}) \end{bmatrix} \quad (2.15)$$

The set $\{\phi\}$ can then be normalized according to $\Phi \mathbf{G} \Phi^T = \mathbf{I}$. \mathbf{G} is an “integration” matrix used to approximate the spatial integration of a function in the x and z directions using the trapezoidal rule. The members of $\{\phi\}$ are chosen such that

$$\lambda_k = \left\langle (\phi^k, n)^2 \right\rangle = \frac{1}{N_t} \sum_{m=1}^{N_t} (\phi^k, n^m)^2 \quad (2.16)$$

is a maximum.

The *method of snapshots* calculates ϕ as an admixture of distributions, i.e. “snapshots” in the ensemble [27].

$$\phi = \sum_{k=1}^{N_t} a_k n^k \quad (2.17)$$

A two-time correlation matrix \mathbf{D} is formulated according to

$$D_{jk} = \frac{1}{N_t} (n^j(\mathbf{x}), n^k(\mathbf{x})) = \frac{1}{N_t} \int_{\Omega} n^j(\mathbf{x}) n^k(\mathbf{x}) d\mathbf{x} \quad (2.18)$$

leading to the matrix equation $\mathbf{D} = (1/N_t) \mathbf{C} \mathbf{G} \mathbf{C}^T$, where \mathbf{D} is a $N_t \times N_t$ matrix. The coefficients $\{a_k\}$ are determined through solution of the eigenvalue problem

$$\sum_{k=1}^{N_t} D_{jk} a_k = \lambda a_j. \quad (2.19)$$

This can be written in matrix form as $\mathbf{D} \mathbf{A} = \mathbf{\Lambda} \mathbf{A}$, where \mathbf{A} is a $N_t \times N_t$ matrix, each row of which contains the time coefficients for all eigenfunctions at a timestep and $\mathbf{\Lambda}$ is a diagonal $N_t \times N_t$ matrix containing the eigenvalues. This is the resulting eigenvalue problem presented in the main text.

Acknowledgements

This work was supported by the Office of Naval Research under ONR contract #N00014-99-1-0447.

References

- [1] Gutmark, E., and Grinstein, F., "Flow Control with Noncircular Jets," *Annual Review of Fluid Mechanics*, Vol. 31, 1999, pp. 239-72.
- [2] Gutmark, E., Parr, T., Wilson, K., and Schadow, K., "Active Control in Combustion Systems with Vortices," *Proceedings of the 1995 IEEE Conference on Control Applications*, Institute of Electrical and Electronics Engineers, Inc., New York, 1995, pp. 679-684.
- [3] Hathout, J., Fleifil, A., Annaswamy, A., and Ghoniem, A., "Role of Actuation in Combustion Control," *Proceedings of the 1999 IEEE International Conference on Control Applications.*, Institute of Electrical and Electronics Engineers, Inc., New York, 1999, pp. 213-218.
- [4] Hathout, J.P., Fleifil, M., Annaswamy, A.M., and Ghoniem, A.F., "Heat Release Actuation for Control of Mixture-Inhomogeneity-Driven Combustion Instability," *Proceedings of the Combustion Institute*, Vol. 28, The Combustion Institute, Pittsburgh, 2000, pp. 721-730.
- [5] Murugappan, S., Gutmark, E.J., Acharya, S., and Krstic, M., "Extremum-Seeking Adaptive Controller for Swirl-Stabilized Spray Combustion," *Proceedings of the Combustion Institute*, Vol. 28, The Combustion Institute, Pittsburgh, 2000, pp. 731-737.
- [6] Lee, J.G., Kim, K. and Santavicca, D., "Effect of Injection Location on the Effectiveness of Active Control System Using Secondary Fuel Injection," *Proceedings of the Combustion Institute*, Vol. 28, The Combustion Institute, Pittsburgh, 2000, pp. 739-746.
- [7] Johnson, C., Neumeier, Y., Lieuwen, T., and Zinn, B., "Experimental Determination of the Stability Margin of a Combustor Using Exhaust Flow and Fuel Injection Rate Modulations," *Proceedings of the Combustion Institute*, Vol. 28, The Combustion Institute, Pittsburgh, 2000, pp. 757-763.
- [8] Candel, S., "Combustion Dynamics and Control: Progress and Challenges," *Proceedings of the Combustion Institute*, Vol. 29, The Combustion Institute, Pittsburgh, 2002, pp. 1-28.
- [9] Ghoniem, A.F., Annaswamy, A., Wee, D., Yi, T., and Park, S., "Shear Flow-Driven Combustion Instability: Evidence, Simulation, and Modeling," *Proceedings of the Combustion Institute*, Vol. 29, The Combustion Institute, Pittsburgh, 2002, pp. 53-60.

- [10] Paschereit, C.O., and Gutmark, E.J., "Enhanced Performance of a Gas-Turbine Combustor Using Miniature Vortex Generators," *Proceedings of the Combustion Institute*, Vol. 29, The Combustion Institute, Pittsburgh, 2002, pp. 123-129.
- [11] Park, S., Wachsman, A., Annaswamy, A., Ghoniem, A.F., Pang, B., and Yu, K.H., "Experimental Study of POD-based Control for Combustion Instability Using a Linear Photodiode Array," *AIAA Paper 2004-0639*, January 2004.
- [12] Hathout, J.P., Annaswamy, A., Fleifil, M., and Ghoniem, A.F., "A Model-Based Active Control Design for Thermoacoustic Instability," *Combustion Science and Technology*, Vol. 132, 1998, pp.99-138.
- [13] Billoud, G., Galland, M.A., Huu, C.H., and Candel, C., "Adaptive Active Control of Combustion Instabilities," *Combustion Science and Technology*, Vol. 81, 1992, pp.257-283.
- [14] Fureby, C., "A Computational Study of Combustion Instabilities due to Vortex Shedding," *Proceedings of the Combustion Institute*, Vol. 28, The Combustion Institute, Pittsburgh, 2000, pp. 783-791.
- [15] Annaswamy, A.M. and Ghoniem, A.F., "Active Control in Combustion Systems," *IEEE Control Systems Magazine*, Vol. 15, Issue 6, 1995, pp. 49-63.
- [16] Smaoui, N. "Linear versus nonlinear dimensionality reduction of high-dimensional dynamical systems," *SIAM Journal on Scientific Computing*, Vol. 25, No. 6, 2004, pp. 2107-2125.
- [17] Norman, D.E. "Chemically reacting fluid flows: Weak solutions and global attractors," *Journal of Differential Equations*, Vol. 152, Issue 1, 1999, pp.75-135.
- [18] Holmes, P., Lumley, J., and Berkooz, G., *Turbulence, Coherent Structures, Dynamical Systems and Symmetry*, Cambridge Univ. Press, New York, 1996, Ch. 3.
- [19] Graham, W.R., Peraire, J., and Tang, K.Y., "Optimal Control of Vortex Shedding Using Low Order Models. Part I – Open-Loop Model Development," *International Journal for Numerical Methods in Engineering*, Vol. 44, No. 7, 1999, pp. 945-972.
- [20] Baker, J. and Christofides, P.D., "Finite-dimensional Approximation and Control of Non-linear Parabolic PDE Systems," *International Journal of Control*, Vol 73, No. 5, 2000, pp. 439-456.

- [21] Ravindran, S.S., "A Reduced-order Approach for Optimal Control of Fluids Using Proper Orthogonal Decomposition," *International Journal for Numerical Methods in Fluids*, Vol. 34, No. 5, 2000, pp. 425-448.
- [22] Zheng, D., Hoo, K.A., and Piovoso, M.J., "Low-order Model Identification of Distributed Parameter Systems by a Combination of Singular Value Decomposition and the Karhunen-Loeve Expansion," *Industrial and Engineering Chemistry Research*, Vol. 41, No. 6, 2002, pp. 1545-1556.
- [23] Fogleman, M., Lumley, J., Rempfer, D., and Haworth, D., "Application of the Proper Orthogonal Decomposition to Datasets of Internal Combustion Engine Flows," *Journal of Turbulence*, Vol. 5, Art. No. 023, 2004.
- [24] Gillies, E.A., "Low-dimensional Control of the Circular Cylinder Wake," *Journal of Fluid Mechanics*, Vol. 371, 1998, pp. 157-178.
- [25] Annaswamy, A., Choi, J.J., Sahoo, D., Alvi, F.S., and Lou, H., "Active Closed-Loop Control of Supersonic Impinging Jet Flows Using POD Models," *Proceedings of the 41st IEEE Conference on Decision and Control*, Institute of Electrical and Electronics Engineers, Inc., New York, 2002, pp. 3294-3299.
- [26] Berkooz, G., Holmes, P., and Lumley, J.L., "The Proper Orthogonal Decomposition in the Analysis of Turbulent Flows," *Annual Review of Fluid Mechanics*, Vol. 25, 1993, pp. 539-575.
- [27] Sirovich, L., and Emerson, R., "Management and Analysis of Large Scientific Datasets," *International Journal of Supercomputer Applications*, Vol. 6, 1992, pp. 50-68.
- [28] Tornianen, E., *Tomographic Reconstruction Using a Karhunen-Loeve Basis*, Ph.D. Dissertation, Cornell University, Ithaca, NY, May 2000.
- [29] Lumley, J., "The Structure of Inhomogeneous Turbulent Flows," *Atmospheric Turbulence and Radio Wave Propagation*, Nauka, Moscow, 1967, pp. 166-178.
- [30] Gunes, H., "Low-Dimensional Modeling of Non-Isothermal Twin-Jet Flow," *International Communications in Heat and Mass Transfer*, Vol. 29, No. 1, 2002, pp. 77-86.
- [31] Frouzakis, C., Kevrekidis, Y., Lee, J., Boulouchos, K., and Alonso, A., "Proper Orthogonal Decomposition of Direct Numerical Simulation Data: Data Reduction and Observer Construction," *Proceedings of the Combustion Institute*, Vol. 28, The Combustion Institute, Pittsburgh, 2000, pp. 75-81.

- [32] Bernero, S., and Fiedler, H., "Application of Particle Image Velocimetry and Proper Orthogonal Decomposition to the Study of a Jet in a Counterflow," *Experiments in Fluids*, Vol. 29, No. 7, 2000, pp. S274-S281.
- [33] Patte-Rouland, B., Lalizel, G., Moreau, J., and Rouland, E. "Flow Analysis of an Annular Jet by Particle Image Velocimetry and Proper Orthogonal Decomposition," *Measurement Science and Technology*, Vol. 12, No. 9, 2001, pp. 1401-1412.
- [34] Citriniti, J., and George, W., "Reconstruction of the Global Velocity Field in the Axisymmetric Mixing Layer Utilizing the Proper Orthogonal Decomposition," *Journal of Fluid Mechanics*, Vol. 418, 2000, pp. 137-166.
- [35] Faghani, D., Sevrain, A., and Boisson, H. "Physical Eddy Recovery through Bi-Orthogonal Decomposition in an Acoustically Forced Plane Jet," *Flow, Turbulence, and Combustion*, Vol. 62, No. 1, 1999, pp. 69-88.
- [36] Yilmaz, T., and Kodal, A. "An Investigation of Forced Structures in Turbulent Jet Flows," *Experiments in Fluids*, Vol. 29, No. 6, 2000, pp. 564-572.
- [37] Tornianen, E., Hinz, A., and Gouldin, F., "Tomographic Analysis of Unsteady Reacting Flows: Numerical Investigation," *AIAA Journal*, Vol. 36, No. 7, 1998, pp. 1270-1278.
- [38] Sirovich, L., Kirby, M., and Winter, M. "An Eigenfunction Approach to Large Scale Transitional Structures in Jet Flow," *Physics of Fluids A*, Vol. 2, No. 2, 1990, pp. 127-136.
- [39] Pelliccia-Kraft, J., and Watt, D. "Visualization of Coherent Structure in Scalar Fields of Unsteady Jet Flows with Interferometric Tomography and Proper Orthogonal Decomposition," *Experiments in Fluids*, Vol. 30, No. 6, 2001, pp. 633-644.
- [40] Winter, M., Barber, T., Everson, R., and Sirovich, L., "Eigenfunction Analysis of Turbulent Mixing Phenomena," *AIAA Journal*, Vol. 30, No. 7, 1992, pp. 1681-1688.
- [41] Aubry, N., Holmes, P., Lumley, J., and Stone, E., "The Dynamics of Coherent Structures in the Wall Region of a Turbulent Boundary Layer," *Journal of Fluid Mechanics*, Vol. 192, 1988, pp. 115-173.
- [42] Moehlis, J., Smith, T.R., Holmes, P., and Faisst, H., "Models for Turbulent Plane Couette Flow Using the Proper Orthogonal Decomposition," *Physics of Fluids*, Vol. 14, Issue 7, 2002, pp. 2493-2507.

- [43] Grinstein, F., "Coherent Structure Dynamics and Transition to Turbulence in Rectangular Jet Systems," *AIAA Paper 99-3506*, June 1999.
- [44] Grinstein, F., "Vortex Dynamics and Entrainment in Rectangular Free Jets," *Journal of Fluid Mechanics*, Vol. 437, 2001, pp. 69-101.
- [45] Grinstein, F.F., and DeVore, C.R., "Dynamics of Coherent Structures and Transition to Turbulence in Free Square Jets," *Physics of Fluids*, Vol. 8, No. 5, 1996, pp.1237-1251.
- [46] Pang, B., Yu, K.H., Park, S., Wachsman, A., Annaswamy, A.M., and Ghoniem, A.F., "Characterization and Control of Vortex Dynamics in an Unstable Dump Combustor," *AIAA Paper 2004-1162*, January 2004.
- [47] Grinstein, F., and Kailasanath, K., "Exothermicity and Three-Dimensional Effects in Unsteady Propane Square Jets," *26th International Symposium on Combustion*, The Combustion Institute, Pittsburgh, 1996, pp. 91-96.
- [48] Fureby, C., and Grinstein, F.F., "Monotonically Integrated Large Eddy Simulation of Free Shear Flows," *AIAA Journal*, Vol. 37, No. 5, 1999, pp.544-556.
- [49] Grinstein, F.F., and Guirguis, R.H., "Effective Viscosity in the Simulation of Spatially Evolving Shear Flows with Monotonic FCT Models," *Journal of Computational Physics*, Vol. 101, No. 1, 1992, pp.165-175.
- [50] Grinstein, F.F., and Kailasanath, K., "Chemical Energy Release and Dynamics of Transitional, Reactive Shear Flows," *Physics of Fluids A*, Vol. 4, No. 10, 1992, pp.2207-2221.
- [51] Fureby, C., and Grinstein, F.F., "Large Eddy Simulation of High-Reynolds-Number Free and Wall-Bounded Flows," *Journal of Computational Physics*, Vol. 181, 2002, pp. 68-97.
- [52] Grinstein, F.F. and Fureby, C., "From Canonical to Complex Flows: Recent Progress on Monotonically Integrated LES," *Computing in Science and Engineering*, Vol. 6, Issue 2, 2004, pp. 37-49.
- [53] Westbrook, C., and Dryer, F., "Simplified Reaction Mechanisms for the Oxidation of Hydrocarbon Fuels in Flames," *Combustion Science and Technology*, Vol. 27, No. 1-2, 1981, pp. 31-43.
- [54] Peters, N., *Turbulent Combustion*, Cambridge University Press, Cambridge, 2000, Ch. 1.

- [55] Williams, F.A., *Combustion Theory*, Benjamin/Cummins, Menlo Park, CA, 1985.
- [56] Zaman, K., "Axis Switching and Spreading of an Asymmetric Jet: the Role of Coherent Structure Dynamics," *Journal of Fluid Mechanics*, Vol. 316, 1996, pp. 1-27.
- [57] Grinstein, F.F., "Self-induced Vortex Ring Dynamics in Subsonic Rectangular Jets," *Physics of Fluids*, Vol. 7, No.10, 1995, pp. 2519-2521.
- [58] Dunstan, W.J., Bitmead, R.R., and Savaresi, S.M., "Fitting Nonlinear Low-Order Models for Combustion Instability Control," *Control Engineering Practice*, Vol. 9, 2001, pp. 1301-1317.
- [59] Furlong, E.R., Baer, D.S., and Hanson, R.K., "Real-Time Adaptive Combustion Control Using Diode-Laser Absorption Sensors," *Twenty-Seventh Symposium (International) on Combustion*, The Combustion Institute, Pittsburgh, 1998, pp.103-111.
- [60] Verhoeven, D., "Limited-Data Computed Tomography Algorithms for the Physical Sciences," *Applied Optics*, Vol. 32, No. 20, 1993, pp. 3736-3754.

Chapter 3

High Speed Absorption Tomography with Advanced Reconstruction Algorithms

Jennifer L. Edwards¹ and Frederick C. Gouldin²

Cornell University, Ithaca, NY 14853

Mark A. MacDonald³

Intel Corporation, Beaverton, OR 97006

ABSTRACT

The results of research to develop and apply multiple line-of-sight (LOS) infrared absorption tomography for the study of combustion and as a sensor for monitoring and control of combustion systems are reported. Absorption tomography can provide data on the state of macro-mixing in combustion systems that can influence system performance, e.g. efficiency, radiation signature, and pollutant emissions. With infrared absorption tomography, spatial distributions of a radiation absorbing species

¹ Graduate Student, Sibley School of Mechanical and Aerospace Engineering.

² Professor, Sibley School of Mechanical and Aerospace Engineering.

³ Intel Corporation, Mobile Platforms Group.

can be reconstructed from the measured attenuation of radiation along multiple LOSs distributed over a measurement plane. In this paper, we report on the development of an IR laser absorption facility for rapid scanning tomography and on the performance of the tomographic reconstruction technique, Adaptive Finite Domain Direct Inversion.

3.1 Introduction

Our overall goal is to develop and apply multiple line-of-sight (LOS) infrared (IR) absorption tomography to study mixing and for problems of feedback combustion control, especially in propulsion systems such as ramjets and turbojets. For IR absorption tomography, the attenuation of radiation along multiple LOSs in a common plane is measured, and the data are used to reconstruct the spatial distribution in the measurement plane of the radiation-absorbing chemical species, e.g., CO₂, CO or NO. Many aspects of aircraft propulsion system performance such as efficiency, radiation signature and pollutant emissions depend in whole or part on mixing processes. In turn these processes depend on the flow configuration, flow turbulence and large-scale flow structures, i.e. macro-mixing, and on molecular transport, i.e. micro-mixing. Line-of-sight absorption and emission tomography provides data primarily on the state of macro-mixing.

For practical reasons the number of LOS measurements is finite, and thus the tomographic reconstruction problem is ill-posed [1,2]. We have developed a reconstruction method for cases where optical access is restricted, and the number of measurement LOSs is limited. This method, Adaptive Finite Domain Direct Inversion (AFDDI), typically requires 100 or more LOSs in a plane [3,4,5] which is an improvement over other reconstruction methods that may require up to 1000 or more LOS measurements for acceptable results [6].

Here we report on CO₂ concentration measurements performed on a square, forced jet using a flow facility constructed for the study and an IR laser absorption facility designed for making temporally resolved LOS absorption measurements of high quality. The absorption facility incorporates a tunable, color center laser system [7,8,9] and six scanning modules [10], allowing for simultaneous measurements to be made along multiple LOSs on a millisecond time scale. High time resolution and phase sensitive detection make the IR absorption facility a valuable instrument for the collection of data in both steady and unsteady flows. As a demonstration of the IR absorption facility capabilities, absorption data have been collected on a forced, square CO₂-air jet and tomographic reconstructions of the CO₂ concentration field have been performed using AFDDI. Additional evaluation of the AFDDI reconstruction method is performed using phantom tomographic measurement data. Together, the tomographic IR absorption facility and AFDDI reconstruction method provide a powerful tool for the analysis of combustion systems and flows.

3.2 Absorption Tomography

In absorption tomography, laser beam transmission measurements are made along many LOSs distributed over several viewing angles, $\{\theta_i\}$. In the present case, LOSs sharing a common viewing angle are parallel to each other and defined by their offset from the origin s , and view angle θ , Figure 3.1. Attenuation of line-of-sight measurements is governed by the Bouguer-Lambert-Beer law [11]

$$\ln\left(\frac{I_v^t}{I_v^0}\right) = -\int_{-\infty}^{\infty} n\sigma_v dt, \quad (3.1)$$

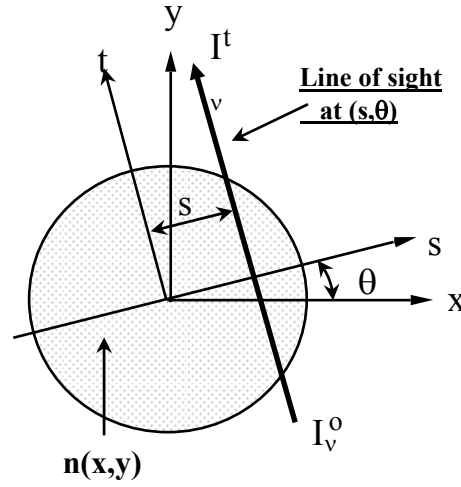


Figure 3.1. Schematic of coordinate system and LOSs in a single view. LOSs are defined by the offset s , and viewing angle, θ . It is assumed that $n(x,y)$ is zero outside of the measurement domain.

where I_ν is the radiant intensity of the laser beam at frequency ν , n is the number density of the optically active species, t is the path length, and σ_ν is the absorption cross section of the active species at the laser source, line frequency, ν . For isothermal conditions the absorption cross section can be assumed to be constant and line integrals of the species number density, $n(x,y)$, over a LOS set can be related to the laser beam transmission through the equation

$$\begin{aligned}
 p(s, \theta) &= -\ln \left[\frac{I_\nu^t}{I_\nu^0} \right] \\
 &= \sigma_\nu \int_{-\infty}^{\infty} n(s \cos \theta - t \sin \theta, s \sin \theta + t \cos \theta) dt \\
 &= \sigma_\nu R(n).
 \end{aligned} \tag{3.2}$$

For Equation (3.2) to be valid, the laser line width is assumed to be much smaller than the absorption line width.

The projection $p(s, \theta)$ is proportional to the line integral of $n(x, y)$ along the LOS defined by s and θ times the absorption cross section, σ_ν , of the optically active species. $p(s, \theta)$ can be related to the experimentally measured initial (I_ν^0) and transmitted (I_ν^l) laser beam intensities using the Bouguer-Lambert-Beer law as shown. $R(n)$ denotes the Radon transform [12,13] of distribution $n(x, y)$. The absorption cross section σ_ν is assumed to be constant under isothermal conditions in (1), but under non-isothermal conditions it may be necessary to include σ_ν within the integral due to changes in absorption line widths with temperature.

3.3 IR Absorption Facility

An IR absorption facility for making LOS measurements on confined and unconfined, nonreacting and reacting flows has been designed and constructed [10]. The facility consists of a Nd:YVO₄-pumped, broadly tunable, KCl:Li color center laser (CCL) system [7,8,9] and an optical apparatus composed of six scanning modules that permit simultaneous measurement of LOS absorption in a single plane at six different viewing angles, $\{\theta_j\}$. A schematic of the facility is shown in Figure 3.2. The color center laser consists of a KCl:Li color center crystal housed in a vacuum dewar between a dichroic input coupler and Littrow-configuration grating for wavelength selection and tuning. The color center laser beam is tunable over the range 2.45-2.82 μm spanning absorption lines of several important combustion products including H₂O, NO, and CO₂ [8]. For the measurements reported here, absorption in the 2.7 μm CO₂ absorption band is measured. The CCL beam is split into six nearly equal-intensity beams, each sent into a separate module, illustrated in Figure 3.3. In addition, a fraction of the beam is sent to a reference detector for monitoring the laser output power. The six modules are located at equally spaced

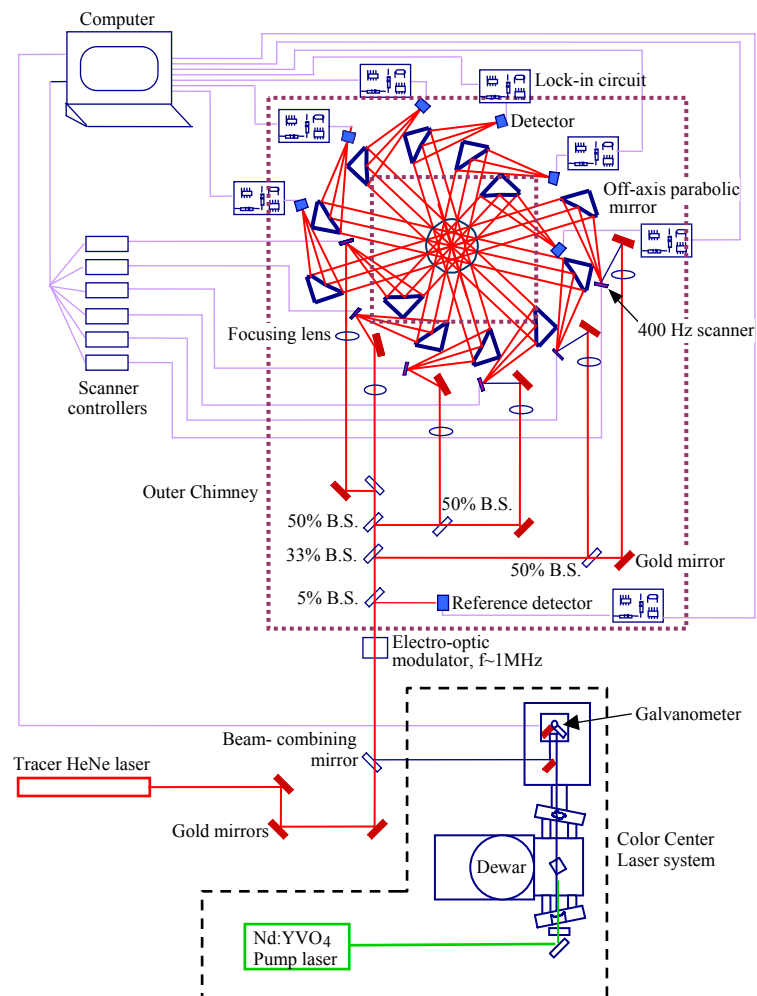


Figure 3.2. Schematic diagram of the IR absorption facility. The absorption facility consists of an IR laser beam divided amongst 6 scanning modules and a reference detector. The IR beam originates at the CCL (dashed lines) and is coupled to a tracer HeNe laser for alignment. The HeNe-coupled IR laser path throughout the facility is highlighted in red. Beam splitters for dividing the laser into the 6 modules are indicated by B.S. Each module consists of a focusing lens, a mirror mounted on a 400 Hz scanning galvanometer, a pair of parabolic mirrors, and an InAs detector. Approximate locations of inner and outer chimneys enclosing the optics are indicated by dotted lines though it is important to note that the drawing is not to scale. Further details on the module setup are presented in Figure 3.3. Drawing courtesy of Dr. Ann Chojnacki.

viewing angles spanning 150° in 30° increments. The CCL beam in each module is focused onto an optical scanning mirror that is mounted on a galvanometer and located at the focus of an off-axis parabolic mirror. The galvanometer-driven scanning mirror sweeps the beam horizontally across the parabolic mirror, producing a set of parallel LOS laser paths spanning the measurement domain. The CCL beam is collected by a second off-axis parabolic mirror and focused onto a thermoelectrically cooled InAs photodetector. The beam is swept across the flow domain at a rate of approximately 400 Hz. The galvanometer is driven by a modified saw tooth wave form with the signal rising in magnitude for 70% of the period and falling for 30%. The galvanometer scanning speed is constant over the majority of the driving signal rise allowing the time history of the galvanometer scanner signal to be correlated to the location of an instantaneous measurement (i.e. the position of the beam). The full range across which the laser beam is swept by the galvanometer is -15 mm to 15 mm, though only measurements within the region of interest from -10 mm to 10 mm are

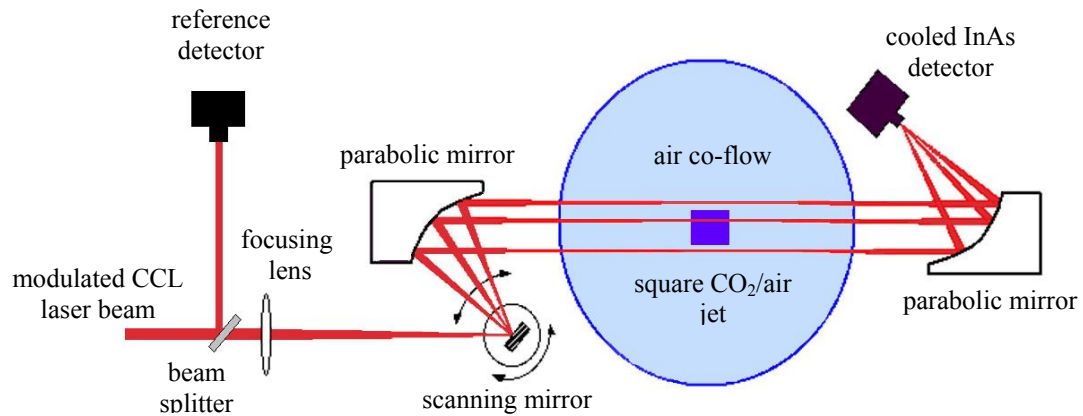


Figure 3.3. Schematic diagram of a single module and reference detector. Each module consists of a focusing lens, a mirror mounted on a 400 Hz scanning galvanometer, a pair of parabolic mirrors, and an InAs detector. The scanning mirror sweeps the CCL beam across the parabolic mirror creating parallel lines-of-sight across the measurement region. A second parabolic mirror focuses these lines-of-sight onto an InAs detector.

used for the tomographic analysis. From the time history of the sweep, transmission of the beam along 175 selected LOSs in the flow is determined. It takes approximately 1.5 milliseconds to complete a sweep of the laser beam across the region of interest in the measurement domain allowing for measurements of high temporal resolution.

Phase sensitive detection is used to improve the signal to noise ratio. Before splitting, the CCL beam is electro-optically modulated at a frequency of approximately 1 MHz for phase sensitive detection. Each photodetector is connected to a demodulating, 'lock-in' circuit which beats the 1 MHz transmitted beam with a coherent reference signal at 1 MHz to generate a signal that represents the transmitted laser intensity as a function of time. The demodulated detector output is low-pass filtered at 40 kHz, before being read and processed by a fast PC-based data acquisition system. Data are acquired at 800,000 samples/sec, while analog to digital conversion is performed with two 12 bit National Instruments PCI-6110E boards. Approximately 1200 samples are collected by each module from the time continuous signal as the laser beam is swept across the region of interest from -10 mm to 10 mm in the measurement domain. Each sample corresponds to a specific location of the laser beam as mentioned previously. A Gaussian filter with a standard deviation of 0.02 mm is used in data processing to average the 1200 samples into 175 data points [14]. These 175 data points yield the tomographic projection measurements at 175 lines-of-sight per view angle with center-to-center spacing of 0.1143 mm.

While the absorption facility developed for this work utilizes a KCl:Li color center laser (CCL) system and InAs detectors, it is important to note that this setup can be adapted for use with other laser systems and detectors. This would allow for phase sensitive detection and high time resolution measurements of additional species in other wavelength ranges for combustion or non-combustion applications.

3.4 Flow Apparatus

Measurements were made on a forced, square jet (8 mm x 8 mm) with a flow of a mixture of air and CO₂. The flow apparatus is shown schematically in Figure 3.4. Gas flows are supplied from high pressure tanks and controlled by electronic mass flow controllers; maximum flow velocities up to 50 m/s are possible. A speaker that is driven by an audio power amplifier provides jet forcing at 30 Hz. A brass honeycomb with a cell diameter of approximately 0.8 mm is located 1 cm upstream of the jet exit to provide a nearly uniform exit velocity profile without forcing. A chimney, exhaust hood, and 5 inch diameter co-flow of air are added to reduce the effects of ambient flow perturbations on the jet. Hot-wire anemometry measurements were made to characterize the velocity distributions of the unforced flow at 0.1 and 1 cm downstream from jet exit. These distributions show a low speed (1 m/s) co-flow surrounding the square jet with large velocity gradients at the edge of the square jet. At 0.1 cm downstream from the jet exit, multiple peaks are seen in the jet velocity distribution that are due to the individual honeycomb cells. At 1 cm (1 *De*)

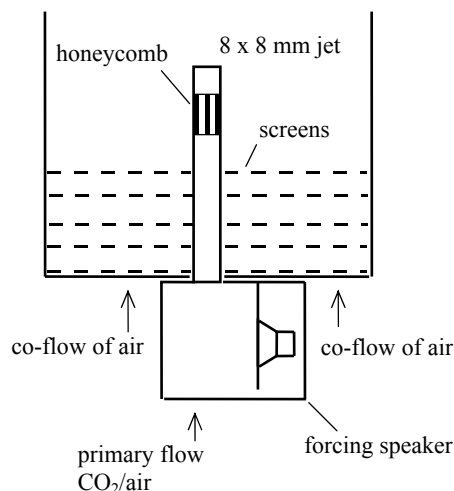


Figure 3.4. Schematic diagram of square jet flow apparatus. A CO₂/air mixture is fed through a speaker chamber that forces the flow at 30 Hz through an 8 x 8 mm square jet. The jet is surrounded by a low velocity circular co-flow of air.

downstream, these peaks have merged, and the velocity distribution is nearly flat across the center of the jet. The equivalent diameter, De , is defined as the diameter of a round jet having the same cross-sectional area as the square jet.

3.5 Performance of Absorption Apparatus

A custom built alignment tool was used to align and determine the laser beam position and orientation for each of the six viewing angles. The tool consists of an aluminum ring containing six sets of alignment holes. Each set consists of 16 pairs of holes, with each member of the pair located on opposite sides of the ring. The pairs in each set are equally spaced and lines connecting the hole pairs of a set form parallel chords of a circle in a single, horizontal plane. These chords define the known locations of particular lines of sight and provide the spatial alignment and calibration for the optical system.

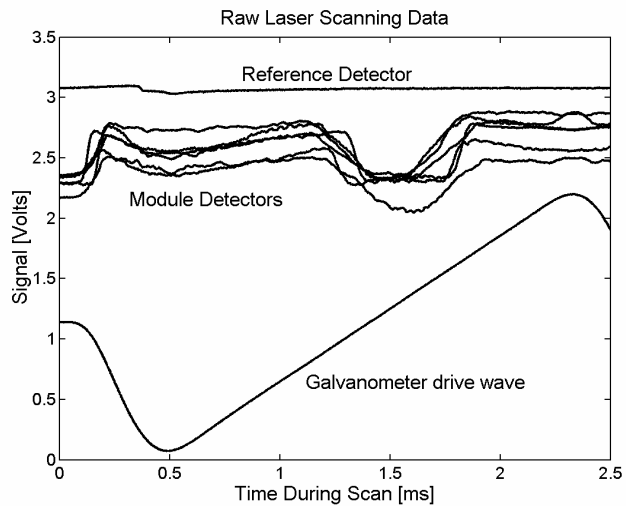
The six modules complete simultaneous scans over the measurement plane in approximately 1.5 ms. The outputs from the lock-in amplifier circuits for each module are over-sampled by the data acquisition system to further reduce the influence of electrical noise. Two thousand data points are collected from each module during a scan. However only those portions of the detector signals collected while the galvanometer signal increases are used for reconstruction of CO₂ distributions. A digital, low-pass filter with a cutoff frequency of 20 kHz is applied to the acquired data to further reduce the influence of residual electrical noise. Signal-to-noise ratios, SNR , vary due to changes in the flow conditions (e.g. amount of CO₂, forcing phase, and flow rate) and due to changes in color center laser power. $SNRs$ ranging from 9 to 68 were measured under various flow conditions using the IR absorption facility.

Measurements were made in both laminar and forced jets with velocities ranging from 1 to 50 m/s and with CO₂ concentrations in air ranging from 8.4% CO₂

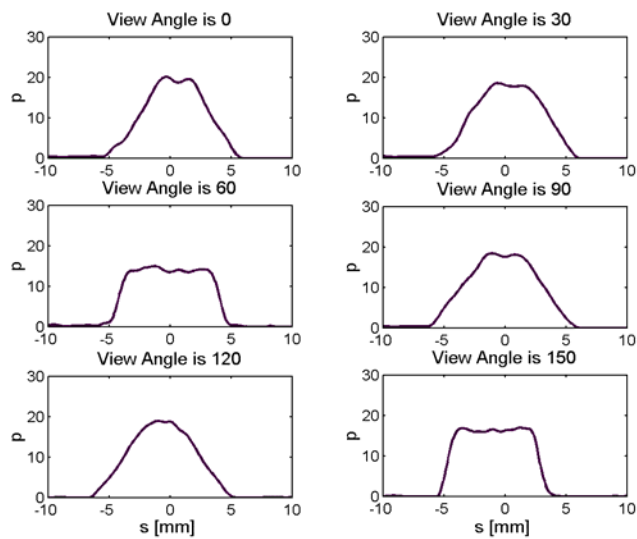
to 100 % CO₂. Figure 3.5 shows a representative sample set of the raw signals from the absorption facility and the resulting projection data obtained from the six modules for measurements made within 1 mm downstream of the exit of a 6 m/s jet with a 50% CO₂ concentration. For each set of projection data, the location of the centerline and shape of the CO₂ absorption profile is slightly different in each of the views because the jet is not centered in the measurement domain and is not axisymmetric. Residual signal noise after low-pass filtering and fluctuations of ambient laboratory CO₂ concentrations are the most significant sources of error in the projection measurements. Fluctuations of laboratory CO₂ concentrations can be a significant source of error, and care has been taken to reduce the influence of these fluctuations. Dry nitrogen is used to purge the color center laser housing and reduce absorption from ambient CO₂. In addition, the experimental apparatus is shielded using an inner chimney surrounding the flow facility and an outer chimney surrounding the tomographic apparatus to reduce interference from absorption by CO₂ in the surrounding room (see Figure 3.2). An air co-flow and exhaust hood provide further barriers to CO₂ concentration fluctuations near the measurement region. All measurements are made with these precautions in place. The efficacy of these precautions is evident in projection data such as those shown in Figure 3.5 that absorption goes to zero outside the jet flow region.

3.6 Tomographic Reconstruction

The practical reconstruction problem is the inverse problem [15] of solving Eq. (3.2) for $n(x,y)$ in cases where $p(s, \theta)$ is known at a discrete set of s and θ . While the continuous problem for which $p(s, \theta)$ is known for all s and θ is well-posed, the discrete reconstruction problem is not. Consequently, the reconstruction solution method must



(a)



(b)

Figure 3.5. Absorption measurements from a 6 m/s forced jet with 50% CO₂ made at the jet exit. (a) Raw laser scanning data recorded from the reference and module detectors with the galvanometer drive signal. (b) Projections obtained from the raw data in (a).

be matched to the particular problem of interest, as defined by the character of $n(x,y)$ and by the number and distribution of the available projections $\{p(s_i, \theta_j)\}$ over s and θ . Here we use Adaptive Finite Domain Direct Inversion (AFDDI) for reconstruction, a method developed at Cornell [3,4] especially for cases where optical access is restricted and a limited set of LOS measurements is available. AFDDI is intended for use where the goal is to determine the large-scale features in a distribution. It is suitable for cases where parallel projection measurements are available over a limited number of viewing angles, θ_i . For successful tomographic reconstruction using AFDDI, the number of viewing angles available is more important than the number of projections per viewing angle.

Finite Domain Direct Inversion (FDDI), a precursor to Adaptive FDDI, was developed by Ravichandran and Gouldin [3]. Separate basis functions derived from the Kaiser window function, $W(R)$, [16] are used to express both the measured projections, $p(s, \theta)$, and the distribution to be reconstructed, $n(x,y)$. Use of the Kaiser window function results in a set of local 2-D basis functions, $\{b_k(x-x_k, y-y_k)\}$, used in the representation of $n(x,y)$, that are band limited while finite computer precision renders their numerical representation space limited. These basis functions are located on a set of triangularly distributed anchor points, $\{x_k, y_k\}$, and their aspect ratio is defined by two parameters: the cutoff frequency, C_0 , and the influence length parameter, H_0 . These parameters are chosen according to guidelines provided by Ravichandran and Gouldin in which the product $C_0 H_0$ is set to 1.6 and C_0 is set to $1/2\Delta g$, where Δg is the closest spacing between the basis functions on the triangular grid [3]. The 1-D basis functions, $\psi(s)$, used in the expansion of $p(s, \theta)$ are the 1-D inverse Fourier transforms of the Kaiser window function, $W(R)$ [3,4].

$$\psi(s) = \mathcal{F}^{-1}(W(R)) = \mathcal{R}(b_k(x - x_k, y - y_k)), \quad (3.3)$$

where \mathcal{F}^{-1} denotes the 1-D inverse Fourier transform and \mathcal{R} the Radon transform. The Kaiser window function itself is defined as

$$W(R) = \begin{cases} \frac{I_0\{2\pi H_0(C_0^2 - R^2)^{0.5}\}}{I_0\{2\pi H_0 C_0\}} & \text{if } |R| < C_0 \\ 0 & \text{otherwise,} \end{cases} \quad (3.4)$$

where I_0 is the modified Bessel function of the first kind, order 0, and R is the Fourier space variable.

As noted, the distribution $n(x,y)$ is expanded in a set of local 2-D basis functions that are located on an equilateral triangular grid defined by the anchor points $\{x_k, y_k\}$:

$$n(x, y) = \sum_{k=1}^K f_k b_k(x - x_k, y - y_k). \quad (3.5)$$

For the original implementation of FDDI, the points on the triangular grid are uniformly spaced with the closest spacing, Δg , set to 0.1925 on a normalized grid extending from -1 to 1 in the x and y directions. In Adaptive FDDI, the triangular grid is adapted to include additional basis functions in a triangular configuration with Δg of the additional basis functions set to 0.1111 on the normalized grid. Sample FDDI and AFDDI basis functions are shown in Figure 3.6. For the uniform triangular FDDI grid, characteristic view angles of 0, 30, 60, 90, 120, and 150 degrees allow for the lines-of-sight to pass through the maximum number of basis function locations possible (see Figure 3.6). In Adaptive FDDI, there is no simple choice of characteristic view angles due to the non-uniform addition of basis functions to the adapted triangular grid. However, studies by Ha et al [4] have concluded that there is no need to restrict the view angle and line-of-sight selection to the characteristic sets

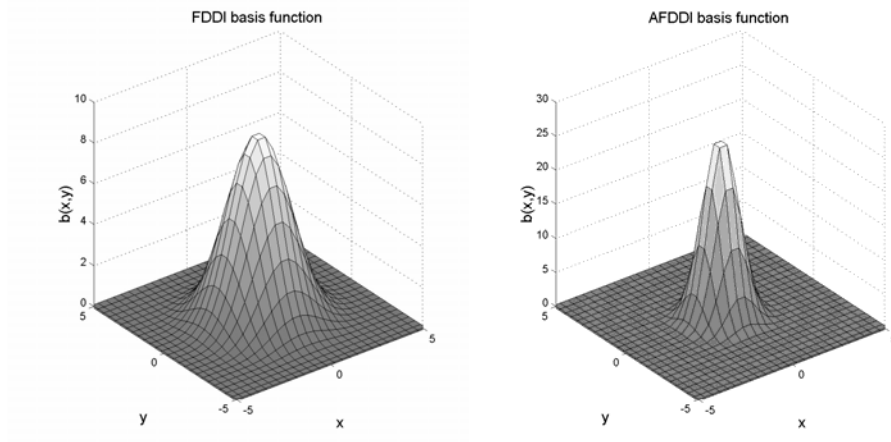


Figure 3.6. Two-dimensional basis functions of varying aspect ratios used in the FDDI and AFDDI reconstructions. These basis functions are band limited and numerically space limited.

determined by the grid geometry. For the results reported here, measurements are made at 175 uniformly spaced lines-of-sight per view angle and 6 view angles spaced every 30 degrees.

For the expansion given in Eq. (3.5), $\{f_k\}$ is the set of unknown weighting coefficients for the basis functions, b_k , where K denotes the number of basis functions used in the expansion. The reconstruction problem is reduced to finding $\{f_k\}$ given the set of projection measurements $\{p(s_i, \theta_j)\}$ and the set of basis functions $\{b_k\}$. $\{f_k\}$ is determined by solving the resulting overdetermined least squares problem

$$Cf = p \tag{3.6}$$

for the vector of weighting coefficients, f , by singular value decomposition [17]. In Equation (3.6), C is a $M_N \times K$ projection matrix, the elements of which represent the contribution of each 2-D basis functions to the projection measurement lines-of-sight. For each projection measurement, the contribution of each basis function can be calculated by evaluating the 1-D basis function at the shortest distance from the

projection measurement location (s_m, θ_n) to the basis function grid location (x_k, y_k) , with the shortest distance defined as

$$s_m - x_k \cos \theta_n - y_k \sin \theta_n \quad (3.7)$$

such that

$$C_{m_n, k} = \psi(s_m - x_k \cos \theta_n - y_k \sin \theta_n). \quad (3.8)$$

The index m_n denotes a specific projection measurement specified by offset (s_m) and view angle (θ_n) and index k refers to a particular basis function. The projection matrix C is modified to impose a bound that forces $n(x, y)$ to zero outside of the measurement domain and to remove contributions from portions of the basis functions that lie outside of the measurement domain [3,18]. Using the modified projection matrix, a new matrix equation is formed:

$$Df = p \quad (3.9)$$

where D is the modified projection matrix that includes boundedness in the domain. f is a K vector and p is the M_N projection vector. M_N is the total number of projection measurements, i.e. the number of views, N , times the number of projections per view, M . It is necessary for $M_N > K$ for the problem stated in Equations (3.6) and (3.9) to be overdetermined. Equation (3.9) is formulated as a nonnegative least squares problem as described in Ravichandran et al. [3] and solved using singular value decomposition.

In the original FDDI, 97 basis functions located on a uniform triangular grid were used in the expansion in Equation (3.5). The vector of weighting factors, f , is solved for using singular value decomposition and the weighting factors are then applied to the series expansion of $n(x, y)$ in Equation (3.5). For Adaptive FDDI, additional basis functions are added to the expansion at grid points located in regions

of high spatial gradients of $n(x,y)$. These high gradient regions are identified in the reconstruction obtained by application of the original FDDI solution method to the projection data [4,5,18]. Gradients of the reconstructed distribution obtained using the original FDDI method are evaluated at possible basis function locations on the additional adaptive grid. The basis function locations are ranked from highest to lowest gradient and a specified number of basis functions in the highest gradient regions are selected for use in Adaptive FDDI (see Figure 3.7 for a sample adaptive grid). The projection matrix D is modified in AFDDI to include the contributions from the additional basis functions, the weighting coefficients $\{f_k\}$ are recalculated, and the reconstruction of $n(x,y)$ is obtained. The number of basis functions added during AFDDI is variable, with 50 commonly used for a total of 147 basis functions. It is thus necessary to use greater than 147 projection measurements to make the problem stated in Equations (3.6) and (3.9) overdetermined. AFDDI reconstructions have been performed on data collected from LOS configurations utilizing up to 1050

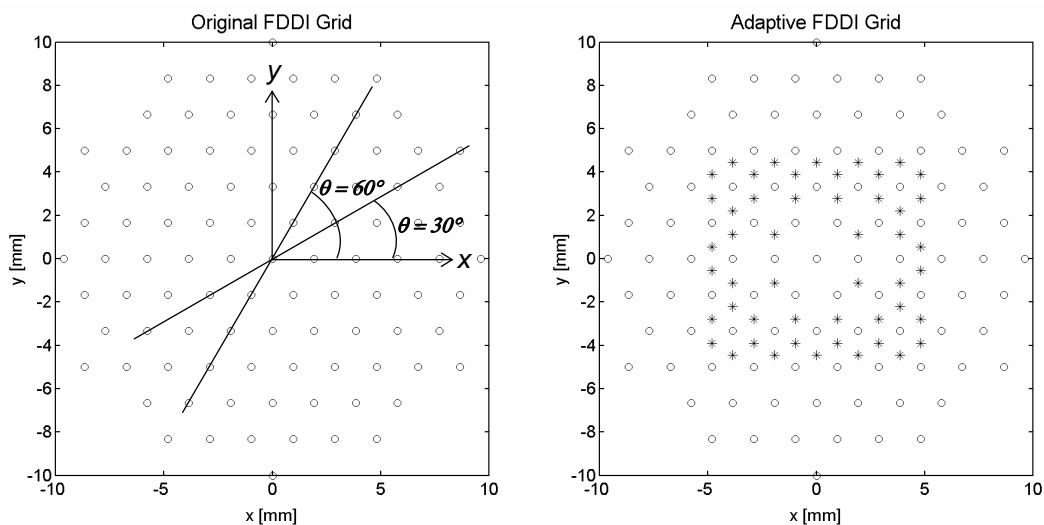


Figure 3.7. Adaptive grid for a square phantom distribution. Left: uniform grid of 97 basis functions used in FDDI. Characteristic view angles of multiples of 30° are shown on the FDDI grid. Right: Adaptive grid with the original 97 basis functions (o) and 50 additional basis functions (*) added in regions of high gradients.

projection measurements though the number of projection measurements can be increased, if necessary, depending on the diameter of the laser beam, the size of the measurement domain, and the resolution needed to capture small scale flow features.

3.7 Forced Square Jet Reconstructions from Laboratory Data

Inversion of the projection data collected by the 6-module IR absorption facility was performed using the AFDDI method. 175 LOSs for each view angle (1050 total) were used to reconstruct CO₂ concentration fields from the forced jet facility. Various two-dimensional filters were investigated for smoothing of the raw reconstructions, including averaging, disk (pillbox), and Gaussian filters of varying kernel size and FWHM [14]. A Gaussian filter with a full-width at half maximum equal to twice the closest spacing on the adaptive triangular grid was chosen for application as it smoothed the reconstruction noticeably while retaining the high contrast features of the reconstruction. For each point on the reconstruction grid, the averaging and disk filters would provide a uniformly weighted average of a specified number of grid points surrounding the central point. The disk filter would average the points from a circular area surrounding the central point and the averaging filter would average the points from a square area surrounding the central point. Because a Gaussian filter provides an average weighted more towards the value of the central point, it provides gentler smoothing and preserves high gradients better than similarly sized standard averaging and disk filters. Varying the Gaussian filter size and standard deviation controls the degree of smoothing performed. The Gaussian filter kernel, h , can be determined using the formulae below, where x and y are the locations

of each grid point, σ is the standard deviation, and h_g is an intermediate step needed for forming the kernel h .

$$h_g(x, y) = e^{-(x^2+y^2)/(2\sigma^2)}$$

$$h(x, y) = \frac{h_g(x, y)}{\sum_x \sum_y h_g} \quad (3.10)$$

The filter used for this application was chosen to reduce the structure seen from individual AFDDI basis functions in the reconstruction. The Gaussian FWHM was set at the twice the closest basis function spacing to sufficiently smooth or “blend” the contributions from neighboring basis functions to the reconstruction. The Gaussian filter does a good job of removing the artifacts from the raw reconstructions while retaining the large-scale structures and high gradients in the concentration field. Peak reconstructed concentrations and jet extent, as measured by the full-width at half-max (FWHM) location of the reconstructed jet distribution, are not altered noticeably by filtering.

Figure 3.8 shows the filtered AFDDI reconstruction obtained from the projection data collected at 0.1 cm downstream of the jet exit, see Figure 3.5. These results show that the effect of forcing in the 6 m/s jet is modest. Reconstructions of the CO₂ concentration field at the jet exit are similar for the eight forcing phases studied. Results at 1 De downstream show slight spreading of the jet and small changes in the shape of the jet cross section and in peak concentration values (see Figure 3.9).

Figure 3.9 shows contour plots of four forced-jet reconstructions from data collected at 1 De downstream from the jet exit on a 6 m/s jet with 50% CO₂ and a 3 m/s jet with 25% CO₂. The results in Figure 3.9 are from four scans taken at 90° phase increments relative to the jet forcing signal. Changes in jet size and peak

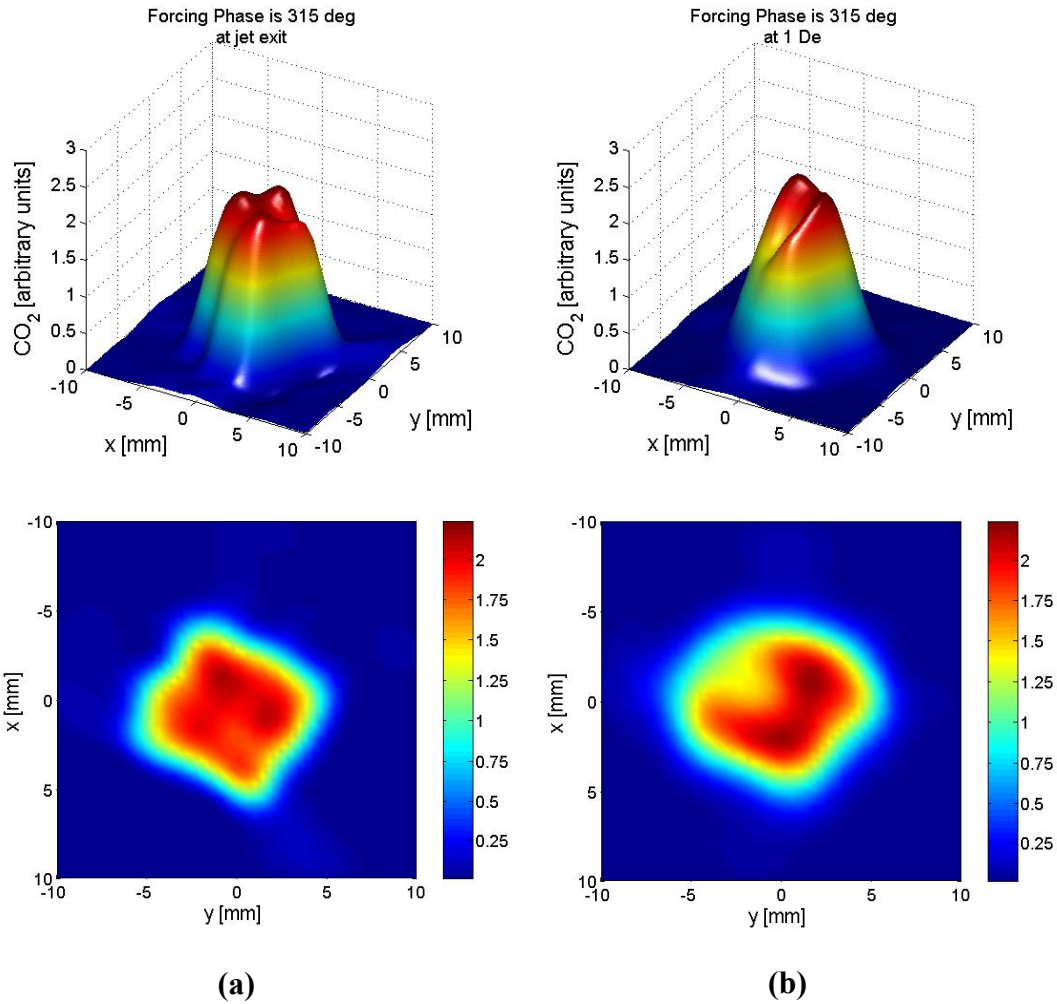


Figure 3.8. Filtered forced jet AFDDI reconstructions of a 6 m/s jet with 50% CO₂.

- (a) Reconstruction of projection data in Figure 3.5, measurements made at the jet exit.
- (b) Reconstruction of measurements made 1 De downstream of the jet exit.

While it is possible to do so, we have not explicitly calculated the absorption cross section, σ_{ν} , and thus present the CO₂ field in arbitrary units.

concentration are quantified in Table 3.1. The area of the jet cross section is estimated based on the number of grid points in the reconstruction with CO₂ concentrations above a threshold value equal to 1/5 of the maximum CO₂ concentration. Jet area and peak concentrations shown in Table 3.1 are measured relative to the maximum values

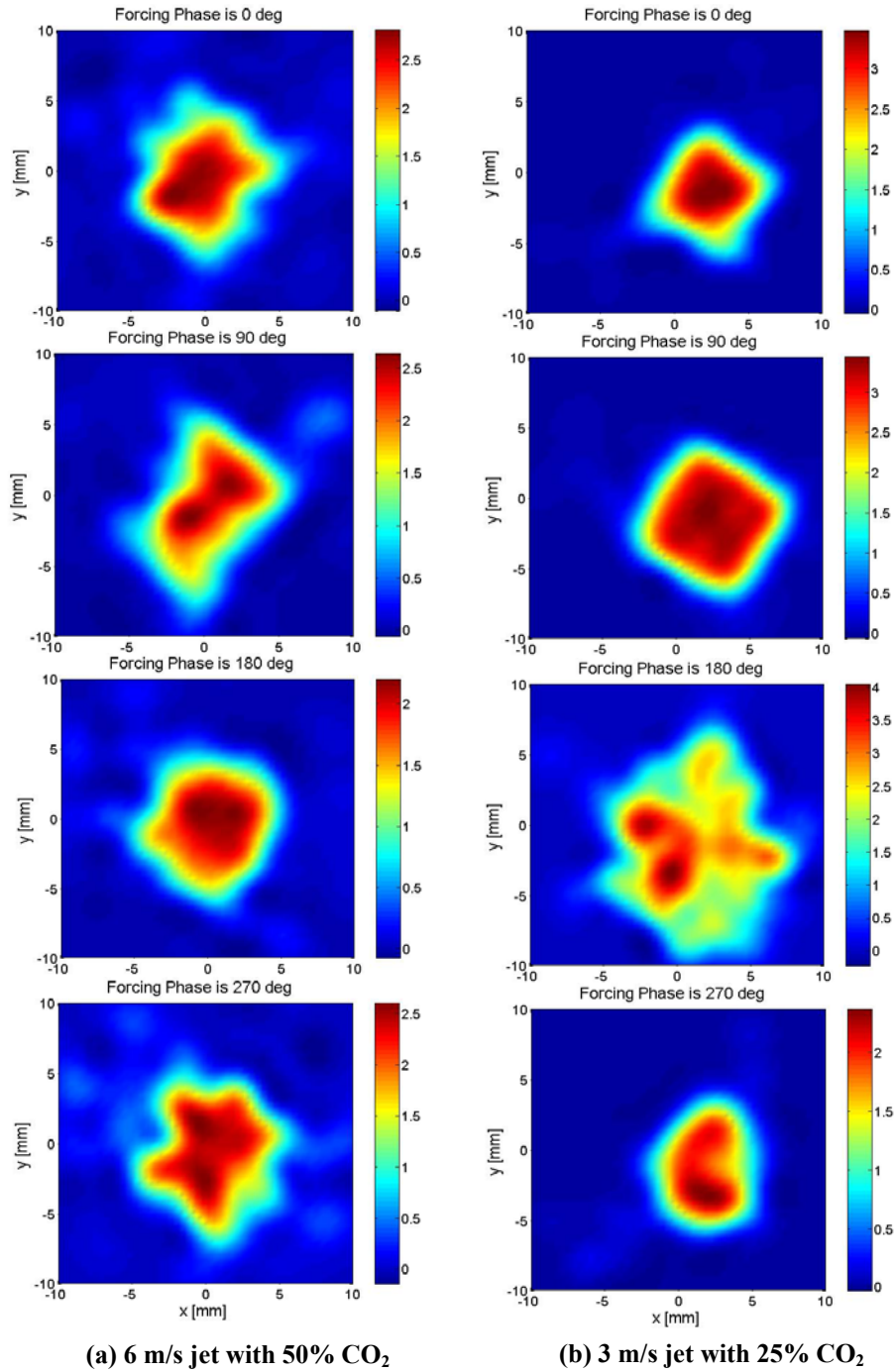


Figure 3.9. Reconstructions at 0, 90, 180 and 270 degrees in the forcing phase. Maximum CO₂ values are labeled on the plots in arbitrary units.
(a) 6 m/s jet with 50% CO₂ at 1 De downstream of the jet exit.
(b) 3 m/s with 25 % CO₂ jet at 1 De downstream of the jet exit.

determined over eight phases (45° increments) in the forcing period. Results show that modulation of the 6 m/s jet is perceptible with some changes to the shape of the jet cross section but changes in size and peak concentration are limited to approximately 20% or less of maximum size and concentration values. Significant modulation of the jet flow is apparent in the reconstructed distributions of the 3 m/s jet at 1 *De* with peak concentration values varying up to 50% of the maximum concentration over all phases of the forcing period (see Table 3.1). The size of the 3 m/s jet varies from 36% to 100% of its maximum size (up to 64% change) over the eight forcing phases studied. Compared to the 6 m/s jet, the 3 m/s jet shows significant effects due to the forcing. While the forcing amplitude and frequency were the same for the two cases, the dynamic pressure of the 6 m/s jet is a factor of four larger than that of the 3 m/s jet, which accounts for the differences in forcing effect of the two jets.

The square jets measured using the IR absorption facility provide an excellent opportunity to test the capabilities of the AFDDI reconstruction method for high

Table 3.1. Comparison of forcing effects on two forced CO₂/air jets.

<i>Forcing</i>	<i>6 m/s jet, 50 % CO₂</i>		<i>3 m/s jet, 25 % CO₂</i>	
	<i>% Max Area</i>	<i>% Max CO₂</i>	<i>% Max Area</i>	<i>% Max CO₂</i>
0	82	100	40	86
45	80	97	53	84
90	87	94	61	85
135	100	87	66	76
180	80	78	100	100
225	83	86	47	51
270	90	93	42	58
315	90	77	36	70

contrast cases in the presence of noise. Various aspects of the distribution characteristics and measurement geometry must be considered for tomographic applications. Distribution orientation, size, location, and shape can affect the choice of method for reconstruction as well as the LOS measurement configuration. Note that the reconstructions in Figures 3.8 and 3.9 show that the square jet is not aligned with the grid axes and is shifted slightly away from the center of the measurement region. The alignment and location of the jet within the measurement domain are not critical to the experimental setup because the AFDDI reconstruction method is able to capture the orientation and location of the jet in various positions. The reconstructed distributions in Figures 3.8 and 3.9 are verified to be consistent with the position of the jet in the flow facility. Forcing has been shown to affect the size and shape of the jet. Changes in distribution size and shape will affect the selection of additional basis functions in the AFDDI reconstruction method. Characterizing the performance of AFDDI under varying conditions of distribution geometry (size, shape, orientation), distribution features of low and high contrast, and the presence of measurement noise is important to the evaluation of the robustness of the reconstruction method.

3.8 Performance of Adaptive FDDI

The experimental work reported in this paper is focused on square jet flows with top-hat like concentration profiles having steep, smooth sides and relatively flat tops. These features are difficult to accurately reconstruct with a generic basis set suitable for application to a wide range of problems, and their high-contrast presents a significant challenge for many reconstruction methods. While reconstruction methods such as Fourier-based [6,19] backprojection or series-expansion based [6,20,21] algebraic reconstruction techniques are often used to reconstruct high-contrast features, a large number of line-of-sight measurements distributed over many

view angles is required in these cases for accurate reconstructions. Compared to many other reconstruction methods, AFDDI requires a low number of LOS measurements for accurate reconstructions. The number of the projections needed to make the reconstruction problem in Equation (3.9) overdetermined is based on the number of basis functions used in the AFDDI reconstruction. This limits the minimum number of LOS measurements necessary for reconstruction to approximately 150 instead of 1000 or more that are necessary for other reconstruction methods. The shape of the basis functions used in Adaptive FDDI make it well suited to cases where smooth, high gradient profiles are expected. In the original FDDI, 97 identical basis functions located on a uniform triangular grid were used for tomographic reconstructions [3]. With AFDDI, 97 basis functions are used on the original grid and 50 basis functions are added in the regions having the highest concentration gradients. Sample grids are shown in Figure 3.7 for the distribution shown in Figure 3.10.

Analyses of the performance of AFDDI were conducted on the 27 different phantom distributions of various jet/peak configurations [1,18], including multiple

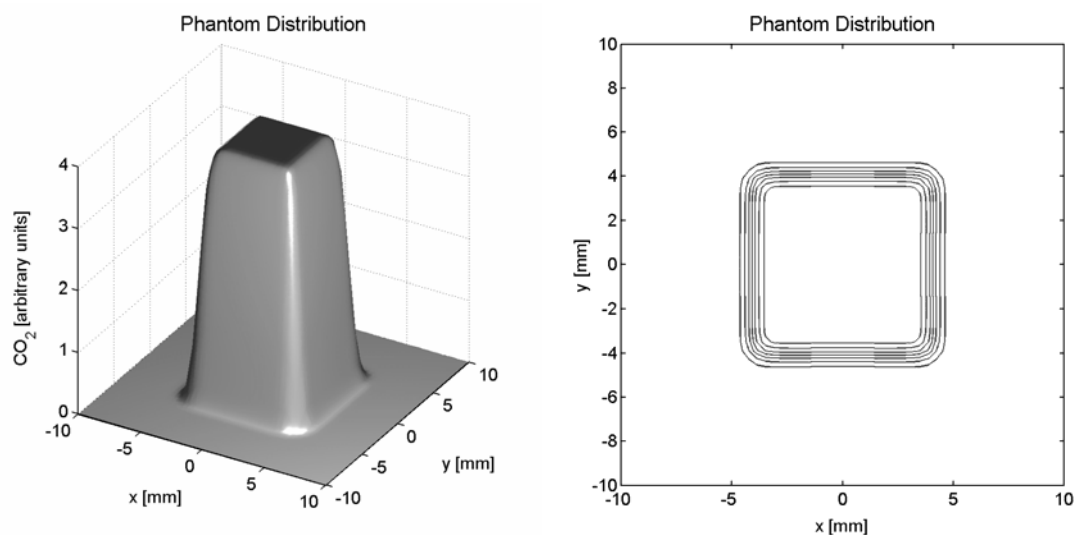


Figure 3.10. Sample phantom top-hat distribution used in evaluation of AFDDI performance (see Figure 3.7 for corresponding AFDDI grid). The square top-hat shape is similar to the experimental CO_2 concentration distributions measured using the IR absorption facility.

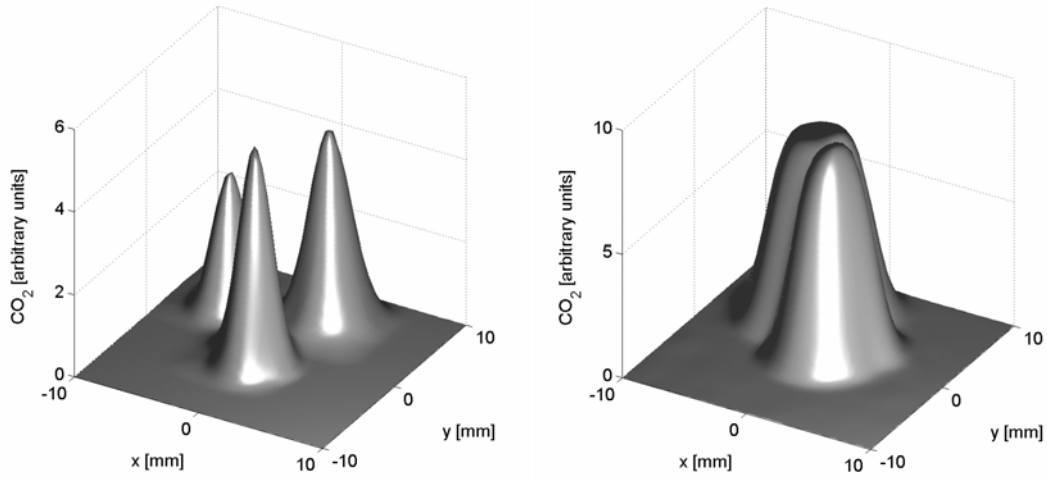


Figure 3.11. Sample multiple-jet (left) and merged-peak phantom distributions derived from previous measured data [1,17].

circular jets and merged peaks (see Figures 3.10 and 3.11), and one square top-hat distributions to test the behavior of AFDDI under high gradient situations. The phantom distributions derived from jet flows [1,18] are representative of the type of smooth high-gradient distributions encountered in physical flows, while the top-hat phantom distribution is of the shape expected from forced jets similar to the one reported above. Additional investigations of AFDDI performance using triangular and square top-hat data are discussed later in this section. Use of these phantom distributions allows for the evaluation of AFDDI using realistic concentration distribution data. The distributions are expressed as an array of CO_2 concentration values on a 50×50 square grid. Phantom projection data were calculated according to the isothermal Bouguer-Beer-Lambert law, Equation (3.2). Absorption cross sections are assumed to be constant as in Equation (3.2) and are not included in the phantom projection calculations. Thus, phantom distributions are presented in arbitrary units and are proportional to number density. Laser absorption data were simulated by numerical integration of each CO_2 number density distribution along each specified

line-of-sight, producing phantom projection measurements with no error. The 50x50 grid distributed over the -10 mm to 10 mm domain yields a grid cell size of 0.4 mm x 0.4 mm. Numerical integration of the phantom distribution along a line-of-sight yields an equivalent laser diameter of approximately 0.45 mm. For the purposes of evaluating AFDDI performance using phantom distributions, this method should be sufficient to provide the resolution necessary to capture the features in the distribution. However, if simulating laser absorption measurements of a well characterized distribution (e.g. previously characterized using CFD or probe sampling) for comparison to experimental measurements, it would be necessary to more accurately model the laser diameter by performing volume integrals over multiple grid points along a line-of-sight.

The standard LOS configuration used for these studies is composed of 175 parallel LOSs per view angle and 6 view angles spaced every 30 degrees, resulting in a total of 1050 LOSs. This measurement configuration was chosen to match the experimental setup of the IR absorption facility. It should be noted that while the studies below were performed using 1050 LOSs, there was no appreciable degradation in reconstruction performance as measured by the error measures discussed below, when testing randomly selected phantom distributions using 87 LOSs per view angle (522 total) and 51 LOSs per view (306 total). The AFDDI basis functions, phantom distributions, and tomographic reconstructions were discretized on a uniform 50x50 point grid. Grids ranging from 25x25 to 100x100 were investigated and it was determined that the 50x50 grid allowed for satisfactory resolution to capture the high gradient regions without needing excessive computational time.

Three error measures are often used for quantitative comparisons of reconstruction results [20,22] (Equation (3.11)): 1) the normalized root mean square error, also called the reconstruction error, e_{rms} ; 2) the normalized mean absolute error,

e_{abs} ; and 3) the maximum error, e_{max} . e_{rms} emphasizes a few large errors in the reconstruction, while e_{abs} emphasizes many small errors. These error measures are defined mathematically as

$$\begin{aligned}
 e_{rms} &= \frac{\|n_1 - n_0\|_F}{\|\overline{n_0 - n_0}\|_F} \\
 e_{abs} &= \frac{|n_1 - n_0|}{|n_0|} \\
 e_{max} &= \frac{\max(|n_0 - n_1|)}{n_0(x_{max}, y_{max})}
 \end{aligned} \tag{3.11}$$

where n_0 is a reference distribution, in this case, the phantom distribution, and n_1 is the reconstructed distribution to be evaluated. $\|\cdot\|_F$ denotes a Frobenius norm and the overbar denotes a spatial average. Reconstruction errors will result from both the inability of the basis set to exactly represent a distribution, the *representation error*, and from errors in the retrieval of the weighting coefficients, the *retrieval error*. The overall *reconstruction error* is composed of contributions from representation and retrieval errors. The best representation of a phantom distribution, $n_{best}(x,y)$, is given by

$$n_{best}(x, y) = \sum_{k=1}^K f_{best} b_k(x - x_k, y - y_k) \tag{3.12}$$

Best representation weighting factors, f_{best} , are computed using a least squares fit of the basis functions to the phantom distribution. The representation error, e_{rep} , is then calculated as the normalized root mean square error using the phantom as the reference distribution, n_0 .

$$e_{rep} = \frac{\|n_{best} - n_0\|_F}{\|\overline{n_0 - n_0}\|_F} \tag{3.13}$$

Results of AFDDI performed on phantom absorption data for a set of 27 distributions including round jets, merged-peaks, and a square top-hat showed that AFDDI failed to reduce the reconstruction error below the FDDI error in 10 cases (see Figure 3.12). Many of these ten distributions contain regions of high gradient as well

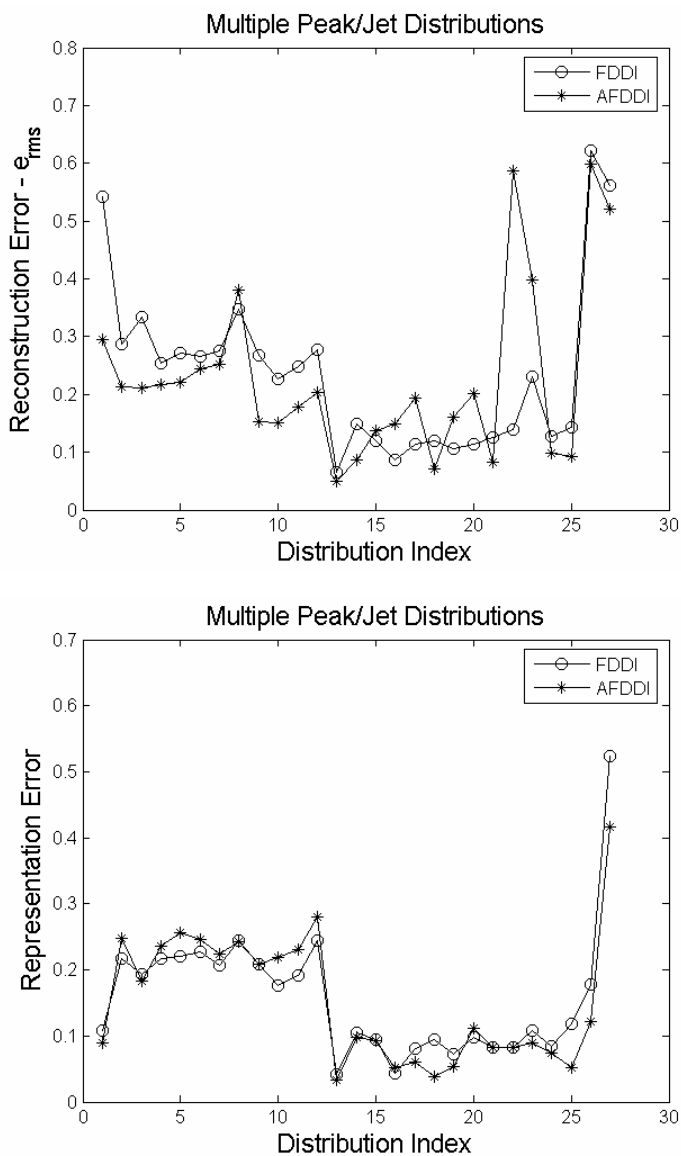


Figure 3.12. Reconstruction and representation errors for various jet and peak distributions.

as regions of low (nonzero) gradient, especially near the tops of the distributions where the top-hat distributions flatten out and the multiple-jet and merged-peak distributions become more rounded. Error measures for distributions with jets or peaks located near the edges of the domain are higher than for the same feature located near the center of the domain for both FDDI and AFDDI reconstructions. Reconstruction errors tend to rise when non-zero features in a distribution are located near the edges of the measurement domain because in FDDI and AFDDI corrections are required to remove contributions of the basis functions from regions outside the measurement domain and the projection matrix is bounded to force the reconstructed distribution to zero at the edges of the domain. Distributions consisting of centered gaussian peaks were used to investigate the effects of spatial gradients on reconstruction and representation errors (see Figure 3.13). Gaussian peaks were normalized on a -1 to 1 grid (arbitrary length units) such that the double integral of the distribution over the grid is 1, and the standard deviation was varied to obtain different two dimensional concentration distributions and gradients in the phantom projection measurement. Projection gradients are calculated for every line-of-sight in a set of projection data and are given by $dp(s, \theta)/ds$. Reconstruction results for these distributions show that reconstruction and representation errors are lowest using FDDI when the maximum projection gradient in a set of projection measurements is less than approximately 60 units^{-1} , where “units” indicate the length units of the domain. Below this value of projection gradient, AFDDI performance is unpredictable resulting in highly variable reconstruction error measures. Compared to the total reconstruction errors, low AFDDI representation errors at low projection gradient suggest that good reconstructions should be possible using the AFDDI basis functions and that the high reconstruction errors are most likely due to errors in retrieval. For the range of projection gradients between 60 units^{-1} and approximately 110 unit^{-1} ,

reconstruction and representation errors are comparable for FDDI and AFDDI. Above a projection gradient of 110 units^{-1} , AFDDI errors are the lowest. Shifting the Gaussian peaks away from the center of the domain helps to reduce errors in the AFDDI reconstructions at low projection gradient while increasing the reconstruction error in both FDDI and AFDDI for projection gradients above 60 units^{-1} .

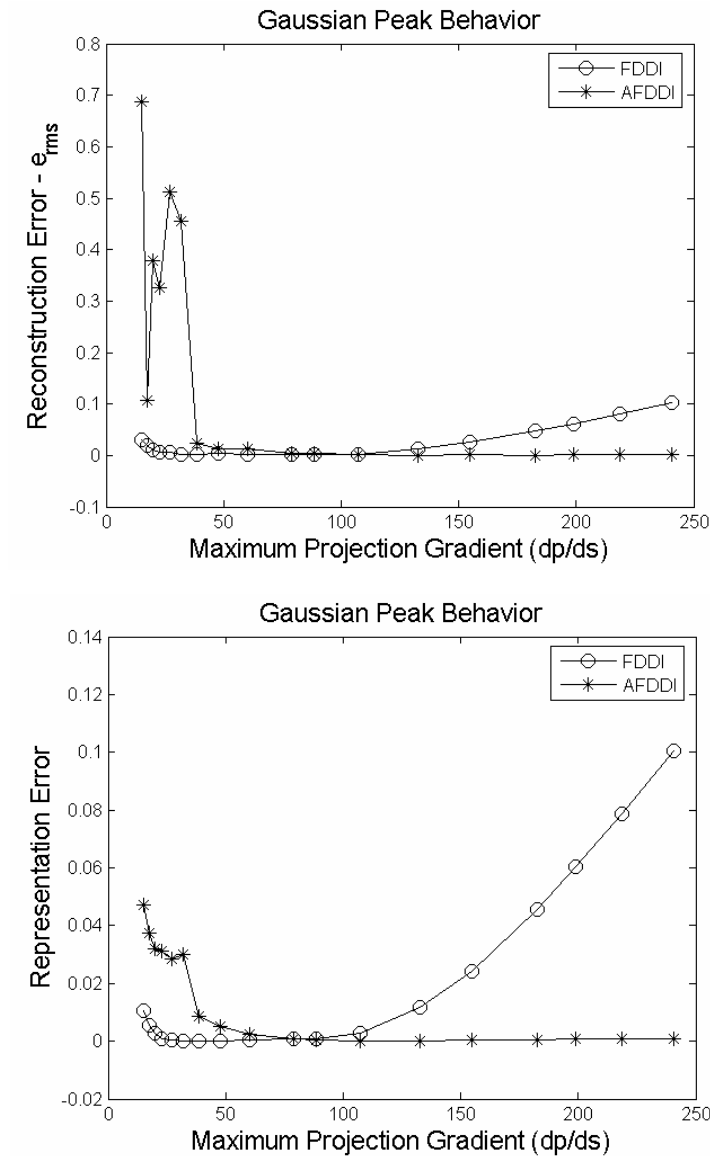


Figure 3.13. Reconstruction and representation errors for gaussian peak distributions.

The sensitivity of AFDDI to small variations in projection data was tested by adding error to the phantom projection data as follows:

$$p'_i = p_i(1 + e_m \cdot \gamma_i) \quad (3.14)$$

where the p'_i 's are the “noisy” phantom projection data given at a specific line-of-sight i , the p_i 's are the original phantom projection data, e_m is the percentage noise magnitude, and the γ_i 's are random numbers between -1 and 1 . Noise was added at 5% and 10% levels (e_m set to 0.05 and 0.10) to test error sensitivity to noise of the reconstruction results. Though the reconstruction problem is ill-posed, both the AFDDI and FDDI reconstruction methods perform well under these conditions with the reconstruction error increasing by less than 20% in the majority of cases with the addition of 5% noise to the projection data. Reconstruction errors increased more significantly with the addition of 10% noise to the projection data; however rms error measures remain below 0.7, compared to measurements with no noise added. Sample results for one distribution are shown in Table 3.2. In cases where AFDDI produces high reconstruction errors, the addition of noise to the projection data helps to reduce the largest AFDDI reconstruction errors, see Table 3.3 for an example. Representation errors for both FDDI and AFDDI are largely unaffected by the addition of noise to the projection data as the selection of the additional basis function locations is unchanged in most cases. However, if large noise spikes or systematic noise were present in multiple view angles of the projection measurements (e.g. in multiple detectors), AFDDI basis function selection could be affected. Though the noise would be due to the detector or other electronics, it could incorrectly be reconstructed as part of the distribution, affecting AFDDI basis function selection.

Table 3.2. Sample reconstruction error results for a phantom distribution with noisy projection measurements.

	<i>FDDI</i>			<i>AFDDI</i>		
	e_{rms}	e_{abs}	e_{max}	e_{rms}	e_{abs}	e_{max}
no noise	0.341	0.496	0.675	0.148	0.176	0.212
5% noise	0.341	0.495	0.681	0.169	0.198	0.240
10% noise	0.346	0.502	0.683	0.315	0.367	2.533

Table 3.3. Sample reconstruction error results for a case with high AFDDI reconstruction error.

	<i>FDDI</i>			<i>AFDDI</i>		
	e_{rms}	e_{abs}	e_{max}	e_{rms}	e_{abs}	e_{max}
no noise	0.112	0.134	0.153	0.427	0.346	1.9917
5% noise	0.112	0.134	0.168	0.145	0.153	0.198
10% noise	0.114	0.134	0.174	0.136	0.145	0.473

Previous studies of AFDDI performance had determined that the addition of more than 50 adaptive basis functions did not have a significant effect on reconstruction error [4]. However, the investigations of AFDDI performance presented here using a square top hat phantom distribution show that there can be a significant effect on reconstruction accuracy caused by the number of basis functions added in AFDDI. Changes in the spatial extent of the top hat distribution show that for a large distribution covering approximately 20% of the measurement domain or more, reconstruction errors increase as the spatial extent of the distribution is increased when using AFDDI with 50 additional basis functions. Representation

errors remain low indicating that the ability of AFDDI to represent the broader distributions is good but that there are errors in the retrieval of the reconstruction weighting factors. Reconstruction and representation errors for two different square top hat profiles are presented in Table 3.4. The square top hat distributions were expressed on a grid spanning -10 mm to 10 mm in the x and y axes. The sizes of the top hat distributions were varied from 6x6 (i.e. spanning -3 mm to 3 mm in the x and y directions) to 10x10. Results show that while representation error is continuously lowered by the addition of more basis functions, reconstruction error is not always lowered, indicating an increase in retrieval error for some cases. Results also indicate that the number of basis functions needed to produce the lowest reconstruction error depends in part on the spatial extent of the distribution to be reconstructed.

Table 3.4. Effect of the addition of basis functions on AFDDI representation and reconstructions errors.

<i>basis functions</i>	<i>6x6 square top hat</i>		<i>10x10 square top hat</i>	
	<i>e_{rms}</i>	<i>rep error</i>	<i>e_{rms}</i>	<i>rep error</i>
30	0.067	0.058	0.196	0.102
40	0.057	0.050	0.149	0.082
50	0.058	0.048	0.210	0.068
60	0.058	0.048	0.106	0.063
70	0.086	0.047	0.124	0.055

AFDDI reconstructions of top-hat distributions often show significant structure on the top of the reconstructed peak. This structure is due in part to the use of high aspect ratio basis functions for reconstruction and to the limited number of basis functions used in regions of lower spatial gradient. Clearly, the high aspect ratio basis functions are unable to represent flat, smooth features in areas where they are not

closely packed, resulting in rippling and spikes in the reconstructed distribution. Applying a spatial filter to the reconstructed results is one way to reduce the rippling and spikes and smooth the AFDDI reconstructions. Though not applied to the top-hat reconstruction discussed here, a Gaussian spatial filter can be designed to reduce the small features seen in the reconstructions while preserving the large-scale flow features [23].

The dependence of AFDDI reconstructions on the distribution orientation with respect to the LOS measurement configuration was investigated using a triangular top hat distribution and rotating it about its centroid. Reconstruction errors were found to have a significant dependence on the orientation (see Figure 3.14) and often to be low when the distribution was oriented such that one side of the top hat was perpendicular to the lines-of-sight of a view. It should be noted that for AFDDI the location of the additional basis functions is highly dependent on the orientation of the distribution, affecting the representation and reconstruction errors. AFDDI representation error remained low but fluctuated significantly from 0.04 to 0.12 with rotation while FDDI

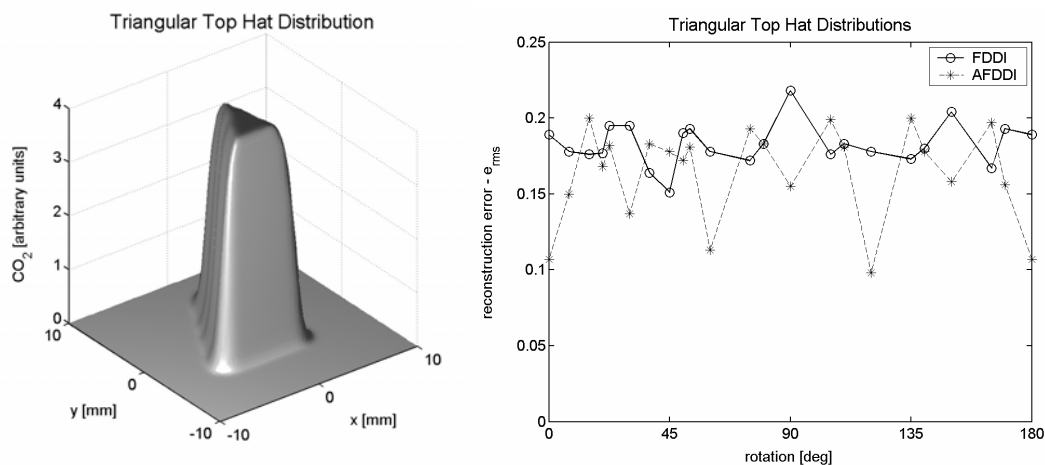


Figure 3.14. Triangular top hat distribution rotated at 0 degrees and reconstruction errors of the triangular distribution under rotation.

representation error remained fairly constant at 0.14 to 0.16.

Analyses of multiple types of phantom distributions were performed in order to test AFDDI. AFDDI performed well using measurement configurations of 306, 522, and 1050 LOSs. Reconstructions errors were shown to be dependent on gradients in the projection measurements with FDDI performing well in cases of low gradient and AFDDI performing better than FDDI in cases of high gradient. Errors in the reconstruction were often larger in areas of low or zero spatial gradients, where the basis functions were not closely packed. Additional errors can be due to noise in the projection measurements. While noise in the projection measurements generally increased reconstruction errors, both FDDI and AFDDI performed well in the presence of noise. Though reconstruction errors generally increased in the presence of noise, they remained comparable to error measurements computed for phantom data with no noise added. Orientation, location, and size of features in the phantom distributions were shown to effect reconstruction accuracy. Errors increased in both FDDI and AFDDI when distribution features were located near the domain boundaries due to the inability of the limited number of basis functions in boundary regions to fully represent these features. It was determined that the number of basis functions added to the AFDDI basis set can have a significant effect on the reconstruction accuracy, specifically in cases where the spatial extent of the features to be reconstructed cover a large portion of the domain. While representation errors were lowered with the addition of basis functions, there is a tradeoff with increasing retrieval error. Overall, AFDDI performed well with error measures comparable to or lower than FDDI error measures.

3.9 Summary and Conclusions

An IR absorption facility for making LOS measurements on confined and unconfined, reacting and nonreacting flows has been designed and constructed. The facility is capable of making simultaneous measurements of LOS absorption over six viewing angles, collecting 1050 LOS measurements in approximately 1.5 ms for high temporal resolution. CO₂ absorption measurements have been made with a KCl:Li color center laser operating at approximately 2.69 μm. The CCL beam is electro-optically modulated at 1 MHz for phase sensitive detection to improve signal to noise ratios. The measurements were made on an 8 mm x 8 mm forced square jet composed of a mixture of CO₂ and air. Jet forcing at 30 Hz was provided by a speaker driven by an audio power amplifier. Representative projection data show good control of noise and of interference due to ambient CO₂ fluctuations in the laser paths.

The measurements presented in this paper are for large CO₂ concentrations of 25% and greater by volume. Lower CO₂ concentrations in the range of 5-15% can be expected for hydrocarbon combustion applications. Interference in the measurement process due to ambient H₂O, which may absorb at certain wavelengths within the CCL tuning range, ambient CO₂ absorption, and electrical signal noise are the primary causes of reduced signal-to-noise ratios and can make low-concentration measurements difficult. Increasing the laser intensity and selecting an appropriate detector with low noise levels and high sensitivity would be primary concerns for practical applications in which CO₂ concentrations are low and low absorption levels are expected. As a demonstration of the IR absorption facility, the measurements presented here have shown good control of measurement errors and reasonable signal levels for CO₂ levels of 25-50%. However, extra care must be taken to reduce these errors for measurement of low concentrations. Tomographic reconstruction results of data for 8.4% CO₂ collected using the IR absorption facility show more significant

reconstruction artifacts than for the 25-50% CO₂ level results presented here. However, the reconstruction results still capture the square top-hat nature of the flow in the case of low (8.4%) CO₂ levels. These results indicate that it is possible to record projection measurements of low concentration flows for tomographic reconstructions though additional noise and error-reduction procedures would be necessary, possibly including electronics and hardware (e.g. wiring) modifications for noise control and additional signal or data filtering.

Tomographic reconstruction of projection data collected by the 6-module IR absorption facility is performed using Adaptive Finite Domain Direct Inversion. Resulting reconstructions are filtered using a Gaussian filter to reduce reconstruction artifacts while maintaining the large-scale structures. Reconstructions of the CO₂ field in forced jets of 3 m/s and 6 m/s were performed. Reconstructions of the 6 m/s jet show less effects of forcing on the CO₂ field when compared to reconstructions of the 3 m/s jet which show significant modulation. Additional absorption measurements of various combustion products (CO₂, H₂O, NO, and NO₂) can be performed using the KCl:Li color center laser with the IR absorption facility. The laser wavelength range can be extended to the 2.25-2.65 μm range by using a KCl:Na crystal to permit measurement of CO [7]. Additional flow rates and forcing parameters (frequency, forcing signal power) can be investigated using the IR absorption facility. These data could then be used to study the dominant gradients and spreading in the jet as well as mixing. Coupled with velocity or vorticity studies, concentration data could provide more detailed information regarding the structures and dynamics of these jets.

Performance of Adaptive FDDI has been evaluated using various phantom distributions of jet/peak configurations as well as high gradient triangular and square top hat distributions. Results show that, relative to FDDI, AFDDI performs better for distributions that contain high gradient regions, such as top hat distributions, and

produces reconstruction errors lower than those of FDDI in many of these high gradient cases. AFDDI does not always produce lower reconstruction errors than FDDI and may fail to reduce errors in cases where the distribution contains a wide range of spatial gradients. Investigations performed on Gaussian peaks of varying standard deviation show that there are three ranges of spatial gradient magnitudes that affect the performance of AFDDI. At low magnitudes (less than 60 units^{-1}) FDDI produces the lowest reconstruction and representation errors, while AFDDI performance is unpredictable. At high magnitudes (greater than 110 units^{-1}), AFDDI consistently produces the lowest errors. Finally, there is an intermediate range of magnitude (60 units^{-1} to 110 units^{-1}) in which AFDDI and FDDI performance is comparable. Errors in the reconstruction occurred often in areas of low or zero gradient magnitude, where the basis functions were not closely packed.

The effects of orientation, location, and size of features on reconstruction performance were investigated. Reconstructions of a high gradient square top hat show that AFDDI performance is dependent on the nonzero spatial extent of a distribution and the number of additional basis function used in the reconstruction. For accurate reconstructions, the number of additional basis functions used in AFDDI must be sufficient to thoroughly cover the high gradient regions of the distribution. AFDDI reconstructions can be improved by increasing the number of basis functions added in the AFDDI procedure when the distribution to be reconstructed covers a large portion of the domain. In addition, reconstruction performance is dependent on distribution orientation as well as location in the domain. Errors increased in both FDDI and AFDDI when absorption features were located near the domain boundaries due to the inability of fewer basis functions in these regions to fully represent the features.

Reconstruction performance was evaluated in the presence of measurement noise. While noise in the projection measurements generally increased reconstruction errors, both FDDI and AFDDI performed well with reconstruction errors remaining comparable to measurements with no noise added. Overall, AFDDI performed well with error measures comparable to or lower than FDDI error measures for all reconstructions performed in this study.

We have demonstrated that high quality tomographic data can be collected using the IR absorption facility. Coupling the IR absorption facility with Adaptive Finite Domain Direction Inversion has yielded a valuable tool for the analysis of non-reacting and reacting, steady and unsteady flows. Additional modifications to the facility, including changes to the laser and detectors, could further enhance the range of possible species and concentrations that can be measured for a variety of applications.

Acknowledgements

The support of the U.S. Navy under ONR grant # N00014-99-1-0447 with Dr. Gabriel Roy as scientific officer is gratefully acknowledged.

References

- [1] Feng, M.Y. and Gouldin, F.C., "Evaluation of a New Tomographic Inversion Method Applied to Jet Flows," *AIAA 98-0726*.
- [2] Hansen, P.C., *Rank-Deficient and Ill-Posed Problems*, SIAM, Philadelphia, PA, 1998.
- [3] Ravichandran, M., Gouldin, F.C. "Reconstruction of smooth distributions from a limited number of projections," *Applied Optics*, **27**:4084, 1988.
- [4] Ha, J., Feng, M., Gouldin, F.C. "Laser tomographic reconstruction in a complex concentration flow field," *AIAA-99-0444*, 1999.
- [5] Feng, M., Gouldin, F.C. "Experimental evaluation of an adaptive tomographic inversion method," *AIAA 2000-0949*, 2000.
- [6] Kak, A.C., and Slaney, M., *Principles of Computerized Tomographic Imaging*, IEEE Press, New York, 1988.
- [7] Chojnacki, A.M., Wolga, G.J., Gouldin, F.C., "Infrared color center laser systems for tomographic determination of temperature and species concentration distributions in combusting systems." *Combustion Science and Technology*, **134**, 165-181, 1998.
- [8] Chojnacki, A.M., Sarma A., Wolga, G.J., Tornianen, E.D., Gouldin, F.C. "Infrared tomographic inversion for combustion and incineration." *Combustion Science and Technology*, **116-117**, 583-606, 1996.
- [9] Pollock, C.R. *Color Center Lasers, Encyclopedia of Physical Science and Technology*, **Vol. 7**, 164, Academic Press, Inc., New York, 1987.
- [10] Feng, M.Y., Gouldin, F.C., Edwards, J.L. "Scanning for high speed laser absorption tomography." *AIAA 2001-0791*.
- [11] Swanson, N.L., Billard, B.D., and T.L. Gennaro, "Limits of optical transmission measurements with application to particle sizing techniques," *Applied Optics*, Vol. 38, No. 27, pp. 5887-5893, 1999.
- [12] Radon, J., "Über die Bestimmung von Funktionen durch ihre Integralwerte langsgewisser Mannigfaltigkeiten," *Ber. Sachsische Akad. Wiss. Leipzig Math. Phys. Kl.*, Vol. 69, pp, 262-267, 1917.
- [13] Deans, S.R., *The Radon Transform and Some of its Applications*, Wiley-Interscience, New York, 1983.
- [14] Sonka, M., Hlavac, V., and Boyle, R., *Image Processing: Analysis and Machine Vision*. Thomson Engineering, 1998.

- [15] Groetsch, C.W., *Inverse Problems in the Mathematical Sciences*, Vieweg, Wiesbaden, Germany, 1993.
- [16] Orfanidis, S.J., *Introduction to Signal Processing*, Prentice Hall, New Jersey, 1995.
- [17] Golub, G.H., and Van Loan, C.F. *Matrix Computations*. Johns Hopkins University Press, 1985.
- [18] Feng, M.Y., *Development of a Real-Time Tomography System for Combustion*, Ph.D. thesis, Cornell University, Ithaca, N.Y., 2000.
- [19] Lewitt, R.M., "Reconstruction Algorithms: Transform Methods," Proc. IEEE, Vol. 71, pp. 390-408, 1983.
- [20] Verhoeven, D., "Limited-data computed tomography algorithms for the physical sciences," *Applied Optics*, **32**: 3736-3754, 1993.
- [21] Censor, Y., "Finite Series Expansion Reconstruction Methods," Proc. IEEE, Vol. 71, pp. 409-419, 1983.
- [22] Herman, G.T., *Image Reconstructions from Projections: The Fundamentals of Computerized Tomography*. Academic Press, 1980.
- [23] Gonzales, R., and Woods, R., *Digital Image Processing*. Prentice Hall, 2002.

Chapter 4

Emission Tomography for Gas Turbine

Combustor Control

Jennifer L. Edwards¹ and Frederick C. Gouldin²

Cornell University, Ithaca, NY 14853

Sandor Becz³

ABAQUS, Inc., Providence, RI 02909

ABSTRACT

The development of a sensor system that can be used in a practical combustion device for the purpose of feedback control of a combustor exit temperature distribution is discussed in this work. Combustor operating states can be defined by distributions of composition, temperature, and pressure that result from the control of a combustion system through fuel-injection or acoustic modulation of flow through the system. In this study, computational simulation of a combustor sector rig provided combustor

¹ Graduate Student, Sibley School of Mechanical and Aerospace Engineering.

² Professor, Sibley School of Mechanical and Aerospace Engineering.

³ Aerospace Engineering Specialist, ABAQUS, Inc

operating states that were defined by the percentages of fuel-flow through the injectors, resulting in excited state population and temperature distributions specific to each state. Emission tomography measurements were simulated using numerical line-of-sight integration of simulated excited state number densities of water for two emission transitions. Tomographic reconstruction was performed using Tomographic Reconstruction via a Karhunen-Loeve Basis (TRKB) which utilizes an optimal basis set to reduce the number of basis functions and thereby measurement lines-of-sight required for reconstruction. TRKB reconstructions of excited state populations and temperature were used to evaluate nine line-of sight measurement configurations and an optimal measurement configuration was selected. Operating state identification for control applications was investigated using the TRKB reconstructions.

4.1 Introduction

Active control of combustion systems is a focus of current research and development [1-12]. Monitoring and feedback control is of great potential importance in applications such as power generators, waste incinerators, furnaces, and gas turbines for propulsion. Detection of off-design conditions, control of combustion instability, and maintenance of peak performance are primary goals in the development of an active control system for combustion [1-3]. Many control systems have focused on controlling thermoacoustic instabilities [5-10], most notably pressure oscillations, to prevent degradation of system performance. Other control systems have been developed to maintain stable and efficient combustion through optimization in the form of operating state control [11,12] where operating conditions may be adjusted to optimize combustor efficiency, minimize emissions, control emission composition, and temperature distribution within a combustor. An active feedback

control system requires the measurement of combustor operating conditions using sensors from which the operating state of the system can be determined. Control can be accomplished through direct modulation of fuel or air injection into the system or through the use of acoustic actuators that modulate the flow in response to control signals that are supplied by a control sensor [1-3].

Several important metrics in the evaluation of gas turbine engine performance include emissions, efficiency, and, for turbojets, thrust generated. These engine characteristics are related in part to the temperature distribution at the combustor exit, often quantified by the engine *pattern factor*. Specifically, the pattern factor is a simple measure of the maximum deviation from the average combustor exit temperature [13]. In gas turbine engines, uniform combustor exit temperature distributions are desirable because large temperature gradients can have detrimental effects on engine turbine blades, influencing engine reliability, longevity, and maintenance cost [14]. Determination of the engine pattern factor gives an indication of the temperature non-uniformity but does not provide information on the spatial distribution of temperature. Knowledge of the entire temperature distribution is useful for the evaluation of combustor mixing, temperature dependent emissions – including CO and Nox, engine efficiency, and thrust generated [14]. Measurements of temperature distributions at the combustor exit have included the use of thermocouples [15], thin film sensors, and laser absorption techniques [13]. These measurements are capable of making limited temperature measurements at relatively few spatial locations or lines-of-sight and can be limited in temporal response. One powerful technique for collecting extensive spatially and temporally resolved data is multiple line-of-sight tomography and reconstruction [16-20]. Tomography is a powerful technique for obtaining spatial distributions of scalars from sets of quantitative line-of-sight measurements. Analysis of line-of-sight data via

tomographic reconstruction yields two-dimensional scalar distributions such as species concentration, excited state populations, and temperature.

In general, tomographic measurements can be made in various ways including laser absorption, nuclear magnetic resonance imaging, X-ray tomography, positron emissions, and radiant emissions, the approach used in this study [17-25]. Absorption and emission tomography are commonly used in the physical sciences in situations where optical access is available and knowledge of spatial distributions in a system is desired (e.g. monitoring in flow or combustion applications) [16-25]. Application of tomography can yield information on combustor exit concentration and temperature distributions over the entire spatial extent of the combustor exit, which is useful for determining and controlling combustor performance. As an alternative to physical probe measurements, tomography is a non-intrusive method that can be used to determine the state of a system and to quantitatively measure conditions in an object or flow. Cross sections of an object or a flow field can be imaged through measurements of emission, transmission or reflection data from multiple lines-of-sight and angles of view [16-25]. An image is then computationally reconstructed from “projection measurements” that are path-integrated measurements of a quantity of interest (e.g. radiation intensity, absorption, etc.) along a set of lines-of-sight. While both absorption and emission tomography are commonly used, emission measurements offer advantages over other measurement techniques, particularly when probing a practical combustion system. Such measurements are single-ended; only collection optics, a spectral resolving element, and a detector such as a radiometer or photodetector are needed for measurement of emitted radiation at chosen wavelengths and lines-of-sight, compared to absorption measurements that require a radiation source at one end of a line-of-sight and a detector at the other end. Emission tomography can be used to reconstruct both species concentration and temperature

distributions while eliminating the need for a radiation source, thereby reducing the complexity of the measurement system.

The quality of a tomographic reconstruction is highly dependent on the number and orientation of the line-of-sight projection measurements [16-20,26]. Thorough measurement coverage of the domain of interest is necessary, often resulting in the need for many overlapping lines-of-sight. Thus, a major challenge in the design of an optical tomography system is the requirement for extensive optical access for measurement of radiation transmitted through or emitted from a medium along multiple, overlapping lines-of-sight distributed over multiple viewing angles. In practice, the physical constraints of many combustion systems and the desire to reduce the modifications necessary for sensing limit the location and number of line-of-sight measurements possible. A goal of the research reported here is to minimize the required number of lines-of-sight and optimize a line-of-sight measurement configuration through comparative analysis of tomographic reconstructions resulting from different measurement configurations.

Evaluation of a tomographic sensor requires the analysis of tomographic reconstructions. For accurate tomographic reconstructions, a reconstruction method well suited to the measurement configuration and distributions to be measured is necessary. The number and location of line-of-sight measurements is important to both the design of a tomography sensor and the choice of reconstruction method. As discussed above, relatively few line-of-sight measurements are desired for application of a tomographic sensor to a practical combustion system. Developed at Cornell University, one reconstruction approach that requires a small number of line-of-sight measurements but incorporates *a priori* information is a series expansion method called Tomographic Reconstruction via a Karhunen-Loeve Basis (TRKB) [16,18,27,28]. This reconstruction technique is based on a series expansion using an

optimal basis set obtained from Proper Orthogonal Decomposition (POD) of an ensemble of distributions [27-30]. POD produces a set of eigenfunctions that represent the principal components of a set of data. Use of these eigenfunctions as the TRKB basis set adapts the basis set to the distributions in the ensemble for efficient tomographic reconstruction.

A priori data in the form of ensembles of expected distributions (e.g. molecular excited state concentration distributions), termed the “training set”, are necessary for POD and can be obtained through physical sampling or computational simulation of an ensemble of combustor operating states. In turn, data in the form of combustor distributions of concentration, temperature, and pressure are needed to generate these training sets. Since empirical measurements of these quantities are difficult and are not available for the combustor in this work, computational simulations are used to generate the expected distributions.

Combustor exit temperature fields can be determined using the statistical mechanical relationships between species populations of two excited states. The measurement of emission at two distinct wavelengths yields the data necessary for reconstruction of the species distributions. Therefore, the choice of emission tomography as a sensor and desire to determine temperature distributions require the simulation of line emission from at least two excited states of a chosen species. Using the simulation data, excited state species populations are computed and TRKB training sets of population and temperature distributions are developed.

The development of a sensor system that can be used in a practical combustion device for the purpose of feedback control of the combustor exit temperature distribution is discussed in this work. The development of rugged, compact sensors that measure radiation and advanced tomographic reconstruction techniques makes tomography a promising approach to measurements in a practical combustion device

[1,16,18,26-28,31,32]. The primary objectives of the research reported here are to evaluate the potential for emission tomography for operating state identification and to demonstrate an approach for selecting an optimal tomographic line-of-sight measurement configuration. This is accomplished through evaluation of combustor simulation data describing operating states and through prediction of sensor performance using different measurement configurations. Practical concerns associated with the development of a tomography system are addressed in this work, including choice of measured species, measurement wavelengths, and tomographic reconstruction technique.

The remainder of this paper begins with a discussion of the tomographic reconstruction problem and TRKB method in Section 4.2. The determination of species population and exit temperature distributions using emission tomography are presented and the application of tomography for state identification and control is discussed. Combustion simulation and emission measurement modeling are presented in Section 4.3, including a brief review of the relevant statistical mechanical relationships and discussion of measurement wavelength selection. Results of an analysis of several different line-of-sight measurement configurations and the related tomographic reconstructions are discussed in Section 4.4. Efficacies of the different line-of-sight configurations are evaluated through comparison of reconstruction results and error measures of excited state populations and the related temperature distributions. An optimal measurement configuration is chosen and application of tomographic reconstruction results to the identification of the combustor operating state for the purpose of combustion control is discussed. The POD procedure and sample results of POD applied to excited state population distributions determined from simulation data are presented in the Appendix.

4.2 Tomographic Reconstruction via a Karhunen-Loeve Basis

4.2.1 Tomographic Reconstruction Problem

Tomographic reconstruction is the reconstruction of a distribution, e.g. radiant emission distribution, from projections. *Projections* are defined as the integral of the distribution along lines-of-sight specified by view angle, θ and offset, s . For spatially inhomogeneous distributions, multiple line-of-sight measurements are required at different view angles for reconstruction of the distribution. For reconstruction of a scalar distribution, $f(y,z)$, measurements are made at a set of view angles, $\{\theta\}$, and offsets, $\{s\}$, that result in a line-of-sight along direction t as shown in Figure 4.1.

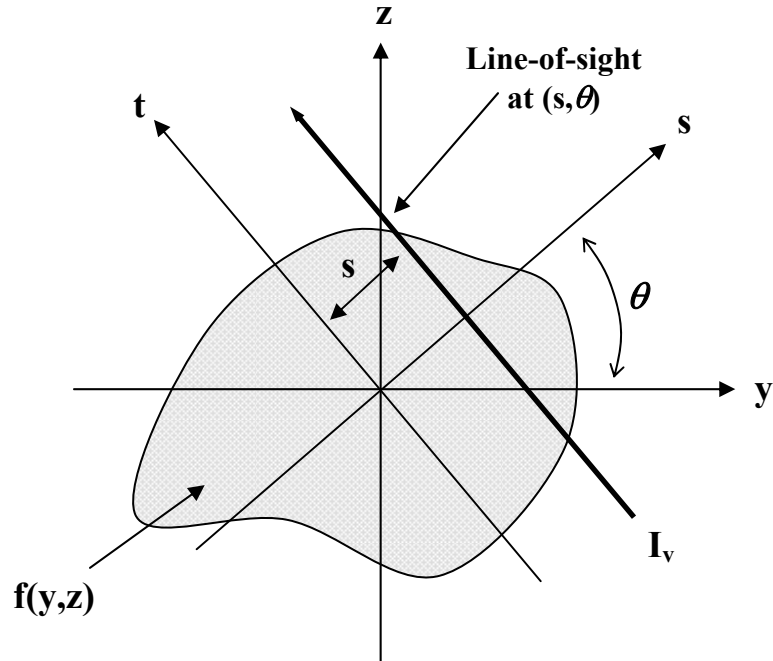


Figure 4.1. Tomographic measurement geometry. Measurement of intensity, I_v , is performed along a line-of-sight in the t direction, defined by offset, s , and viewing angle, θ .

In general, the tomographic projection for a line-of-sight defined by s and θ (see Figure 4.1) is given by the line-integral of the distribution $f(y,z)$ along that line-of-sight

$$p(s, \theta) = \int_{-\infty}^{\infty} f(y, z) dt . \quad (4.1)$$

Using the coordinate transform

$$\begin{aligned} y &= s \cos \theta - t \sin \theta \\ z &= s \sin \theta + t \cos \theta \end{aligned} \quad (4.2)$$

Equation (4.1) can be rewritten as

$$p(s, \theta) = \int_{-\infty}^{\infty} f(s \cos \theta - t \sin \theta, s \sin \theta + t \cos \theta) dt = \mathfrak{R}(f) . \quad (4.3)$$

This is known as the Radon transform of $f(y,z)$ for which an explicit inversion is known [19]. Because measurements are only available at a limited number of discrete view angles and offsets, the practical reconstruction problem for $f(y,z)$ is ill-posed and the explicit inversion formula for the Radon transform cannot be used.

Various methods have been used to reconstruct two-dimensional spatial distributions from projections. The two primary types of tomographic reconstruction method are based on Fourier transforms and finite series expansions respectively [19,20]. Transform methods are generally used in medical applications where accuracy is of vital importance and generality is needed with respect to the distributions to be reconstructed. Standard transform methods used for reconstruction are backprojection algorithms, which require little or no *a priori* information about the distribution to be reconstructed [20]. The main drawback of backprojection algorithms is the need for numerous line-of-sight measurements at many viewing angles for accurate reconstructions. Series expansion methods are better suited to applications where limited line-of-sight measurements are possible and *a priori* information such as non-negativity is available. These methods include reconstruction

algorithms such as the Algebraic Reconstruction Technique (ART) [20], Finite Domain Direction Inversion (FDDI) [26], and Tomographic Reconstruction via a Karhunen-Loeve Basis (TRKB) [16,18,27,28], the method that is used in this work. These techniques are often used in the physical sciences where numerous line-of-sight measurements are difficult to acquire and distributions are typically smooth and of low contrast [20].

The TRKB method approximates a discretized distribution $f(y_i, z_j)$ in an expansion of basis functions, $\phi_l(y_i, z_j)$.

$$f(y_i, z_j) \cong \sum_{l=1}^{N_B} \alpha_l \phi_l(y_i, z_j) \quad (4.4)$$

$$i=1, \dots, N_y, \quad j=1, \dots, N_z$$

where α_l are the basis function weighting coefficients, i and j are the indices for each discrete grid point, N_y and N_z are the number of grid points in the y and z directions respectively (equal to 48 in each direction for this work), and N_B is the number of basis functions used in the expansion. The reconstruction problem is reduced to finding the basis function coefficients given the set of projection measurements, $\{p(s, \theta)\}$. The coefficients $\{\alpha_l\}$ are determined from solution of an overdetermined least squares problem

$$D\alpha = p. \quad (4.5)$$

D is an $M_N \times N_B$ projection matrix containing line integrals of the basis functions along the measurement lines-of-sight used for reconstruction, α is a N_B vector of basis function coefficients, and p is a M_N vector of projection measurements. M_N is the total number of line-of-sight projection measurements available. It is necessary for the number of line-of-sight measurements to be greater than the number of basis functions used in the expansion, i.e. $M_N > N_B$, for the least-squares problem to be overdetermined.

Tomographic reconstruction is accomplished by solution of the least-squares problem (4.5) through minimization of the norm

$$\|D\alpha - p\|. \quad (4.6)$$

Significant *a priori* information can be incorporated into the problem solution through the use of a basis function set derived from an ensemble of expected distributions to be reconstructed. Proper Orthogonal Decomposition of the ensemble provides an optimal set of basis functions that incorporate *a priori* information including non-negativity and the primary features evident in the ensemble distributions. However, if a limited number of basis functions is used for reconstruction, errors in the reconstruction may include negative values. To ensure non-negativity of the reconstructed distribution, a constraint is applied to the problem, such that $f(y,z) > 0$. For the discrete problem of computationally simulated distributions investigated in this work, the constraint is applied at each grid point (y_i, z_j) in the domain such that

$$0 < \sum_{l=1}^{N_B} \alpha_l \phi_l(y_i, z_j) \quad (4.7)$$

$$i=1, \dots, N_y, \quad j=1, \dots, N_z$$

The problem including this constraint can be restated in matrix form as

$$\min \|D\alpha - p\| \quad \text{subject to } B\alpha > h \quad (4.8)$$

where B is a $N_p \times N_B$ matrix containing the values of each basis function at all points (y_i, z_j) and h is a vector of constraints set equal to zero for this problem. N_p is the total number of grid points in the simulated data, equal to $N_x * N_y$. This is a linear least squares problem with linear inequality constraints. The reader is referred to Reference 26 for details on the solution methodology.

4.2.2 TRKB Basis Set Development

A major challenge in the design of a tomography sensor for practical applications is the determination of a line-of-sight measurement configuration. As discussed previously, given the physical constraints and limited optical access of practical hardware such as an engine combustor, it is important to minimize the required number of line-of-sight measurements such that extensive modifications to the system can be avoided. Use of an optimum set of basis functions for the tomographic reconstruction minimizes the number of measurements required. The advantage of using the TRKB method for reconstruction is the use of an optimal set of basis functions derived from the Karhunen-Loeve (KL) procedure, commonly termed Proper Orthogonal Decomposition (POD) [16,18,27,28]. POD is a mathematical procedure that produces an optimal orthonormal set of eigenfunctions for an ensemble of distributions [16,18,27-30]. The eigenfunctions are optimal in the sense that they are calculated to have the smallest mean squared error compared to any other basis set in representing the ensemble of distributions for any fixed number of terms in a series expansion. Calculation of the KL eigenfunctions for use as the TRKB basis set requires *a priori* knowledge of a set of expected distributions, termed the *training set*. In this work, computational simulations have provided distributions of temperature, pressure, and species needed to develop the training sets of species excited state number density and temperature distributions at the exit of a gas turbine engine combustor. Details of the training set development and POD analysis are presented in Section 4.3 and the Appendix respectively.

Determination of species population and temperature distributions at the combustor exit from line-of-sight measurements is accomplished using emission tomography. Tomographic projection measurements of radiant emissions can be related to the population of a species in a specific molecular state via the equation of

radiative transfer. For emissions at frequency, ν , the radiant intensity I_ν measured at distance r for a spontaneous emission dominated process simplifies (see below) to

$$I_\nu = \int_0^r n_2 A_{21} h\nu d\hat{r} \quad (4.9)$$

where n_2 is the population of a species in an excited state and A_{21} is the Einstein coefficient for spontaneous emission from an excited energy state 2 to a lower energy state 1. The Einstein coefficient and emission frequency are known for a measurement system based on a chosen frequency and molecular transition, and the distribution of the excited state species population density n_2 over the domain can be reconstructed from projection measurements using TRKB as described previously. Reconstructions of population distributions for two separate excited states resulting from measurements at two separate emission frequencies can be used to determine the temperature distribution at the combustor exit. For the line-of-sight configuration evaluation presented in this work, emission from two specific molecular transitions is modeled as a line integral according to Equation (4.9). A review of the statistical mechanics and radiative transfer relevant to these calculations is presented in Section 4.3. Though the line-of-sight configuration evaluation does not include effects from practical measurement applications, these effects are discussed in Section 4.3.3.

4.2.3 Error Measures

Comparison of tomography results with training sets of species population and temperature distributions allows for evaluation of errors in the tomographic reconstructions. Three error measures are often used for quantitative comparisons of reconstruction results [16,17,20]: 1) the *normalized root mean square error*, also

called the *reconstruction error*, e_{rms} ; 2) the *normalized mean absolute error*, e_{abs} ; and 3) the *maximum error*, e_{max} . e_{rms} emphasizes a few large errors in the reconstruction, while e_{abs} emphasizes many small errors. The error measures are defined as

1) Normalized rms error

$$e_{rms} = \frac{\|f(y_i, z_j) - f_{rec}(y_i, z_j)\|_F}{\|f(y_i, z_j) - \bar{f}\|_F} \quad (4.10)$$

where

$$\bar{f} = \sum_{i=1}^{N_y} \sum_{j=1}^{N_z} \frac{f(y_i, z_j)}{N_y N_z} \quad (4.11)$$

2) Normalized absolute error

$$e_{abs} = \frac{\sum_{i=1}^{N_y} \sum_{j=1}^{N_z} |f(y_i, z_j) - f_{rec}(y_i, z_j)|}{\sum_{i=1}^{N_y} \sum_{j=1}^{N_z} |f(y_i, z_j)|} \quad (4.12)$$

3) Normalized maximum error

$$e_{max} = \frac{\max(|f(y_i, z_j) - f_{rec}(y_i, z_j)|)}{f(y_{max}, z_{max})}. \quad (4.13)$$

In the equations above, $f(y_i, z_j)$ is the actual distribution to be reconstructed, $f_{rec}(y_i, z_j)$ is the reconstructed distribution, (y_{max}, z_{max}) is the spatial location of the largest error, and $\|\cdot\|_F$ denotes a Frobenius norm.

Limiting the number of basis functions used in the TRKB reconstructions places some, if not all, of the distributions in the ensemble outside the span of the basis functions. Given a basis set composed of all available POD eigenfunctions, all

distributions from the ensemble would be within their span and errors in the reconstruction would result only from the inability of the reconstruction algorithm to retrieve the proper basis function weighting coefficients. For reconstructions outside the span of the basis set, reconstruction errors will result from both the inability of the basis set to exactly represent a distribution from the ensemble, termed *representation error*, and from errors in the retrieval of the weighting coefficients, termed *retrieval error*. The overall *reconstruction error* is composed of the sum of representation and retrieval errors. The *best representation* of a distribution $f(y,z)$ using a subset of N_B eigenfunctions is given by

$$f_{best}(y, z) = \sum_{l=1}^{N_B} \beta_l \phi_l(y_i, z_j) \quad (4.14)$$

where the weighting coefficients $\{\beta\}$ are obtained from the inner product of eigenfunctions in the basis set with the actual distributions to be reconstructed. The representation error, e_{rep} , can then be calculated as

$$e_{rep} = \frac{\|f(y_i, z_j) - f_{best}(y_i, z_j)\|_F}{\|f(y_i, z_j) - \bar{f}\|_F}. \quad (4.15)$$

Retrieval error, e_{ret} , is calculated as

$$e_{ret} = \frac{\|f_{best}(y_i, z_j) - f_{rec}(y_i, z_j)\|_F}{\|f_{best}(y_i, z_j) - \bar{f}_{best}\|_F}. \quad (4.16)$$

4.2.4 Evaluation of Tomography for Control using TRKB

The determination of combustor exit plane temperature distributions is of interest for combustion control applications where knowledge of the operating state

can be used to improve combustor performance. It is possible to identify the operating state of the combustor by matching the population and temperature distributions determined using emission tomography to those produced by the computational simulation. For this work, state identification is accomplished through a least-squares fit of the weighting factors for each reconstructed distribution to the best representation weighting factors. Simulation data of 18 combustor operating states results in 18 unique sets of best representation weighting coefficients $\{\beta\}$ to identify the operating states. Reconstruction of each n_A , n_B , or temperature distribution using TRKB results in a set of reconstructed weighting coefficients, $\{\alpha\}$. Because the basis set for TRKB reconstructions is the same basis set used for producing the best representations, comparisons of the TRKB weighting coefficients $\{\alpha\}$ and the best representation weighting coefficients $\{\beta\}$ can be used for state identification purposes. Given a set of TRKB weighting coefficients for a distribution, it is possible to find the closest match of these weighting coefficients to all possible best representation weighting coefficients by minimizing the norm $\|\{\alpha\} - \{\beta\}\|$ for all possible unique sets of $\{\beta\}$, allowing for identification of the actual operating state distribution from the set of 18 possible distributions, and hence the operating state associated with it.

Nine configurations of line-of-sight measurements are considered in this investigation. To determine an optimum measurement configuration for combustion control, tomographic reconstruction errors and state identification capabilities are evaluated for all combustor operating states.

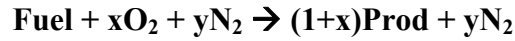
4.3 Combustor Simulations and Modeling of Emission Measurements

4.3.1 Combustor simulation

The determination of operating conditions using emission tomography requires the measurement of radiation caused by emission from excited molecular states. In addition, a set of expected distributions is required to calculate a set of basis functions for reconstruction using TRKB. These data can be collected through physical measurements or produced through numerical simulation of the flow. For this study, data are produced through numerical simulation such that excited state populations necessary to simulate emitted radiation can be computed. These excited state populations and temperature distributions can then be used for the generation of TRKB basis functions.

Simulated combustor exit plane temperature, pressure, and fuel/air ratio distributions were provided for a Pratt & Whitney combustor sector rig. Allstar, a Pratt & Whitney proprietary CFD flow solver was used to provide these distributions [33,34]. Allstar solves the Reynolds-averaged Navier-Stokes equations on unstructured or structured meshes for the entire combustor domain. It is a pressure-based, finite-volume flow solver that discretizes the conservative form of the governing equations using second order centered differencing. For combustor applications, the standard $k-\varepsilon$ model for turbulence is used with wall function near-wall modeling. In order to provide a good representation of flame structure and heat release and a reasonably accurate determination of local flame temperature, a combustion model based on the Magnussen-Hjertager Eddy Breakup Model is used.

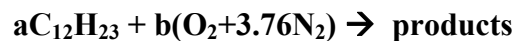
Assuming infinitely fast chemistry acceptable for the high combustor pressures and temperatures, the chemistry mechanism is based on the simplified reaction:



For further details on the computational solution method, the reader is referred to Malecki, et. al [33].

The computational fluid dynamics (CFD) combustor nozzle representation consisted of a flameholder with four fuel injectors located on either side (for a total of eight). Fuel injectors were grouped into three zones: an outer zone of two fuel injectors, a middle zone consisting of the four center fuel injectors, and an inner zone of two fuel injectors. Operating states were specified by the percentages of fuel in each of the three injector zones. Eighteen operating states were included in the analysis with Jet-A as the fuel, modeled as $C_{12}H_{23}$ with a molecular weight of 167.32 g/mole.

A single nozzle of a four-nozzle combustor rig was modeled for the CFD simulation, see Figure 4.2. Periodic boundary conditions on the single nozzle were applied during the simulation. Simulation data were collected at the exit plane of the combustor, measuring 8.0645 cm by 7.62 cm (3.5 in by 3 in) and located 16.51 cm (6.5 in) downstream of the fuel injectors. Temperature, pressure, and molar fuel/air ratio distributions were output onto a 48x48 grid at the exit plane (see Figure 4.3 for sample distributions). The computation simulations provided molar fuel/air ratios, FA , that were calculated as



$$FA = \frac{a}{b} = \frac{moles(fuel)}{moles(air)} \quad (4.17)$$

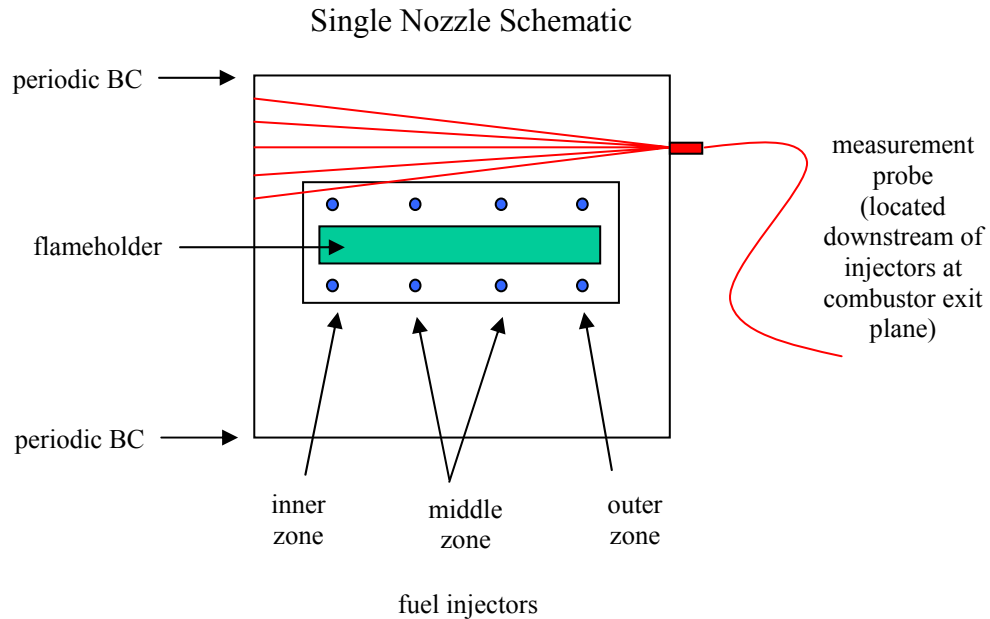


Figure 4.2. CFD single nozzle schematic.

Product composition was determined through equilibrium calculations where temperature, pressure, and reactant mole fractions (determined from the fuel/air ratios as shown in (4.17)) are used to calculate product composition at each grid point. Chemical equilibrium calculations were performed using Cantera, an open-source software package for problems involving chemically-reacting flows, including combustion. Cantera was developed by Dr. D.G. Goodwin at the California Institute of Technology and is available at <http://www.cantera.org>.

4.3.2 Modeling of Emission Measurements

The choice of emission tomography as a sensing technique and computation of population and temperature distributions from measured emission data require the simulation of line of sight emissions from excited states of a chosen species. To

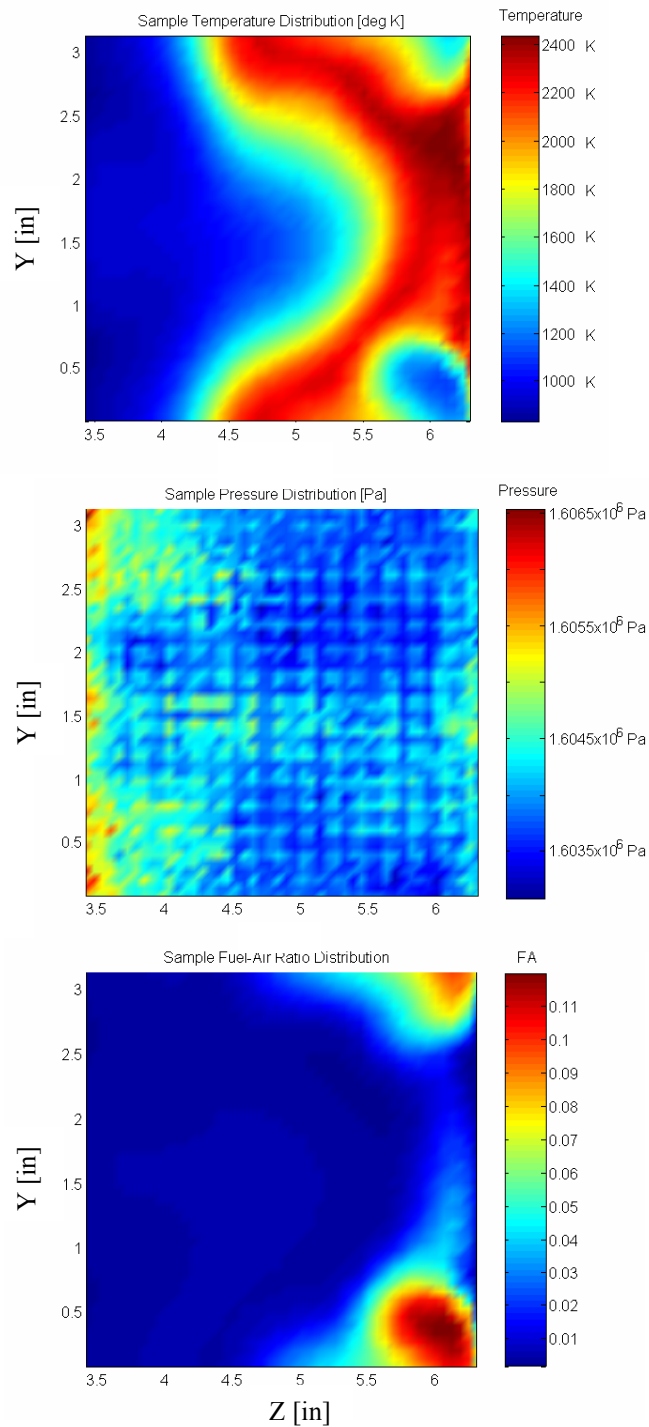


Figure 4.3. Sample temperature, pressure, and fuel-air ratio distributions provided by CFD simulations. Though the pressure values vary little over the sample distribution seen in the center, the discretization of the distribution on the computational grid creates the pattern seen in the sample pressure distribution, and is amplified by the color scaling.

evaluate the performance of the tomographic sensor described in this work, it is necessary to model radiant emission measurements given the pressure, temperature, and product composition obtained from the combustor simulation data. It is useful to first briefly review the statistical mechanics required for the analysis of radiant emissions and to relate radiation intensity to excited state species number densities and combustor exit temperature distributions.

In this investigation, emission measurements are simulated at the exit plane of a research combustor. Spontaneous radiant emission occurs during a transition from an excited state (i.e. upper energy level) of an atom or molecule to a lower energy level [35,36]. In a molecular gas, changes in rotational, vibrational, and electronic states can occur simultaneously [37]. The energy of the emitted photon, $h\nu$, is given by the difference in energy between the two states. Consider the emission of radiation due to a transition from an excited state 2 to a lower state 1. The Einstein coefficient for spontaneous emission, denoted A_{21} , is a measure of the probability per unit time for a spontaneous transition from state 2 to state 1 [35,36]. The rate of emission is proportional to the number density of molecules in the excited state 2, n_2 . For an ideal gas, the number density of molecules in state 2 can be calculated using the Boltzmann distribution [35,38]

$$n_2 = n \frac{g_2 e^{-\varepsilon_2/kT}}{Q}, \quad (4.18)$$

where n is the total number density of the emitting species in the gas, g_2 is the degeneracy of the molecular energy level 2, ε_2 is the energy of level 2, k is Boltzmann's constant, T is the temperature of the gas, and Q is the molecular partition function. For this investigation we consider radiant emissions from H₂O molecules. The internal molecular partition function for water is often written as the product of the vibrational, rotational, and electronic contributions, [35,38] i.e.

$$Q_{\text{int}} = Q_v Q_r Q_e. \quad (4.19)$$

Rotational and vibrational energies are coupled through interacting modes of vibration and rotation [39]. A combined ro-vibrational partition function, Q_{vr} , can be introduced and the internal partition function rewritten as

$$Q_{\text{int}} = Q_{vr} Q_e \quad (4.20)$$

Electronic excited states for water lie well above the dissociation energy of the system, thus, Q_e can be assumed to be unity [39]. Values for the ro-vibrational partition function of H₂O at temperatures up to 6000 K have been calculated [39], and it is seen that the ro-vibrational partition function can be presented in analytic form as

$$\log Q_{vr} = \sum_{i=0}^6 a_i (\log T)^i \quad (4.21)$$

where the a_i 's are coefficients used to fit the calculated values of Q_{vr} to the formula above [39]. Equation (4.21) is the form of the partition function used in this work.

Specific ro-vibrational emission lines of water are chosen for the simulated emission. Given the above form for Q_{vr} , the number density of water molecules in a specific ro-vibrational state (i.e. excited state 2) at temperature T is given by

$$n_2 = n_{H_2O} \frac{g_2 e^{-\varepsilon_2/kT}}{Q_{vr}}. \quad (4.22)$$

The total number density of water molecules in the combustion products is given by

$$n_{H_2O} = \chi_{H_2O} n = \chi_{H_2O} \frac{p}{kT} \quad (4.23)$$

where χ_{H_2O} is the mole fraction of H₂O and p is the pressure. Emission measurements made at two separate frequencies correspond to transitions from excited energy levels A and B and can be used to determine temperature through the relation

$$\frac{n_A}{n_B} = \frac{g_A}{g_B} \exp\left(\frac{-(\varepsilon_A - \varepsilon_B)}{kT}\right). \quad (4.24)$$

Here, g_A , g_B , and ε_A , ε_B refer to the degeneracies and energy levels of the excited states A and B respectively. Data for the upper state energy levels are taken from experimentally derived energy levels of H₂O presented in Reference 40. The HITRAN database provides weighted transition-moments squared, R_{21} , for each transition in Debye² [Debye²=10⁻³⁶ ergs cm³], and the Einstein coefficient A_{21} can be calculated from the transition-moments according to [41]

$$A_{21} = \frac{64\pi^4}{3h} \bar{\nu}_{21}^3 \frac{g_1}{g_2} \mathfrak{R}_{21} \times 10^{-36}. \quad (4.25)$$

Here h is Planck's constant and $\bar{\nu}_{21}$ is the wavenumber ($1/\lambda$) of the photon emitted in the transition from excited state 2 to the lower state 1.

It is possible to calculate the radiation emitted by an excited species using the species number densities and transition Einstein coefficients. Following the analysis in Vincenti & Kruger [35], for steady-state conditions and non-degenerate molecular transitions, the equation of radiative transfer for radiation of frequency ν along a line-of-sight in direction r is given by

$$\frac{\partial I_\nu}{\partial r} = n_2 A_{21} h\nu + n_2 B_{21} I_\nu h\nu - n_1 B_{12} I_\nu h\nu. \quad (4.26)$$

The three terms in Equation (4.26) correspond to contributions from spontaneous emission, induced emission, and absorption respectively with Einstein coefficients A_{21} ,

B_{21} , and B_{12} . I_ν is the specific radiation intensity and $h\nu$ is the energy of a radiative molecular transition from an excited to lower state. Using relations between the Einstein coefficients and equilibrium populations for an ideal gas one can show that

$$\frac{A_{21}}{B_{21}} = \frac{2h\nu^3}{c^2}, \quad \frac{B_{12}}{B_{21}} = 1, \quad \text{and} \quad \frac{n_2}{n_1} = e^{-h\nu/kT}, \quad (4.27)$$

and the equation of radiative transfer can be rewritten as

$$\frac{\partial I_\nu}{\partial r} = n_1 B_{12} h\nu \left[(1 - e^{-h\nu/kT}) B_\nu(T) + e^{-h\nu/kT} I_\nu - I_\nu \right]. \quad (4.28)$$

The three terms in brackets represent the contributions of spontaneous emission, induced emission, and absorption as above. $B_\nu(T)$ is the Planck function, k is Boltzmann's constant, c is the speed of light, and T is temperature.

$$B_\nu(T) = \frac{2h\nu^3/c^2}{e^{h\nu/kT} - 1} \quad (4.29)$$

For a process to be emission-dominated such that spontaneous emission dominates over induced emission and absorption the radiating medium must be *optically thin*.

The *optical depth*, τ_ν , is defined as

$$\tau_\nu(r) = \int_0^r n_1 B_{12} h\nu (1 - e^{-h\nu/kT}) d\hat{r} \quad (4.30)$$

where \hat{r} is a running variable of integration. Optically thin conditions apply if $\tau_\nu(r) \ll 1$ for all distances r in the domain of interest. For the engine combustor temperature and concentration distributions provided by the CFD simulations for this investigation, numerical integration of the optical depth for the transitions chosen confirm optically thin conditions with typical values of the optical depth less than 10^{-2} .

Neglecting any background radiation from the wall at distance r_s , the solution to the equation of radiative transfer (4.28) is

$$I_v = \int_0^r n_1 B_{12} h\nu (1 - e^{-h\nu/kT}) B_v(\hat{r}) e^{-\tau_v(\hat{r})} d\hat{r}. \quad (4.31)$$

Contributions from background radiation sources in practical applications are addressed in Section 4.3.3. Using equilibrium population relations, Einstein coefficients, and the Planck function, this can be rewritten for optically thin conditions as

$$I_v = \int_0^r n_2 A_{21} h\nu \left(\frac{e^{h\nu/kT}}{e^{h\nu/kT} - 1} \right) d\hat{r}. \quad (4.32)$$

The term in parentheses is approximately equal to one such that the intensity measured at distance r for a spontaneous emission dominated process simplifies to

$$I_v = \int_0^r n_2 A_{21} h\nu d\hat{r} \quad (4.33)$$

which is consistent with Equation (4.26) when the stimulated emission and absorption contributions are removed. The specific intensity in W/m²-sr-m can be easily evaluated through numerical integration of the excited state populations along chosen lines-of-sight.

Water was chosen for the emission measurements in this investigation due to the large number density of molecules present as one of the major products of combustion. In addition, water has several strong emission lines within the spectral range captured by available emission sensors [40-43]. The choice of energy levels for measurement is determined by the strength of the H₂O emission lines in the spectral range of interest (700-1150 nm), and the absence of additional strong lines from other major combustion products near the chosen emission line [31,32]. Vibrational states are presented in the standard mode notation of ($\nu_1\nu_2\nu_3$) where the vibrational quantum numbers are ν_1 (symmetric stretch), ν_2 (bending), and ν_3 (asymmetric stretch) [37,40]. Rotational states are labeled using standard asymmetric top notation of J_{K_a,K_c} where J

is the rotational angular momentum and K_a and K_c are the values of the angular momentum for corresponding prolate and oblate symmetric tops [37,40]. Based on the HITRAN database [42,43], two measurement wavelengths for H₂O emission from ro-vibrational lines that met the criteria stated above were selected, and measurements were simulated at 936 nm (transition A) corresponding to a $(300) 8_{7,2} \rightarrow (000) 9_{4,5}$ transition and at 1130 nm (transition B) corresponding to two overlapping transitions $(111) 9_{8,1} \rightarrow (000) 9_{8,2}$ and $(111) 9_{8,2} \rightarrow (000) 9_{8,1}$. Differences in Einstein A_{21} coefficients for overlapping transitions in B are negligible (<1%) and an average value of the Einstein A coefficients is used. H₂O Einstein A coefficients and transition line strengths from HITRAN are presented in Figure 4.4.

In the Section 4.4, tomographic line-of-sight configurations are evaluated using simulated projection data of intensity determined by the line integral in Equation (4.33). This approach is sufficient for the purposes of line-of-sight configuration evaluation using TRKB. It will be necessary to include the effects of measurement over a finite volume, finite solid angle, and finite spectral resolution in practical applications. Section 4.3.3 evaluates the potential for practical measurements through estimation of the line emission and background signal strengths.

4.3.3 Practical Emission Estimates

This section first outlines the procedure for predicting emission signal levels in a general manner for a practical application. Simplifications in the analysis are then made where reasonable for the goal of signal estimation in the measurement configurations presented in this work.

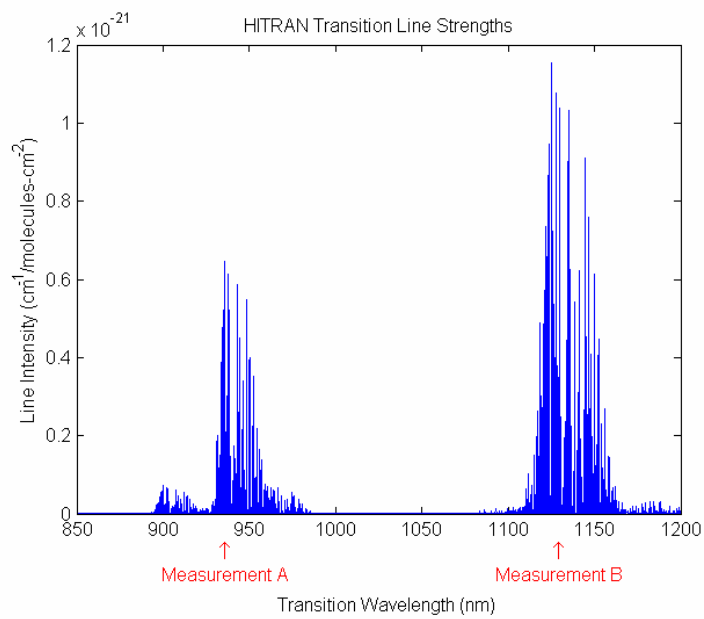
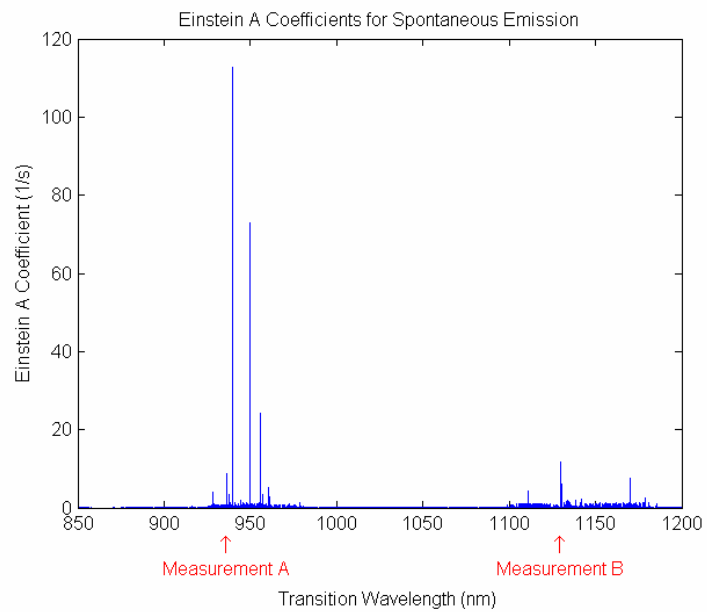


Figure 4.4. H₂O spectral information provided by HITRAN.

In practical emission tomography, light collection is not restricted to a small differential solid angle and to a single line-of-sight but rather is distributed over finite solid angle and a bundle of lines-of-sight that define a finite volume. The measured quantity, neglecting absorption, can be expressed as the volume integral over space and solid angle of the product of the emission coefficient $j_\nu(x,y,z)$, density ρ , and a measurement system response function $g_\nu(x,y,z,\phi,\chi:\theta,s,t)$ that accounts for the performance characteristics of the light collection system at the frequency ν . In $g_\nu(x,y,z,\phi,\chi:\theta,s,t)$, ϕ and χ define the orientation of a light ray emitted from a differential emitting volume, dV . At a distance t_a along a measurement line-of-sight, emitted light is collected from a finite volume over a finite solid angle with a collection efficiency that may vary with spatial position and collection angle. The emitting volume which is being measured and the collection solid angle are defined by the collecting optics and vary with position along t_a , see Figure 4.5. Consider an emitting volume ΔV that is disk-shaped with a thickness dt_a and cross sectional area ΔA_s such that $\Delta V = \Delta A_s dt_a$. The variation in the system response function, g_ν over the volume of the disk accounts for any spatial variation in collection efficiency. Light emitted from a differential volume, dV , in this disk can be defined by the differential cross sectional area dA that is imaged onto the detector, and the thickness dt_a of the emitting volume such that $dV = dA dt_a$. The light emitted from dV and collected over a differential solid angle, $d\Omega$, is given by

$$\rho j_\nu(x,y,z) g_\nu(x,y,z,\phi,\chi:\theta,s) dV d\Omega(\phi,\chi), \quad (4.34)$$

where ϕ and χ define the orientation of a light ray emitted from dV . Integration of this product over space and collection solid angle Ω for fixed s and θ gives the light collected at frequency ν from the line-of-sight defined by s and θ . In turn, integration

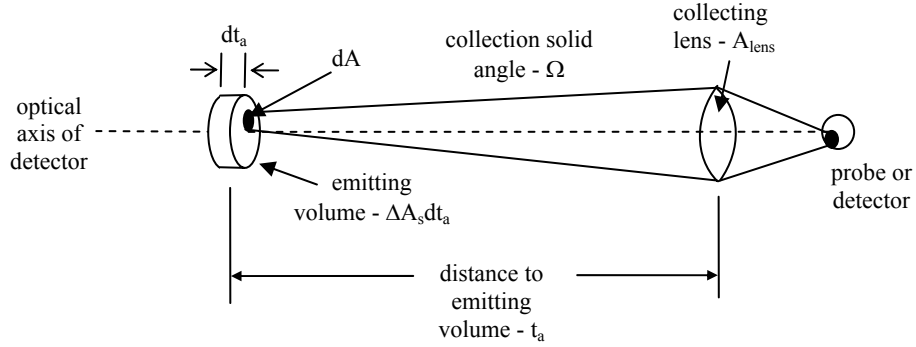


Figure 4.5. Line-of-sight collection geometry assuming practical collection optics. The collection optics define the solid angle and emitting volume that vary with position along t_a . Note that the emitting area, ΔA_s , is small and of the same order of magnitude as the thickness dt_a . The emitting distribution is integrated along the line in the direction t_a as described by Equation (4.36).

over ν gives the light collected by a measurement along the line-of-sight defined by s and θ yielding the tomographic projection,

$$p(s, \theta) = \iiint_{\Delta V \Omega \nu} \rho j_\nu g_\nu d\nu d\Omega dV . \quad (4.35)$$

The integration is over all light frequencies, solid angle, and emitting volume collected by the optics and detector. The practical emission projection measurements in Equation (4.35) can be rewritten as

$$\hat{p}(s, \theta) = \sum_{nm} \left(\int_{\nu} \int_{t_1}^{t_2} \int_{\Omega} \int_{\Delta A_s} A_{nm} h\nu n_n(y, z) \phi_{nm}(\nu) g_\nu dA d\Omega dt_a d\nu \right) \quad (4.36)$$

where projection measurements of intensity are summed over all $n \rightarrow m$ H₂O transitions within the detector bandpass with indices n and m denoting the upper (excited) and lower states of each transition within the summation. Line-of-sight limits of integration across the measurement domain are denoted t_1 and t_2 . Projection

measurements in Equation (4.36) are integrated over the light collection solid angle, Ω , emitting area, ΔA_s , distance along the line-of-sight, t_a , and frequency, ν . For each transition, there is an associated line shape function, $\phi_{nm}(\nu)$, that describes the variation in line emission with frequency.

For the estimation of predicted signal strengths, we assume that the collection solid angle is independent of the position of the differential emitting volume in physical space, the emitting volume ΔV is a cylinder centered on the optical axis of the detector with cross-section ΔA_s , and the frequency band pass is a top hat profile. Since transition line widths are small in comparison to the detector bandpass, it is assumed that the entire transition line is within the detector bandpass and the line shape can be simplified to a Dirac delta function at each transition frequency, ν_{nm} . While these assumptions are not necessary, they significantly simplify the analysis. For the calculation of projections from computer simulation data, we further assume that the component of gradients of property values perpendicular to the measurement plane are small and this variation is neglected. With these assumptions, emission projection measurements from Equation (4.36) can be written as

$$\hat{p}(s, \theta) = \sum_{nm} \left(\int_{t_1}^{t_2} \int_{\Omega} \int_{\Delta A_s} A_{nm} h \nu_{nm} n_n(y, z) dA d\Omega dt_a \right). \quad (4.37)$$

In order to estimate signal strengths in a practical manner, it is necessary to consider a sensor capable of withstanding the harsh environment of combustors. Such sensors must be extremely robust to allow for continuous operation in a combustion control application. In addition, compactness of sensors is of primary concern to minimize the modifications necessary for incorporation into an engine. Advanced sensors capable of fulfilling these requirements are currently under development. For example, a fiber-optic probe and remote spectrograph with readout-unit capable of

collecting thermal radiation over the visible and near infrared spectral range has been developed and tested [31,32]. These probes are capable of a spectral resolution of 2 nm at FWHM over a spectral range of approximately 700-1150 nm. Both single and five-fiber probes have been developed to allow for measurement of a single view defined by line-of-sight angle and offset or multiple views in a fan-like shape. The probes measure ¼ inch in diameter, allowing for incorporation into the wall of a combustor with minimal intrusiveness. They are capable of withstanding temperatures of up to 270 °C (520 °F) without cooling and with cooling could be placed close to the combustion zone. Emission spectra of water, O₂, and black body radiation have been measured using the these probes and readout-unit [31,32].

Given the geometry of these fiber-optic probes and of the measurement lines-of-sight, it is possible to estimate the collection solid angle Ω of the collecting optics (including a focusing lens) and fiber probe or detector. The arrangement of the fiber probe and focusing lens correspond to some area from which radiation is emitted along the line-of-sight and captured by the detector. Both the collection solid angle and emitting area ΔA_s vary due to changes in focus along the line-of-sight, but as noted, this variation is neglected. To estimate solid angle and emitting area, it is assumed that the optics are focused at the average midpoint for all lines-of-sight in a measurement configuration. Assuming the smallest relevant length scale is on the order of the computational grid cell size, the emitting area of the radiating source can be estimated as the area of a cell. For the combustor geometry investigated here, the exit plane is discretized on a 48×48 grid with cells measuring 0.159 cm × 0.168 cm, yielding an emitting area of $\Delta A_s = 2.67 \times 10^{-6} \text{ m}^2$. The collection solid angle is based on the area of the focusing lens and distance from the emitting volume to the lens. Because emission projection measurements are determined by the line integral of emission along the line-of-sight t_a , the separation distance L from the collecting optics

to the emitting volume varies over the measurement domain, resulting in changes in the collection solid angle. However, using line-of-sight configuration 9 as a representative measurement configuration (see Section 4.4), an estimate of the average solid angle Ω can be made based on a lens to sample distance of $L=3.81$ cm (1.5 in), which is the average distance to the sample line-of-sight midpoints. Previous applications of the fiber-optic probes noted above have incorporated a 7 mm diameter lens for collection, giving a lens area of $A_{lens}=3.85 \times 10^{-5}$ m². The corresponding collection solid angle is computed as

$$\Omega = A_{lens} / L^2 \quad (4.38)$$

yielding an estimate of 0.0265 steradians. Given that the emitting area is estimated as the computational grid cell size, a negligible variation in excited state population over the emitting area is assumed and we can eliminate the integration over area and solid angle in Equation (4.37). For a constant solid angle, the H₂O line emission signal, S_{H_2O} , can be approximated according to:

$$\hat{p}(s, \theta) = \sum_{nm} \left(\int_{t_1}^{t_2} A_{nm} h\nu_{nm} n_n(s, \theta) \int_{\Omega} \int_{\Delta A_s} dA d\Omega dt_a \right) \quad (4.39 \text{ a})$$

$$S_{H_2O} = \hat{p}(s, \theta) = \Delta A_s \cdot \Omega \cdot \sum_{nm} \left(\int_{t_1}^{t_2} A_{nm} h\nu_{nm} n_n dt_a \right) \quad (4.39 \text{ b})$$

Estimates of background radiation from the hot combustor walls are necessary for comparison with H₂O line emissions to determine if line emission signals are large enough to be measurable in the presence of background radiation. The combustor walls are assumed to have an emissivity of one, and the background radiation, S_{bgd} , is

approximated by blackbody radiation, $B_\lambda(T)$, emitted within the 2 nm spectral band of the detector from λ_1 to λ_2 centered at each of the measurement wavelengths.

$$\begin{aligned}
 S_{bkgd}(T) &= \Omega \cdot \Delta A_s \cdot \int_{\lambda_1}^{\lambda_2} B_\lambda(T) d\lambda \\
 &= \Omega \cdot \Delta A_s \cdot \int_{\lambda_1}^{\lambda_2} \frac{2hc^2}{\lambda^5 (e^{hc/\lambda kT} - 1)} d\lambda
 \end{aligned} \tag{4.40}$$

A combustor liner temperature of $T=1600$ °F (1144 K) is used to approximate the background radiation. Using measurement configuration 9 as a representative line-of-sight configuration, approximate H₂O emission signal strengths range from $S_{H_2O} = 5$ -30 nW with background emissions of $S_{bkgd} = 35$ -140 nW. With a wall emissivity of one assumed, it is likely that background signals are overestimated for the temperature specified. In order to collect the H₂O line emission signals in this situation it would be necessary to use a method such as tuning the detectors across the emission line of interest to accurately determine both the background and line emission signals. The background signal due to the combustor wall could then be removed from the emission signals leaving only H₂O line emission data to be used in the tomographic analysis as presented in this paper. In addition, since the optical depth is very small, stronger H₂O emission lines could be selected without violating the small optical depth assumption.

While Equations (4.34)-(4.40) take into account the practical considerations of measurement for signal estimations, recall that simplified projection measurements are simulated at two single transition energies for use in the tomographic evaluation of various line-of-sight measurement configurations, which is presented in the Results section. For the tomographic measurements simulated in this paper, the distribution to be reconstructed is the excited state population for each transition. Phantom

projection measurements of intensity with the geometry shown in Figure 4.1 are given by the line integration in Equation (4.33)

$$p(s, \theta) = \int_{t_1}^{t_2} A_{21} h\nu n_2(s, \theta) dt = A_{21} h\nu \int_{t_1}^{t_2} n_2(s, \theta) dt \quad (4.41)$$

where A_{21} and the energy of the transition, $h\nu$, are constants and have been pulled out of the integral, and t_1 and t_2 are the limits of integration across the combustor domain. The tomographic projection measurements were evaluated according to Equation (4.41) for H₂O emission lines at two specific transitions, neglecting emission from additional transitions $n \rightarrow m$ in the detector bandpass. A_{21} and n_2 in Equation (4.41) correspond to the Einstein coefficient and excited state number density for each measured transition A and B at wavelengths λ_A and λ_B . The omission of detector responsivity, H₂O transition line shapes, emitting source and detector areas, and solid angle effects is not expected to have a significant effect on the tomographic analysis in the Results section of this paper. It is noted that it is also possible to include the practical measurement considerations such as collection solid angle and emitting area variation in the integrals of the basis functions contained in the TRKB D matrix. However, due to the complexity involved in this calculation, it was considered outside the scope of the present investigation.

4.4 Results

The TRKB method is used to test various line-of-sight measurement configurations for application to the combustor shown in Figure 4.2. Emission measurements are simulated by numerical integration of Equation (4.41), producing simulated intensity measurements resulting from radiant emission due to molecular transition along the lines-of-sight specified by a measurement configuration.

Eigenfunctions resulting from POD of molecular excited state distributions were used as TRKB basis functions, yielding an optimum basis set. Details on the POD procedure are included in the Appendix. Numerical integration of each basis function along the specified lines-of-sight yields the elements of the projection matrix D . Examples of excited state distributions and the resulting eigenfunctions for transition A are presented in Figure 4.6 and Figure 4.7 respectively; results for transition B are similar. Eigenfunction spectra for the two transitions are presented in Figure 4.8.

Nine line-of-sight measurement configurations were evaluated for the combustor nozzle represented in the CFD simulations. Because future experimental measurements are under consideration for testing of an actual combustor, practical line-of-sight configuration limitations were taken into account. Given the annular shape of an engine combustor, measurement probes must be placed at locations along the outer regions of the annulus. Installation of fiber optic probes such as those of References 31 and 32 would require forming holes of several millimeters or more in diameter through the combustor liner. Minimizing the number of holes necessary for measurements is an important practical concern as modifications to the combustor are both difficult and costly. The use of multiple-fiber probes [31,32] that can make multiple line-of-sight measurements is one way to reduce the number of modifications made to the combustor while providing enough measurement lines-of-sight for the least-squares problem to be overdetermined. Consequently, 5-view probes were utilized in most of the measurement configurations studied. Nine line-of-sight configurations were evaluated using TRKB reconstructions of the water n_A and n_B distributions. These configurations are shown in Figure 4.9. Note that while configurations 5 and 8 appear to have five probes each, due to the periodicity of the boundary conditions, the five LOS from one probe have been split across the boundaries at the minimum and maximum Y locations such that only four probes are

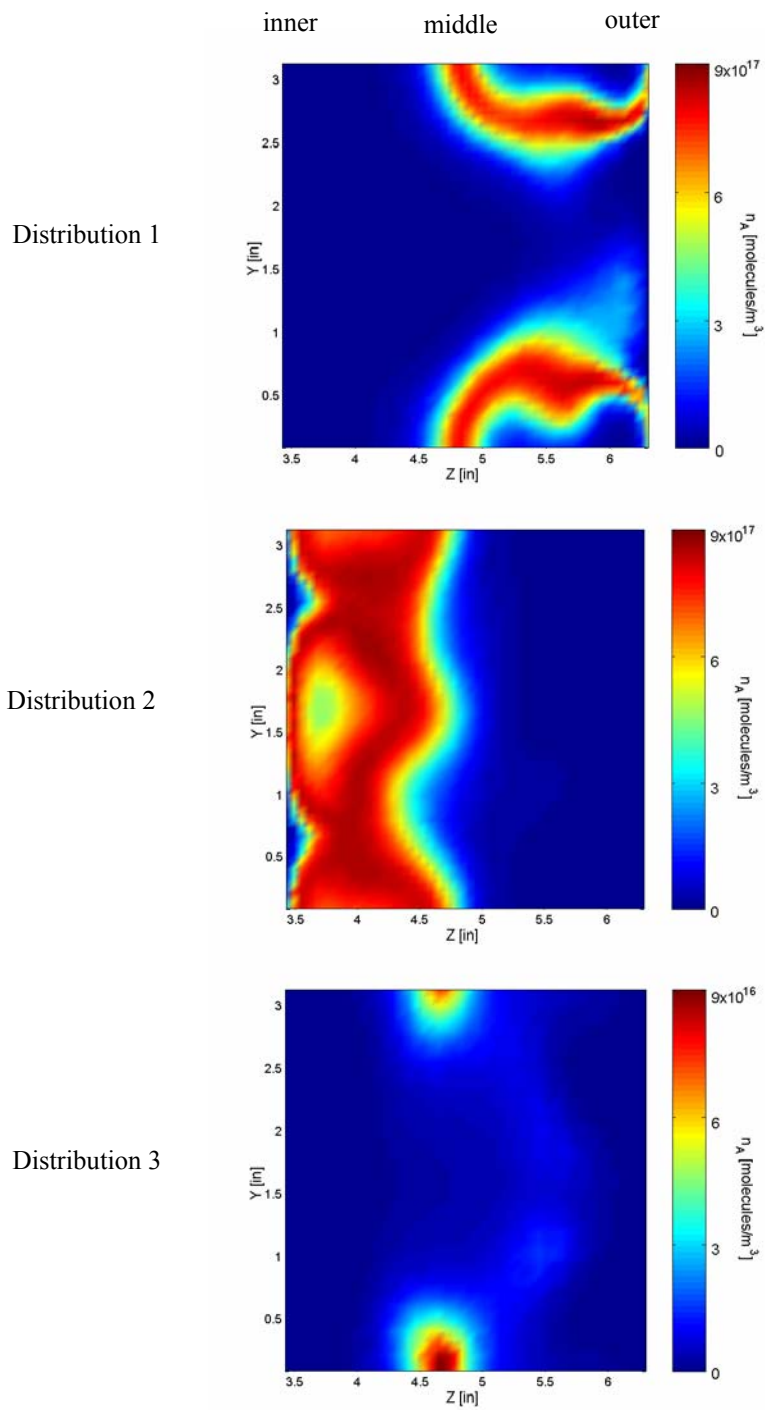


Figure 4.6. Sample n_A excited state population distributions from the ensemble. The outer zone, middle zone, and inner zone, locations are marked at the top of the figure.

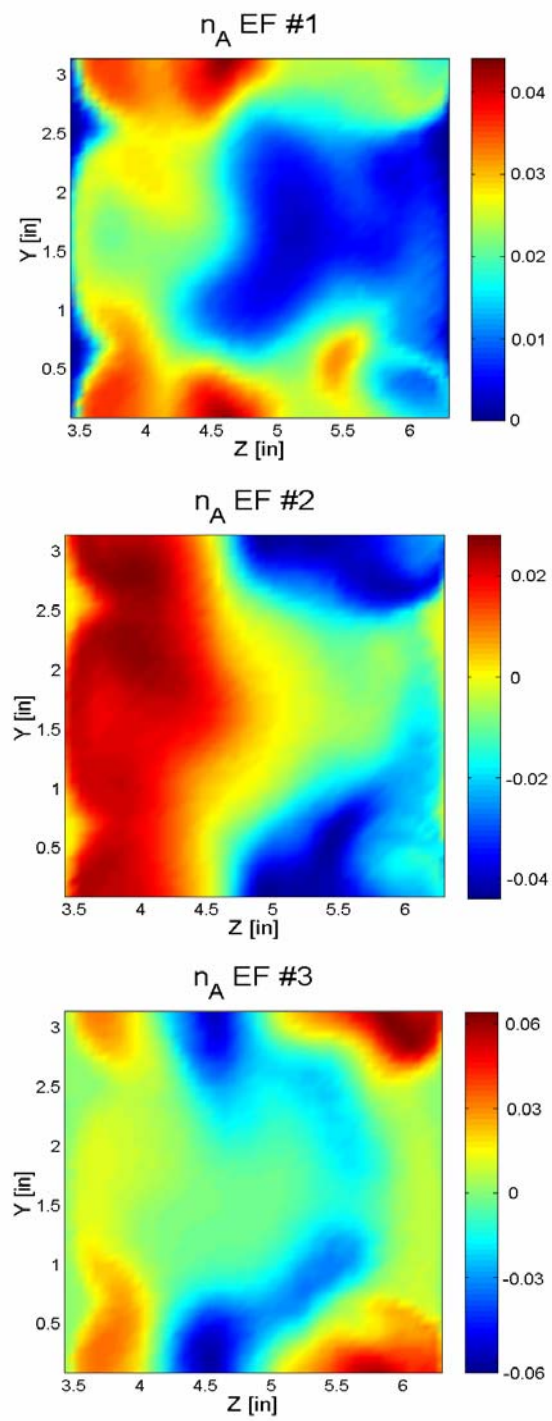


Figure 4.7. First three n_A population eigenfunctions.

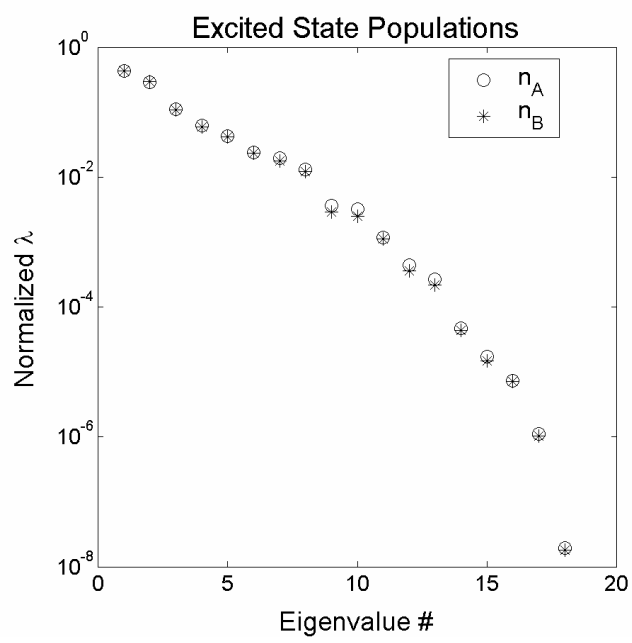


Figure 4.8. Eigenvalue spectra for the n_A and n_B population eigenfunctions.

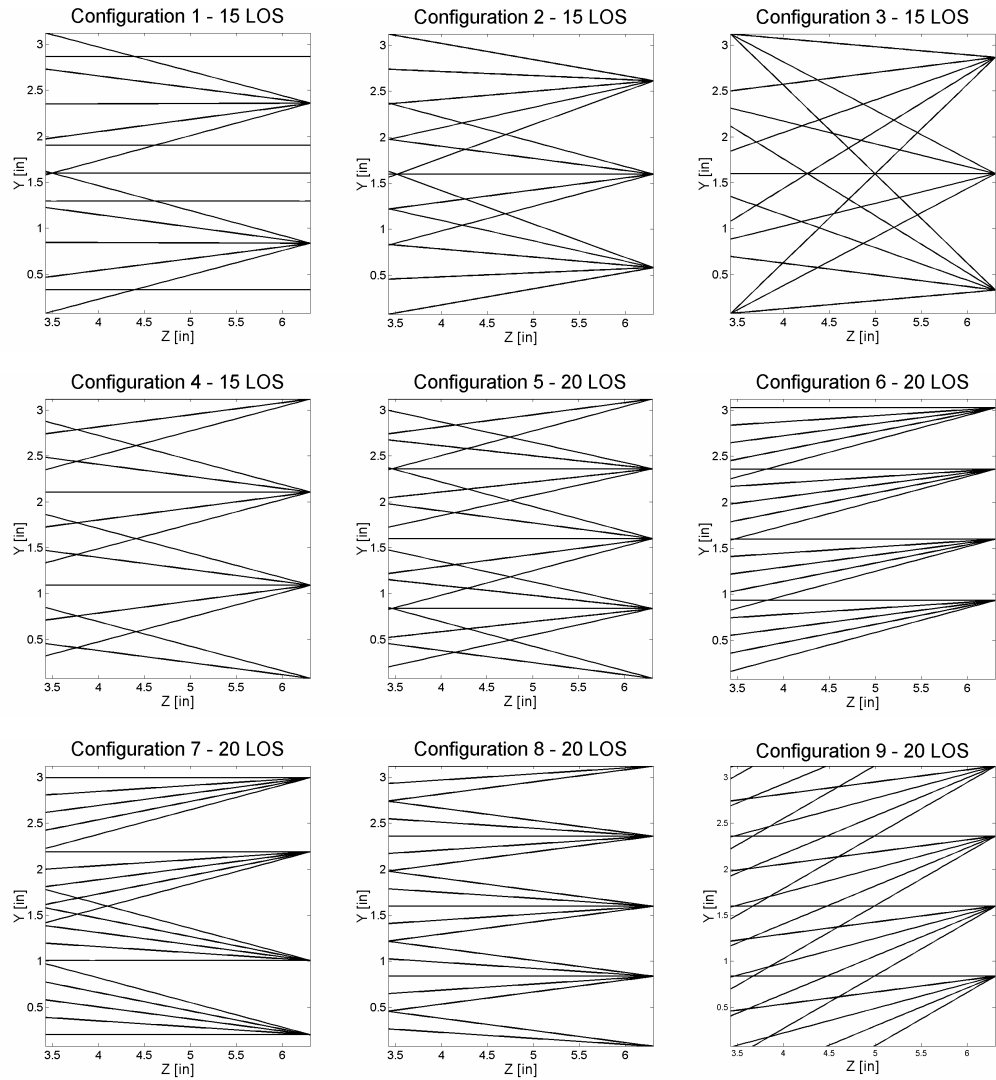


Figure 4.9. LOS measurement configurations considered. Inner, middle, and outer regions correspond to minimum, median, and maximum Z locations as presented in Figure 4.6.

used per combustor nozzle in these measurement configurations. Similar to the four-probe configurations above, configuration 4 consists of three probes only with one probe split across the boundaries. Except for configuration 1, all configurations result in a maximum of four probes installed per combustor nozzle.

4.4.1 Evaluation of Tomographic Measurement Configurations

The efficacies of the nine line-of-sight measurement configurations shown in Figure 4.9 were evaluated using TRKB reconstructions of the n_A and n_B distributions. The number of lines-of-sight employed in a measurement determines the maximum number of basis functions that can be used for reconstruction without making the problem underdetermined. It is beneficial to make the problem overdetermined by increasing the number of lines-of-sight or reducing the number of basis functions used for reconstruction. Solution of an overdetermined problem reduces the effects of random errors or noise in the projection measurements on the weighting factors calculated from TRKB. The number of basis functions used for reconstruction will depend on the accuracy needed for a given application. Sirovich suggests defining the *representational dimension* as the number of eigenfunctions with eigenvalues greater than 1% of the first eigenvalue [29]. For the n_A and n_B eigenvalue spectra shown in Figure 4.8, the representational dimension as defined above is equal to 8, though eigenvalues 9 and 10 have values close to 1% of the first eigenvalue. Preliminary reconstructions indicated that it might be necessary to include up to 12 eigenfunctions to capture some significant features occurring in a few specific distributions. As a result TRKB reconstructions have been evaluated using basis sets consisting of 10 and 12 eigenfunctions. The limited basis sets of 10 and 12 eigenfunctions lead to significant representation errors, with average representation errors for the 18

ensemble distributions being 40-60% of the total reconstruction error for various line-of-sight configurations. The average representation error for a basis set of 12 eigenfunctions is approximately half that of the 10 eigenfunction basis set, showing the ability of the additional basis functions to capture important features in the ensemble distributions. However, increasing the number of eigenfunctions in the basis set results in a less over-determined reconstruction problem, therefore retrieval errors for the 12 eigenfunction basis set compose a larger percentage of the total reconstruction errors than for the 10 eigenfunction basis set.

The previous work of Chojnacki *et. al.* has addressed the problem of line-of-sight configuration selection using TRKB for the case where distributions to be reconstructed were within the span of the basis set [18]. For the practical problem of the engine combustor presented in this work, it is likely that measured distributions will be outside the span of the basis set due to variations in operating state conditions not seen in the numerical simulations and due to the use of a subset of eigenfunctions for reconstruction. For this study, numerical simulations of eighteen fuel-flow configurations have been used to derive the POD eigenfunctions. Even if all available eigenfunctions were used in the basis set, off-design conditions would likely force the empirically measured distributions outside the span of the basis functions. Thus, it is useful to investigate TRKB performance when out-of-span distributions are encountered, such as those that can occur in a practical measurement context. In addition to making the problem overdetermined by reducing the number of basis functions used, evaluating the TRKB reconstructions using a limited basis set is a good indicator of reconstruction behavior when out-of-span distributions are encountered.

TRKB reconstructions are performed for all 18 distributions in each n_A and n_B ensemble, for a total of 36 reconstructions for each measurement configuration.

Average error measures of all 36 reconstructions for each configuration are shown in Figure 4.10. Averages of the three error measures show that errors are reduced when 12 eigenfunctions are used as a basis instead of 10 eigenfunctions, resulting in significant reductions in reconstruction error for all measurement configurations. For a basis set of 12 eigenfunctions, average values of error measures are similar for the nine configurations investigated. Maximum average values of the normalized reconstruction and absolute errors are under 0.24, which is within the normal range of errors for reconstructions utilizing limited data [17,20,26].

Though error measures are similar for the nine configurations, careful selection of a measurement configuration can result in some improvements in reconstruction. In general, average errors are lowest for a 12 eigenfunction basis set using measurement configurations 1, 4, 5, 6, and 9. Configuration 1 would require the use of two 5-view probes and five single-view probes for a total of 7 probes. While reconstruction errors are low, the practical considerations of combustor modification are likely to eliminate configuration 1 as a realistic possibility. The use of configuration 4 is advantageous because only 3 probes are necessary for measurements, reducing the modifications made to the combustor. However, the limitation of configuration 4 is that only 15 LOS are used, making the reconstruction problem less overdetermined than for a configuration with 20 LOS's. Configuration 4 would also make the least-squares problem underdetermined if a full basis set of 18 eigenfunctions was considered.

Reconstructions using measurement configurations 4, 5, 6, and 9 and a basis set of 12 eigenfunctions are evaluated in the presence of random error or noise in the projection measurements. Noise levels of 5% and 10% are added to the projection measurements p given by the line integral in Equation (4.41); see Equation (4.42).

$$p_n = p + \gamma \cdot p \cdot e_{rand} \quad (4.42)$$

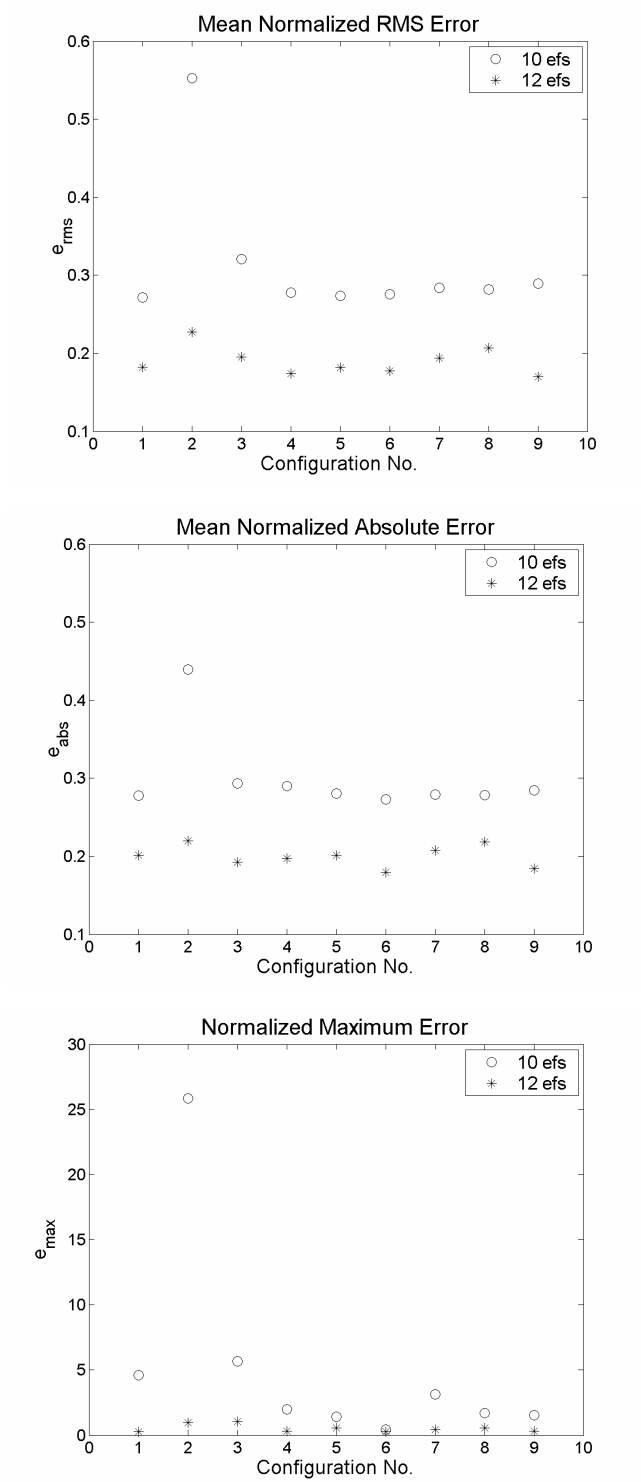


Figure 4.10. Mean error measures presented for the nine measurement configurations.

where p_n is the noisy projection measurement, γ is the noise level maximum (5% or 10%), and e_{rand} is a vector of uniformly generated random numbers from -1 to 1. Twenty sets of noisy projection measurements are calculated according to Equation (4.42) for four sample distributions of the n_A population ensemble that contain features representative of the different combustor operating states. The resulting reconstruction errors averaged over the 20 noisy data sets for each distribution are presented in Figure 4.11. Error measures for the case of 5% noise are within the normal range of error measures for tomographic reconstruction using limited data, but the error measures increase to significantly higher values when noise levels of 10% are considered. It is also noticeable that errors increase significantly when noise is added to distributions that have very low reconstruction errors without noise being present (e.g. sample distributions 1 and 4). In the absence of noise, sample distributions 1 and 4 have both low representation and retrieval errors. Reconstruction errors presented in Figure 4.11 indicate that measurement configuration 9 results in the lowest errors of the four configurations evaluated in the presence of noise.

Another measure of the efficacy of a measurement configuration can be considered. The condition number of the eigenfunction projection matrix D has been shown to be one method of gauging the reconstruction effectiveness of a configuration [16,18,27]. The condition number, $\kappa(D)$, is defined as

$$\kappa(D) = \sigma_1 / \sigma_{N_B} \quad (4.43)$$

where σ_1 is the largest singular value of D and σ_{N_B} is the smallest singular value. Studies have shown that low condition numbers often indicate reconstruction errors will be low [16,26]. The condition number of D is a minimum at 1 when D is orthogonal. Given that the KL eigenfunctions used in the basis set are orthogonal, low

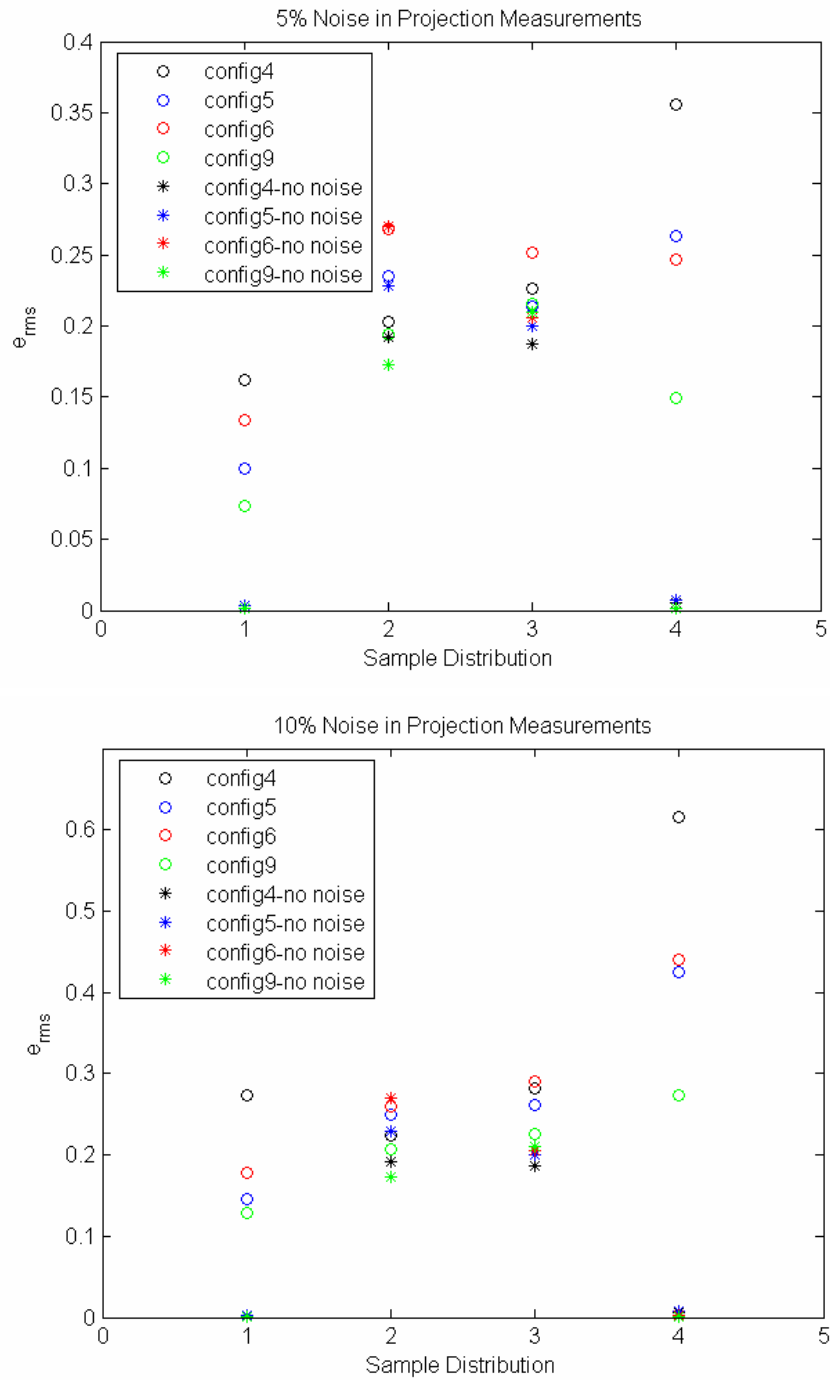


Figure 4.11. Average reconstruction errors for four sample n_A distribution reconstructions in the presence of noise in the projection measurements.

condition numbers indicating a nearly orthogonal projection matrix can be achieved with selection of a proper measurement configuration. Condition numbers for the eigenfunction projection matrices using 12 eigenfunctions are shown in Table 4.1 for the nine configurations. Configuration 9 has a low condition number as well as low errors, even in the presence of noise, and would be a good choice for measurements if the installation of four probes in the combustor sector wall is feasible.

All measurement configurations considered include lines-of-sight distributed over a large area of the combustor sector. This allows for line-of-sight measurement coverage of many important features that occur in the H₂O distributions for the different fuel injector operating states studied (see Figure 4.6 for samples). While coverage of a large area of the sector is important, reconstruction results show that it is necessary to include measurements to capture specific features in the H₂O

Table 4.1. Projection matrix condition numbers for a 12 eigenfunction basis set.

<i>Measurement Configuration</i>	<i>Condition Number</i>	
	<i>n_A projection matrix</i>	<i>n_B projection matrix</i>
1	247.69	403.23
2	660.01	478.20
3	58.62	55.02
4	147.59	132.53
5	92.52	90.09
6	165.15	152.49
7	154.54	154.48
8	319.28	282.58
9	24.44	24.13

distributions near the boundaries of the sector (e.g. features seen in distributions 2 and 3 in Figure 4.6). Practical consideration of combustor modifications was taken into account in all configurations through limitations on the number and spacing of measurement probes and placement of probes along only one side of the combustor. There are some physical similarities amongst the configurations that result in the lowest errors (configurations 1, 4, 5, 6, 9). These configurations include lines-of-sight near or at the minimum and maximum Y locations (the boundaries of each combustor nozzle sector), where adjacent nozzles of the combustor meet, and lines-of-sight through the middle region of the combustor. Lines-of-sight near the minimum and maximum Y boundaries are important for measurements of several distributions, such as distribution 3 presented in Figure 4.6, where small features are concentrated in regions near the edges of the domain. The fan-like LOS arrangement of the 5-view probes makes it difficult to achieve good coverage near the side of the combustor where the probes are located. Lack of projection data in this region is detrimental to the reconstruction of distributions similar to distribution 1 presented in Figure 4.6. Most of the low-error configurations have lines-of-sight distributed over a large area of the domain (configurations 1, 5, and 9) and/or include specific regions where significant features are present in some distributions (configuration 6). Configuration 9 incorporates all of the features above with 20 lines-of-sight, resulting in both low errors and a low condition number. Reconstructions of sample n_A and n_B ensemble distributions using 12 eigenfunctions are presented in Figure 4.12 for configuration 9.

Temperature distributions can be reconstructed according to Equation (4.24) using populations n_A and n_B measured for the same operating state. Due to the exponential dependence of populations on temperature, relatively small errors in population reconstructions are amplified in the temperature reconstructions. Temperature distributions for each fuel-flow operating state obtained from the

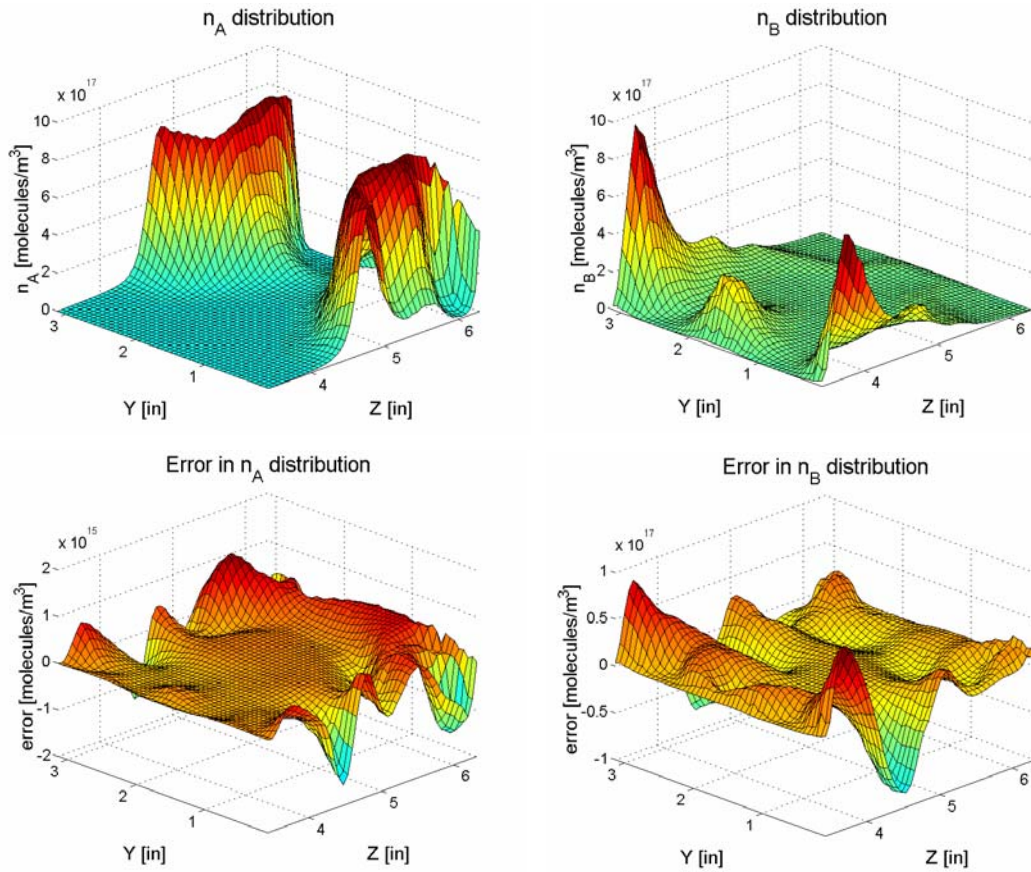


Figure 4.12. Sample population distributions and errors in reconstruction. Note, the distributions for n_A and n_B presented here are for different operating states of the combustor. Error in the distributions presented is calculated as $(f_{recon} - f_{actual})$.

combustion simulations were used to obtain POD temperature eigenfunctions. Once a temperature distribution has been calculated from the population reconstructions according to Equation (4.24), the temperature eigenfunctions can be used to “filter” the calculated distribution. The temperature distribution is filtered by computing the inner products of the temperature eigenfunctions with the calculated distribution, producing a new set of weighting factors. These weighting factors are used in a series expansion to construct the “filtered” temperature distribution using a basis set consisting of the temperature eigenfunctions. Results show that filtering the temperature distributions in this manner significantly reduces the large errors that

result from extracting temperature distributions from reconstructed population distributions. Sample reconstructions of temperature for the two operating states presented in Figure 4.12 are shown in Figure 4.13. Error measures for temperature distributions calculated from the 12-eigenfunction population reconstructions and filtered using 12 temperature eigenfunctions are presented in Figure 4.14. While the error measures have been reduced significantly in many cases using the filtering technique described, *rms* temperature reconstruction errors remain large (greater than 1) compared to the population distribution reconstruction errors.

4.4.2 Control Applications

Although temperature determination using excited state population reconstructions results in large errors, the resulting population and temperature reconstructions can be used for operating state identification in control applications. For the present study, operating states are defined by the percentages of fuel-flow through the injectors. The corresponding excited state population and temperature distributions for each operating state can be used for state identification. For the 18 operating states supplied, identification was attempted using distributions of n_A populations, n_B populations, and filtered temperature.

State identification was accomplished through a least-squares fit of the weighting factors for each reconstructed distribution to the best representation weighting factors, as described in Section 4.2. This procedure was tested using reconstructions from different line-of-sight measurement configurations for the n_A , n_B , and filtered temperature distributions. Results show that this method is significantly more successful at identifying states using n_A or n_B distributions than using the filtered temperature distributions (see Table 4.2). The number of states successfully identified

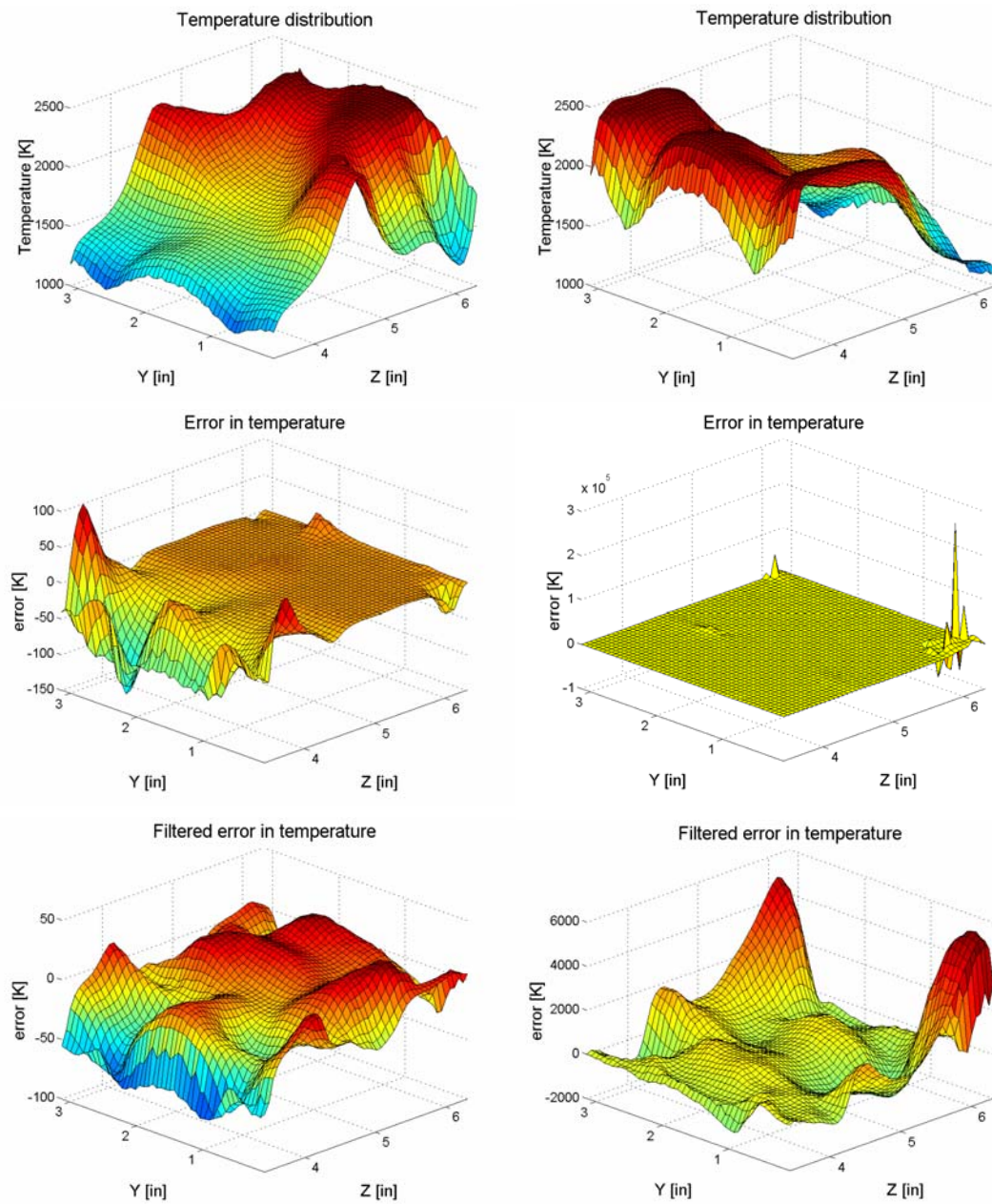


Figure 4.13. Temperature distributions and errors in reconstructions corresponding to the two operating states presented in Figure 4.12. Error in the distributions presented is calculated as $(f_{recon}-f_{actual})$.

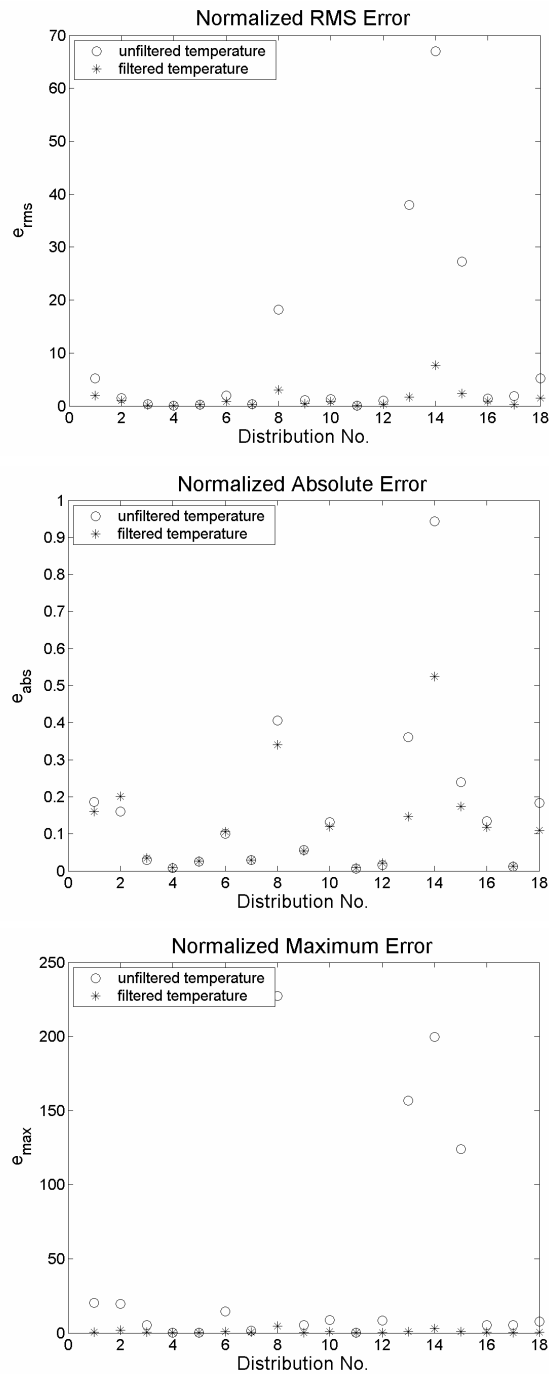


Figure 4.14. Error measures corresponding to temperature distributions calculated from reconstructed populations (○) and filtered using temperature eigenfunctions (*).

using population distributions is also not very dependent on the configuration chosen as at least 17 of the 18 states were identified using all configurations. Preliminary studies have shown that state identification using the filtered temperature distributions is dependent on the number of temperature eigenfunctions used in the filtering process and the least-squares fit described above, allowing for some optimization of the temperature filtering and state identification processes. However, currently there has been no determination of a systematic method for optimizing the number of temperature eigenfunctions used in this process and population distributions remain the best choice for state identification. The number of states identified for each distribution type is presented in Table 4.2 for the nine configurations using a 12 eigenfunction basis set. A sample set of norms $\|\{\alpha\} - \{\beta\}\|$ for state identification of a single sample excited state distribution is presented in Table 4.3 using configuration 9.

Table 4.2. Number of states identified using basis sets consisting of 12 eigenfunctions.

<i>configuration</i>	<i>Number of States Identified</i>		
	<i>n_A population</i>	<i>n_B population</i>	<i>filtered temperature</i>
1	18	17	10
2	17	17	9
3	17	17	11
4	17	17	7
5	17	17	11
6	17	17	12
7	17	17	7
8	17	17	8
9	17	17	10

Table 4.3. Sample State Identification Results

<i>Sample Distribution No. to be Identified $\{\alpha\}$: 5</i>	
<i>Distribution No. to Match $\{\beta\}$</i>	$\ \{\alpha\} - \{\beta\}\ $
1	0.4668×10^{20}
2	0.5596×10^{20}
3	0.5919×10^{20}
4	0.4636×10^{20}
5	0.0041×10^{20}
6	0.4893×10^{20}
7	0.7428×10^{20}
8	0.4650×10^{20}
9	0.2812×10^{20}
10	0.2162×10^{20}
11	0.4909×10^{20}
12	1.0930×10^{20}
13	0.3385×10^{20}
14	0.4681×10^{20}
15	0.4667×10^{20}
16	0.4564×10^{20}
17	0.6264×10^{20}
18	0.4679×10^{20}

Because the TRKB basis functions are normalized, the magnitudes of the resulting TRKB weighting factors are on the order of the population distributions. Note that the large values of the norm results seen in Table 4.3 are comparable to the magnitude of the weighting factors calculated for tomographic reconstruction.

4.5 Summary and Conclusions

Active control of combustion systems for propulsion is important to maintaining the stability and peak performance of a system. Knowledge of the

operating state of a gas turbine combustor allows for feedback control through modulation of fuel injector flow rates, allowing for optimization of efficiency, emission composition, and exit plane temperature distribution. Operating states can be defined by distributions of composition, temperature, pressure, etc. that result from the control of a combustion system through fuel-injection or acoustic modulation of flow through the system. In this study, operating states are defined by the percentages of fuel-flow through the injectors, resulting in excited state population and temperature distributions specific to each state. Minimally invasive measurements of operating conditions are required for monitoring and feedback control of the system.

We have investigated the use of emission tomography for measurements in an engine combustor. Emission measurements were simulated using numerically evaluated line-of-sight integrals of excited state number densities of water for two emission transitions. Number densities were calculated from mean pressure, temperature, and fuel/air ratio distributions generated by CFD simulation. Tomographic reconstruction was performed using Tomographic Reconstruction via a Karhunen-Loeve Basis (TRKB) which utilizes an optimal basis set to reduce the number of basis functions and thereby reduce the number of measurement lines-of-sight required for reconstruction. Using this approach, the number of required line-of-sight measurements has been reduced, minimizing physical modifications necessary to the combustor for emission measurements.

TRKB reconstructions of excited state populations and temperature were used to evaluate nine line-of sight measurement configurations. Use of a 12 eigenfunction basis set improved population reconstructions for all configurations when compared with a basis set of 10 eigenfunctions. Error measures for population reconstructions were within the normal range of tomographic errors but required very few line-of-sight measurements due to the optimality of the basis set. Error measures using a 12-

eigenfunction basis set were comparable for the nine measurement configurations evaluated though some configurations showed slight improvements in error measure and condition number of the eigenfunction projection matrix used in TRKB. Depending on the number of probes desired, configurations 4 (three probes) and 9 (four probes) have been determined to be good choices for a measurement configuration.

Operating state identification for control applications was investigated using the TRKB reconstructions. Use of reconstructed population distributions for state identification was much more accurate than use of the filtered temperature reconstructions. At least 17 of the 18 states were identified using population reconstructions, while at most 12 were identified using temperature reconstructions. Filtered temperature reconstructions were calculated from population distribution reconstructions at two excited states and filtered using temperature eigenfunctions. Errors present in the population reconstructions were amplified in the temperature reconstructions, making state identification difficult. It was determined that the excited state populations were the best choice for state identification.

Advances in measurement technology have made it possible to consider active feedback control of a gas turbine engine combustor. In this investigation, we have evaluated the potential for a control sensor based on multiple line-of-sight emission tomography. Tomographic reconstruction tools developed at Cornell and applied to combustor simulation data from Pratt & Whitney have been used to evaluate and optimize the line-of-sight measurement configuration of an exit plane control sensor. The sensor is based on fiber-optic water emission measurements in the near infrared along a limited number of lines-of-sight. Errors in reconstructed population and temperature distributions from phantom data were evaluated and it is shown that the combustor operating state can be identified from the reconstructed population

distribution. Exit plane temperature distributions, emissions, and efficiency can be controlled through the use of operating state information supplied by the measurements, thereby improving the performance of the combustor.

Appendix

POD Analysis and Results

An ensemble of N_M distributions $\{f_j\}$, such as H₂O excited state populations for the various fuel-flow conditions, can be expanded as a superposition of KL eigenfunctions, $\{\phi_l\}$, each with a set of associated distribution coefficients $\{a_l\}$ that correspond to all of the distributions in the ensemble.

$$f(y_i, z_j, k) = \sum_{l=1}^{N_M} a_l(k) \phi_l(y_i, z_j) \quad (4.43)$$

$$i=1, \dots, N_y, \quad j=1, \dots, N_z, \quad k=1, \dots, N_M$$

N_M is the total number of eigenfunctions provided by POD analysis, and is equal to the number of distributions available in the ensemble. Distributions of excited state populations for 18 fuel-flow configurations were used for analysis. Each eigenfunction also has an associated eigenvalue, which classifies the importance of the eigenfunction to the representation of the ensemble of distributions. The eigenvalues, $\{\lambda_l\}$, are the mean square of the associated distribution coefficients, $\{a_l(k)\}$.

The KL eigenfunctions and distribution coefficients are determined from a matrix eigenvalue problem via the method of snapshots [29]

$$CA = \Lambda A \quad (4.44)$$

where C is a $N_M \times N_M$ correlation matrix, A is a $N_M \times N_B$ matrix of distribution coefficients, and Λ is a diagonal $N_B \times N_B$ matrix of eigenvalues. The correlation matrix is defined as

$$C = (1/N_M)\Psi G\Psi^T \quad (4.45)$$

where Ψ is a $N_M \times N_p$ matrix containing the distributions in the ensemble, N_p is the number of spatial points in each distribution (equal to $N_y \times N_z$), and G is a $N_p \times N_p$ matrix used to numerically integrate each ensemble distribution with another ensemble distribution. Using this method, eigenfunctions are given by a superposition of instantaneous distributions from the ensemble, producing an intrinsically defined basis set,

$$\Phi = (1/N_M)\Lambda^{-1}A^T\Psi \quad (4.46)$$

where the $N_M \times N_p$ matrix Φ contains N_M eigenfunctions that are normalized according to

$$\Phi G \Phi^T = I \quad (4.47)$$

For the present study, combustor simulations provide distributions of pressure, temperature, and molar fuel/air ratios for 18 combustor operating states defined by the fuel-injector flow configurations. Mole fractions of H₂O are computed from these distributions using Cantera and distributions of H₂O total number density are calculated according to Equation (4.23). Excited state number densities n_A and n_B are calculated for two specific ro-vibrational transitions according to Equation (4.22) where the excited state 2 in Equation (4.22) corresponds to each of the measured excited states A and B . The sets of distributions of n_A and n_B for all combustor operating states form two ensembles, Ψ_A and Ψ_B , used to calculate two sets of eigenfunctions, Φ_A and Φ_B according to Equation (4.47).

The eigenvalue, λ_i , associated with each eigenfunction, ϕ_i , classifies the importance of that eigenfunction in the representation of the ensemble of distributions investigated. The eigenfunctions are arranged in order of importance, the first eigenfunction having the largest eigenvalue and the last eigenfunction having the smallest eigenvalue. The total amount of information present in a subset of eigenfunctions, termed the *information content*, can be evaluated as the sum of the subset of normalized eigenvalues. Eigenvalues are normalized as

$$\bar{\lambda}_i = \frac{\lambda_i}{\sum_{j=1}^{N_M} \lambda_j} \quad (4.48)$$

and are used to classify the information content of a subset of the first M eigenfunctions, E_M (sometimes referred to as the “energy” of a subset of eigenfunctions) [16,29,43]

$$E_M = \sum_{i=1}^M \bar{\lambda}_i . \quad (4.49)$$

Acknowledgements

The work reported here was supported by Pratt and Whitney. The authors would like to thank Dr. Jeffrey Cohen and Dr. Arash Ateshkadi for their valuable input and feedback.

References

- [1] Docquier, N., and Candel, S., "Combustion Control and Sensors: A Review," *Progress in Energy and Combustion Science*, Vol. 28, 2002, pp. 107-150.
- [2] Candel, S., "Combustion Dynamics and Control: Progress and Challenges," *Proceedings of the Combustion Institute*, Vol. 29, The Combustion Institute, Pittsburgh, 2002, pp. 1-28.
- [3] Annaswamy, A.M. and Ghoniem, A.F., "Active Control in Combustion Systems," *IEEE Control Systems Magazine*, Vol. 15, Issue 6, 1995, pp. 49-63.
- [4] Riley, A.J., Park, S., Dowling, A.P., Evesque, S., and Annaswamy, A.M., "Advanced Closed-Loop Control on an Atmospheric Gaseous Lean-Premixed Combustor," *Journal of Engineering for Gas Turbines and Power, Transactions of the ASME*, Vol. 126, No. 4, 2004, pp. 708-716.
- [5] Hathout, J.P., Fleifil, M., Annaswamy, A.M., and Ghoniem, A.F., "Heat Release Actuation for Control of Mixture-Inhomogeneity-Driven Combustion Instability," *Proceedings of the Combustion Institute*, Vol. 28, The Combustion Institute, Pittsburgh, 2000, pp. 721-730.
- [6] Johnson, C., Neumeier, Y., Lieuwen, T., and Zinn, B., "Experimental Determination of the Stability Margin of a Combustor Using Exhaust Flow and Fuel Injection Rate Modulations," *Proceedings of the Combustion Institute*, Vol. 28, The Combustion Institute, Pittsburgh, 2000, pp. 757-763.
- [7] Ghoniem, A.F., Annaswamy, A., Wee, D., Yi, T., and Park, S., "Shear Flow-Driven Combustion Instability: Evidence, Simulation, and Modeling," *Proceedings of the Combustion Institute*, Vol. 29, The Combustion Institute, Pittsburgh, 2002, pp. 53-60.
- [8] Park, S., Wachsman, A., Annaswamy, A., Ghoniem, A.F., Pang, B., and Yu, K.H., "Experimental Study of POD-based Control for Combustion Instability Using a Linear Photodiode Array," *AIAA Paper 2004-0639*, January 2004.
- [9] Hathout, J.P., Annaswamy, A., Fleifil, M., and Ghoniem, A.F., "A Model-Based Active Control Design for Thermoacoustic Instability," *Combustion Science and Technology*, Vol. 132, 1998, pp.99-138.
- [10] Billoud, G., Galland, M.A., Huu, C.H., and Candel, C., "Adaptive Active Control of Combustion Instabilities," *Combustion Science and Technology*, Vol. 81, 1992, pp.257-283.
- [11] Gutmark, E, Parr, T.P., Hanson-Parr, D.M., and Schadow, K.C., "Closed-loop Amplitude Modulation Control of Reacting Premixed Turbulent Jet," *AIAA Journal*, Vol. 29, No. 12, 1991, pp. 2155-2162.

- [12] Furlong, E.R., Baer, D.S., and Hanson, R.K., "Combustion Control Using Multiplexed Diode-Laser Sensor System," *Proceedings of the Combustion Institute*, Vol. 26, 1996, pp. 2851-2858.
- [13] Palaghita, T., and Seitzman, J., "Pattern Factor Sensing and Control Based on Diode Laser Absorption," *AIAA-2005-3578*, 41st AIAA/ASME/SAE/ASEE Joint Propulsion Conference and Exhibit, Tucson, AZ, 10-13 Jul 2005.
- [14] Lord, W.K., MacMartin, D.G., and Tillman, T.G., "Flow Control Opportunities in Gas Turbine Engines," *AIAA 2000-2234*, Fluids 2000, Denver, CO, 19-22 June 2000.
- [15] Chen, Y., Scarborough, D., Liang, S., Aung, K., and Jagoda, J., "Manipulating Pattern Factor Using Synthetic Jet Actuators," *AIAA 2000-1023*, 38th Aerospace Sciences Meeting and Exhibit, Reno, NV, 10-13 January 2000.
- [16] Torniainen, E.D., *Tomographic Reconstruction Using a Karhunen-Loeve Basis*, Ph.D. Dissertation, Cornell University, Ithaca, NY, 2000.
- [17] Feng, M.Y., *Development of a Real-Time Tomography System for Combustion*, Ph.D. Thesis, Cornell University, Ithaca, NY, 2000.
- [18] Chojnacki, A.M., Sarma, A., Wolga, G.J., and Torniainen, E.D., and Gouldin, F.C., "Infrared Tomographic Inversion for Combustion and Incineration," *Combustion Science and Technology*, Vol. 116-117, 1996, pp. 583-606.
- [19] Kak, A.C., and Slaney, M. *Principles of Computerized Tomographic Imaging*, IEEE Press, New York, 1988.
- [20] Verhoeven, D., "Limited-data Computed Tomography Algorithms for the Physical Sciences," *Applied Optics*, Vol. 32, 1993, pp. 3736-3754.
- [21] Winklhofer, E. , "Optical Access and Diagnostic Techniques for Internal Combustion Engine Development," *Process Imaging for Automatic Control, Proceedings of SPIE*, Vol. 4188, 2001, pp. 134-140.
- [22] McCann, H., Carey, S.J., Hindle, F.P., Ozanyan, K.B., Winterbone, D.E., and Clough, E., "Near Infra-Red Absorption Tomography System for Measurement of Gaseous Hydrocarbon Distribution," *Process Imaging for Automatic Control, Proceedings of SPIE*, Vol. 4188, 2001, pp. 140-141-150.
- [23] Beiting, E.J., "Fiber-Optic Fan Beam Absorption Tomography", *Applied Optics*, Vol. 31, Issue 9, 1992, pp. 1328-1343.
- [24] Correia, D.P., Ferrao, P., and Caldeira-Pires, A., "Advanced 3D Emission Tomography Flame Temperature Sensor," *Combustion Science and Technology*, Vol. 163, 2001, pp. 1-24.
- [25] Snelling, D.R., Thomson, K.A., Smallwood, G.J., Gulder, O.L., Weckman, E.J., and Fraser, R.A., "Spectrally Resolved Measurement of Flame Radiation to Determine Soot Temperature and Concentration," *AIAA Journal*, Vol. 40, No. 9, 2002, pp. 1789-1795.

- [26] Ravichandran, M., and Gouldin, F.C., "Reconstruction of Smooth Distributions from a Limited Number of Projections," *Applied Optics*, Vol. 27, 1988.
- [27] Torniainen, E.D., Hinz, A., and Gouldin, F.C. "Tomographic Analysis of Unsteady Reacting Flows: Numerical Investigation," *AIAA Journal*, Vol. 36, No. 7, 1998, pp. 1270-1278.
- [28] Torniainen, E.D. and Gouldin, F.C., "Tomographic Reconstruction of 2-D Absorption Coefficient Distributions from a Limited Set of Infrared Absorption Data," *Combustion Science and Technology*, Vol. 131, 1998, pp. 85-105.
- [29] Sirovich, L., and Emerson, R., "Management and Analysis of Large Scientific Datasets," *International Journal of Supercomputer Applications*, Vol. 6, 1992, pp. 50-68.
- [30] Holmes, P., Lumley, J., and Berkooz, G., *Turbulence, Coherent Structures, Dynamical Systems and Symmetry*, Cambridge University Press, New York, 1996.
- [31] Goldstein, N., Arana, C.A., Bien, F., Lee, J., Gruninger, J., Anderson, T., and Glasheen, W.M., "Innovative Minimally Intrusive Sensor Technology Development for Versatile Affordable Advanced Turbine Engine Combustors," *Proceedings of the ASME Turbo Expo 2002, Paper number GT-2002-30051*, June 2002.
- [32] Goldstein, N., Adler-Golden, S., Jin, X., Lee, J., Richtsmeier, S., and Arana, C.A., "Temperature and Temperature Profile Measurements in the Combustor Flowpath Using Structured Emission Thermography," *Proceedings of the ASME Turbo Expo 2003, Paper number GT-2003-38695*, June 2003.
- [33] Malecki, R.E., Rhie, C.M., McKinney, R.G., Ouyang, H., Syed, S.A., Colket, M.B., and Madabhushi, R.K., "Application of a CFD-Based Analysis System to the PW6000 Combustor to Optimize Exit Temperature Distribution – Part I: Description and Validation of the Analysis Tool," *Proceedings of the ASME Turbo Expo 2001, Paper number 2001-GT-0062*, June 2001.
- [34] Snyder, T.S., Stewart, J.F., Stoner, M.D., and McKinney, R.G., "Application of a CFD-Based Analysis System to the PW6000 Combustor to Optimize Exit Temperature Distribution – Part II: Comparison of Predictions to Full Annular Rig Test Data," *Proceedings of the ASME Turbo Expo 2001, Paper number 2001-GT-0064*, June 2001.
- [35] Vincenti, W.G. and Kruger, C.H., *Introduction to Physical Gas Dynamics*, Krieger Publishing Co., Malabar, FL, 1986.
- [36] Penner, S.S., *Quantitative Molecular Spectroscopy and Gas Emissivities*, Addison-Wesley Publishing Co, Inc., Reading, MA, 1959.
- [37] Herzberg, G., *The Spectra and Structures of Simple Free Radicals: An Introduction to Molecular Spectroscopy*, Cornell University Press, Ithaca, NY, 1971.

- [38] Dole, M., *Introduction to Statistical Thermodynamics*, Prentice-Hall, Inc., New York, 1954.
- [39] Harris, G.J., Viti, S., Mussa, H.Y., and Tennyson, J., "Calculated High Temperature Partition Function and Related Thermodynamic Data for H₂¹⁶O," *Journal of Chemical Physics*, Vol. 109, No. 17, 1998, pp. 7197-7204.
- [40] Tennyson, J., Zobov, N.F., Williamson, R., Polyansky, O.L., and Bernath, P.F., "Experimental Energy Levels of the Water Molecule," *Journal of Physical and Chemical Reference Data*, Vol. 30, No. 3, 2001, pp. 735-831.
- [41] Gamache, R.R., and Rothman, L.S., "Extension of the HITRAN Database to Non-LTE Applications," *Journal of Quantitative Spectroscopy and Radiative Transfer*, Vol. 48, 1992, pp. 519-525.
- [42] Rothman, L.S., Rinsland, C.P., Goldman, A., Massie, S.T., Edwards, D.P., Flaud, J.M., Perrin, A., Camy-Peyret, C., Dana, V., Mandin, J.Y., Schroeder, J., McCann, A., Gamache, R.R., Wattson, R.B., Yoshino, K., Chance, K.V., Jucks, K.W., Brown, L.R., Nemtchinov, V., and Varanasi, P., "The HITRAN Molecular Spectroscopic Database and HAWKS (HITRAN Atmospheric Workstation): 1996 Edition," *Journal of Quantitative Spectroscopy and Radiative Transfer*, Vol. 60, 1998, pp. 665-710.
- [43] Rothman, L.S., Barbe, A., Benner, D.C., Brown, L.R., Camy-Peyret, C., Carleer, M.R., Chance, K., Clerbaux, C., Dana, V., Devi, V.M., Fayt, A., Flaud, J.M., Gamache, R.R., Goldman, A., Jacquemart, D., Jucks, K.W., Lafferty, W.J., Mandin, J.Y., Massie, S.T., Nemtchinov, V., Newnham, D.A., Perrin, A., Rinsland, C.P., Schroeder, J., Smith, K.M., Smith, M.A.H., Tang, K., Toth, R.A., Vander Auwera, J., Varanasi, P., and Yoshino, K., "The HITRAN Molecular Spectroscopic Database: Edition of 2000 Including Updates through 2001," *Journal of Quantitative Spectroscopy and Radiative Transfer*, 2003.

Chapter 5

Summary

Active control of combustion systems is important to maintaining the stability and peak performance of a system. Combustor efficiency, temperature distribution (pattern factor), radiant signature, exhaust gas composition, and pollutants can be optimized through control of the operating state of a combustion system, which is defined by the composition, temperature, and pressure distributions within the combustor or at the combustor exit. Knowledge of the operating state of a combustor is necessary to enable feedback control of the combustor. Two methods of combustor control that affect the operating state of the combustor are modulation of fuel injector flow rates and acoustic modulation within the combustor. The work presented in this dissertation addressed both combustor control using acoustic modulation of jets (e.g. fuel injectors) as well the sensing technology needed to measure the operating state of the combustor for feedback control purposes.

In Chapter 2, proper orthogonal decomposition was used to analyze ensembles of two-dimensional distributions of concentration and vorticity magnitude in forced reacting rectangular jets. These forced jets are of interest as flow actuators for control. The jet distributions of CO₂ concentration and vorticity magnitude data were obtained by CFD. Proper orthogonal decomposition was used to investigate the large-scale features of the flow through analysis of the POD eigenfunctions. Eigenvalues were used to evaluate the information content of the eigenfunctions and the potential for reduced-order modeling of the CO₂ and vorticity fields using a limited number of basis functions. CO₂ eigenfunctions and vorticity eigenfunctions were similar in shape and

nonzero spatial extent, consistent with the understanding that vortex driven mixing dominates in forced rectangular jets. Vorticity eigenfunctions could be associated to some extent with different vortex orientations, e.g. streamwise vorticity or azimuthal vortex rings. Large-scale structures were easily identified in the POD results and phenomena such as axis-switching were readily apparent. Through evaluation of the eigenvalue spectra and eigenfunction information content, it was determined that there is a greater potential for reduced-order modeling of the CO₂ field than for the vorticity field.

The Cornell IR absorption facility for making LOS measurements on confined and unconfined, reacting and nonreacting flows was presented in Chapter 3. The facility is capable of making simultaneous measurements of LOS absorption over six viewing angles, collecting 1050 LOS measurements in approximately 1.5 ms for high temporal resolution. The measurements were made on an 8 mm x 8 mm forced square jet composed of a mixture of CO₂ and air using a KCl:Li color center laser capable of measurements at wavelengths of 2.45-2.82 μm . Additional absorption measurements of various combustion products (CO₂, H₂O, NO, and NO₂) can be collected using the KCl:Li color center laser with the IR absorption facility. The measurements presented in Chapter 3 were for CO₂ levels of 25% and greater by volume. For practical combustor applications, CO₂ levels below 10% are possible, in such cases absorption measurement uncertainty is a significant concern. Increasing the laser intensity and selecting an appropriate detector with low noise levels and high sensitivity would be primary considerations for measurements of low signal levels. Tomographic reconstructions from projection data collected by the 6-module IR absorption facility were performed using Adaptive Finite Domain Direct Inversion. Reconstructions of multiple jets showed less effects of forcing on the CO₂ field in a 6 m/s jet than in a 3 m/s jet. Additional flow rates and forcing parameters (frequency, forcing signal

power) can be investigated using the IR absorption facility. These data could then be used to study the dominant gradients and spreading in the jet as well as mixing, to provide more insight into the structures and dynamics of these jets.

Performance of Adaptive FDDI was evaluated in Chapter 3 using various phantom distributions of jet/peak configurations as well as high gradient top hat distributions. Results showed that, relative to the original FDDI method, AFDDI performs better for distributions that contain high gradient regions, such as top hat distributions, and produces reconstruction errors lower than those of FDDI in many of these high gradient cases. AFDDI does not always produce lower reconstruction errors than FDDI and may fail to reduce errors in cases where the distribution contains a wide range of spatial gradients. Results showed that for accurate reconstructions, the number of additional basis functions used in AFDDI must be sufficient to thoroughly cover the high gradient regions of a distribution. While noise in the projection measurements generally increased reconstruction errors, both FDDI and AFDDI performed well with reconstruction errors remaining comparable to measurements with no noise added. Overall, AFDDI performed well with error measures comparable to or lower than FDDI error measures for all reconstructions performed in this study.

In Chapter 4, the practical implementation of a tomographic sensor for combustion control was considered using phantom data for application to a gas turbine combustor. Exit plane temperature distributions, pollutant emissions, and efficiency can be controlled through the use of operating state information supplied by the measurements, thereby improving the performance of the combustor. Minimally invasive measurements of operating conditions are required in a practical system. In this work, combustor operating states were defined by the percentages of fuel-flows through multiple fuel injectors and related to the resulting excited state H_2O

population and temperature distributions specific to each operating state. The tomographic sensor investigated in Chapter 4 is based on fiber-optic water emission measurements in the near infrared along a limited number of lines-of-sight. Emission measurements were simulated using numerically evaluated line-of-sight integrals of excited state number densities of water for two emission transitions. Number densities were calculated from mean pressure, temperature, and fuel/air ratio distributions generated by CFD simulations. Tomographic reconstruction was performed using Tomographic Reconstruction via a Karhunen-Loeve Basis (TRKB) which utilizes an optimal basis set to reduce the number of basis functions and thereby reduce the number of measurement lines-of-sight required for reconstruction. Through this approach, the number of required line-of-sight measurements has been minimized, reducing physical modifications necessary to the combustor for emission measurements. Error measures for population reconstructions were within the normal range of tomographic errors but required very few line-of-sight measurements due to the optimality of the basis function set. Operating state identification for control applications was investigated using the TRKB reconstructions. Use of reconstructed population distributions for state identification was much more accurate than use of the temperature reconstructions calculated from the population distributions.

While the studies presented in this paper were performed as separate investigations, it is possible to apply the results from each to the problem of measurement diagnostics for combustion control. Further work on these projects could bring aspects of all three studies together. For example, the IR absorption tomography facility presented in Chapter 3 can be modified to investigate forced rectangular jets such as those presented in the proper orthogonal decomposition analysis presented in Chapter 2. The results from the POD analysis of numerically simulated forced jets could be compared to experimental data collected with the IR

absorption facility. Such a comparison would help further the understanding of how the vortex formations in these jets affect the combustion product distributions, including CO₂ and other product species. Both AFDDI and TRKB reconstruction methods could be applied to the experimentally measured projection data.

Measurements made using the IR absorption facility have been of nonreacting CO₂/air mixtures thus far. A possible next step would be to modify the flow facility to measure CO₂ and H₂O concentrations in combusting flows. An emission tomography sensor similar to the one outlined in Chapter 4 could be constructed for measurements of H₂O in the reacting jets in the flow facility. Line-of-sight configurations would be selected through POD analysis of the forced rectangular jets for implementation with the TRKB method. The reconstructed H₂O and CO₂ distributions obtained from the IR absorption facility could be used to monitor combustion products.

The ideas outlined above are simply a few ways in which the various aspects of the research in this dissertation can be applied for combustion control. Each of the studies in this dissertation addresses important aspects of the development of diagnostics for combustion system control applications. The proper orthogonal decomposition method discussed in Chapter 2 is useful in the analysis of flow structures and dynamics. The tomographic IR absorption facility and emission sensors presented in Chapters 3 and 4 are highly effective sensors for measurements of combustion systems. AFDDI and TRKB are powerful techniques for the reconstruction of temperature and species concentration distributions. Coupled with the measurements systems, they are extremely valuable in the analysis of combustion systems. Further investigations can be done to improve the reconstruction methods and sensor performance, and bring the tools described above together for the purpose of combustion control.